POLITECNICO DI MILANO

CFD Assessment of a Flame Area Combustion Model on the Darmstadt TSF Burner

by

Suliman Abdelwahid

Student ID: 904736

Supervisor: Prof. Tommaso Lucchini

Co-Supervisor: Prof. Gianluca D'Errico & Ph.D. Lorenzo Sforza

Master's Thesis submitted in partial fulfillment for the degree of

Master of Science in Mechanical Engineering

in the

School of Industrial and Information Engineering

Department of Mechanical Engineering

June 2020

"In the name of God, the Most Gracious, the Most Merciful"

Suliman Abdelwahid: suliman.abdelwahid@mail.polimi.it
Politecnico di Milano.
June 2020.

Politecnico di Milano:
www.polimi.it
School of Industrial and Information Engineering:
www.ingindinf.polimi.it
Internal Combustion Engine Group:
www.engines.polimi.it

Dedicated to my lovely family

"Turbulence is the most important unsolved problem of classical physics."

- Richard Feynman

Abstract

Despite the push for renewable energy and the more stringent regulations to control pollutants and emissions, the combustion of fossil fuels will continue in order to meet the rapid growth of the world's energy demand. Fuels are a powerful and reliable source of energy, but today they must also be sustainable and clean. Hence, novel combustion techniques are required for the mitigation and control of NO_x and CO_2 emissions. One way to achieve this is through the use of stratified combustion. This combustion mode has shown promising results in mitigating emissions, decreasing throttling losses, and extending the operational range as is the case in direct-injection engines; thus, more understanding is required. Simulations using CFD analysis are powerful tools that allow combustion systems optimization with rather low costs. The target of this thesis work is to assess the Flame Area model proposed by Weller on controlled combustion conditions, with both stratified and homogeneous premixed fuel-air mixtures. In the context of the one-equation Weller model, several algebraic closure correlations were tested for the flame wrinkling factor, such as Gulder, Peters and Muppala ones, and then compared to the two-equations model version, where a transport equation is instead solved for the flame wrinkling factor. A preliminary assessment of the Coherent Flamelet Model (CFM) was also conducted. The TU-Darmstadt turbulent stratified flame (TSF) burner was selected for these assessments, with the steady-state methane-air flames A-r (premixed stratified) and G-r (premixed homogeneous) as chosen configurations. The intention of this basic analysis is to support turbulent engine combustion simulations, where it is more difficult to clarify the differences between the aforementioned modelling strategies. A general agreement is found between the achieved numerical results with both Weller model versions and the TSF burner experimental measurements, with only a partial agreement when using Muppala correlation. However, concerning this last point, fine-tuning of the main calibration coefficient shows rather promising results and improvements. Moreover, a first attempt to model NO_x of the TSF burner was performed under the adiabatic assumption. Finally, a preliminary assessment of the CFM (Choi-Huh version) was performed; nevertheless, more understanding of this model version is needed in the future.

Keywords: CFD; OpenFOAM; LibICE; Weller model; CFM; RANS; Stratified combustion.

Sommario

Nonostante lo slancio verso le energie rinnovabili e le normative sempre più stringenti per controllare l'emissione di inquinanti, i combustibili fossili continueranno ad essere utilizzati per soddisfare la rapida crescita della domanda energetica globale. I combustibili sono una fonte di energia potente e affidabile, ma al giorno d'oggi devono essere soprattutto puliti ed ecosostenibili. Di conseguenza, tecniche di combustione innovative sono necessarie per mitigare e controllare le emissioni di NOx e CO2. Un modo per raggiungere tale obiettivo è attraverso l'uso della combustione stratificata. Questa modalità di combustione ha mostrato risultati promettenti nel'abbattimento delle le emissioni, nella riduzione delle perdite a carico parziale e nell'estensione del campo di utilizzo, come nel caso di motori a iniezione diretta. Una più chiara comprensione di questa modalità di combustione è dunque necessaria. Le simulazioni numeriche condotte per mezzo dell'analisi CFD sono strumenti potenti e relativamente economici per ottimizzare questi sistemi di combustione. L'obiettivo di questo lavoro di tesi è valutare il modello Flame Area proposto da Weller in condizioni di combustione controllata, con miscela sia stratificata che omogenea. Nel contesto del modello Weller a una equazione, sono state testate diverse correlazioni algebriche di chiusura per il fattore di increspamento della fiamma, come quelle di Gulder, Peters e Muppala, e quindi confrontate con la versione del modello a due equazioni, dove invece viene risolta un'equazione di trasporto per il fattore di increspamento della fiamma. E' stata condotta anche una valutazione preliminare sul Coherent Flamelet Model (CFM). Per queste valutazioni è stato selezionato il bruciatore a fiamma stratificata turbolenta (TSF) TU-Darmstadt, adottando come configurazioni fiamme metano-aria stazionarie A-r (premiscelate stratificate) e G-r (premiscelate omogenee). Lo scopo di queste analisi di base su fiamma stazionaria è quello di supportare le simulazioni turbolente in camera di combustione, dove risulta difficile distinguere le differenze tra le strategie di modellazione presentate. Si trova una corrispondenza generale tra i risultati numerici raggiunti sia con le versioni del modello Weller che con le misure sperimentali del bruciatore TSF, con una corrispondenza solo parziale quando si utilizza la correlazione Muppala. Tuttavia, riguardo a quest'ultimo punto, un'accurata messa a punto del coefficiente di calibrazione principale mostra risultati e miglioramenti piuttosto promettenti. Inoltre, un primo tentativo per modellare gli NOx del combustore TSF è stato condotto con l'ipotesi di adiabaticità. Infine, è stata eseguita una valutazione preliminare del CFM (versione Choi-Huh); tuttavia, in futuro sarà necessaria una maggiore comprensione di questa versione del modello.

Keywords: CFD; OpenFOAM; LibICE; Modello Weller; CFM; RANS; Combustione stratificata.

Contents

List of Figures

List of Tables

Chapter 1

Introduction

1.1 Background

Global warming is one of the major concerns for today's world and has driven stricter emission regulations. Such environmental restrictions have caused a push for renewable energy. Despite this, the use of fossil fuels is expected to increase by mid-century to meet the rapid growth of the world's energy demand coming mainly from developing economies. Hence, novel combustion techniques are required for the mitigation and control of NO_x and CO_2, the latter has been identified as the dominant contributor in the greenhouse gases and is responsible for more than 60% of the global warming effect. Figure 1.1 depicts the trend of the world energy supply mix to meet the growing energy demand in the foreseeable future [1]. Natural gas demand increases the most, to help meet the evolving needs for electricity and power generation. Oil and natural gas will continue to supply about 55% of the world's energy demand by mid-century. Therefore, combustion remains a quintessential energy technology for power generation in the future.

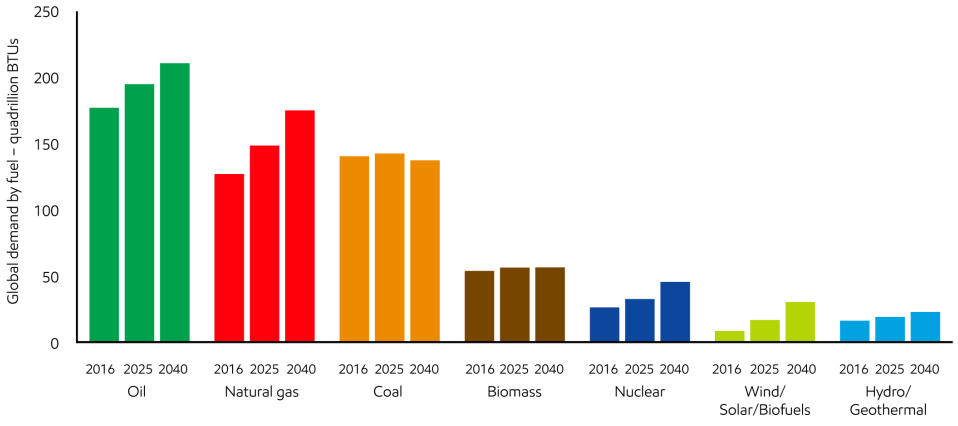

Figure 1.1: The trend of the world's energy supply to meet diverse demand [1].

Combustion is defined as an exothermic chemical reaction causing the oxidization of fuel with a considerable heat release. These high-temperature reaction products can be utilized for direct power production (through their expansion in turbines or internal combustion engines) or cooled down transferring heat to a heat user or a working fluid. This apparently simple approach is limited by the tradeoff between combustion stability and pollutant emissions.

A flame can be seen as a thin gaseous zone where self-sustained combustion occurs. The structure and characteristics of flames can vary depending on the level of mixing in the reactants. One extreme is diffusion flames, in which fuel and oxidizer enter the combustion chamber as separate streams and react along a thin interface, known as the flame front, separating unburnt mixtures and products. The flame front is the region where a significant change in chemical composition occurs followed by heat release. The combustion process occurs at a local stoichiometric equivalence ratio in the flame front as the diffusion process (slower than the combustion process) is just able to replenish the oxidizer and fuel molecules consumed by the combustion process. Thus, the temperature of the reaction zone is usually very high and close to the stoichiometric flame temperature even if excess air is available. However, the superior stability characteristic of diffusion-flame combustors is the main reason behind implementing this mode of combustion in older gas turbine engines for power generation [2–4]. Due to the unacceptably high concentrations of NO_x pollutant emissions, this mode of combustion is no longer used in power generation engines nowadays [5]. On the other extreme are premixed flames, in which the fuel and oxidizer are perfectly mixed before entering the combustion chamber. Unlike diffusion flames, premixed fuel/oxidizer mixtures can be varied and usually set to a low equivalence ratio (lean mixture), in which the fuel is the limiting reactant. In lean premixed combustion (LPM), NO_x pollutant emissions are reduced because of the reduction of the flame temperature. Moreover, no soot formation in LPM combustion as these particles are only produced under rich mixture conditions (the oxidizer is the limiting reactant). Nowadays, the LPM technology is adopted in novel gas turbine engines in the power generation industry to replace diffusion flame combustors due to the ability to control the flame temperature and NO_x emissions. Nevertheless, this mode of combustion is prone to flame instabilities, blow-off, and flashback. The risk of flame extinction increases when operating a burner near the lean blow-off limit. Such an extinction requires shutdown and restart of the combustion process in gas turbine burners which may lead to thermo-fatigue damages. Flame extinction mechanism due to blow-off has been investigated in several experimental and numerical studies [6–12].

In most industrial applications, the ideal mixture of fuel and oxidizer is not fully achieved due to spatial and time of mixing limitations. Therefore, it is common to have non-uniform inhomogeneous mixture distribution in such devices, e.g. land-based gas

turbines, aero-engines, and automotive engines. Furthermore, in most practical devices combustion usually occurs in a turbulent flow regime and not a laminar one. The reason is that the effect of heat release induces flow instabilities in the forms of buoyancy and gas expansion that stem from the change in density of the fluid with the increase of flow temperature. Turbulence is of great importance because it enhances the mixing process and the flame speed propagation resulting in an increased power output [13]. To further study combustion in practical devices, turbulence, partial premixing, and stratification in flames must be considered.

1.2 Characteristics of turbulent combustion

When combustion occurs in a turbulent flow entering the flame front, the regime is described as turbulent combustion interaction. This mode of combustion is encountered in many practical applications including jet-engines, gas turbines, and internal combustion engines. Turbulent combustion stems from the interaction between turbulence, and chemistry. Turbulence alters the flame structure through enhancing mixing which may increase the chemical reaction rate, however, high levels of turbulence could also diminish the flame causing flame quenching. On the other hand, combustion can generate turbulence through heat release which induces strong flow accelerations causing fluctuations to the flame front.

1.2.1 Elementary descriptions of turbulence

Turbulence is a three-dimensional, unsteady, rotational fluid motion with broad-banded fluctuations of flow quantities (velocity, pressure, temperature, etc) occurring in both time and space. Turbulent flows are characterized by intensity fluctuations, length and time scales, fluctuating vorticity fields (highly unstable streaks and swirls, called eddies, that undergo distortion and spin), dissipation, molecular and thermal diffusivities, and non-dimensional numbers.

Turbulence can be considered to consist of coherent eddies of different sizes. There is no exact definition of a turbulent eddy, but it is characterized by coherent rotational structures formed as a result of the unsteady random fluctuations in the flow variables and exist in a certain region in space for a certain time. Those structures are subsequently destroyed as the kinetic energy is transferred from the largest to smallest scales (termed the turbulent energy cascade). The integral length scale l is defined as the largest size of eddies in the flow which is in the order of the size of the flow geometry. Eddies of size l have a characteristic velocity in the order of turbulence intensity u' and

an eddy turnover time defined as:

$$\tau = \frac{l}{u'} \tag{1.1}$$

The Turbulent Kinetic Energy (TKE) is defined as:

$$k = \frac{3}{2}u'^2 \tag{1.2}$$

At the smallest micro-scale of eddies, named the Kolmogorov length scale η, viscous effects dominate as the eddy energy is dissipated into thermal energy resulting in a temperature increase. This length scale is related to the dissipation rate ϵ of the turbulent kinetic energy k by the kinematic viscosity ν as follows:

$$\eta = (\frac{\nu^3}{\epsilon})^{1/4} \tag{1.3}$$

This dissipation rate is estimated as the ratio of the kinetic energy and the eddy turnover time and expressed as:

$$\epsilon = \frac{u'^3}{l} \tag{1.4}$$

The velocity and time scales associated with the Kolmogorov length scale are defined as:

$$u_\eta = (\nu\epsilon)^{1/4} \tag{1.5}$$

$$\tau_\eta = (\frac{\nu}{\epsilon})^{1/2} \tag{1.6}$$

1.2.2 Key non-dimensional parameters in combustion

Non-dimensional numbers are essential in the identification of combustion regimes. The turbulent Reynolds number is a measure of the ratio of inertial forces to viscous forces based on the integral length scale:

$$Re_T = \frac{u'l}{\nu} \tag{1.7}$$

Damköhler number is the ratio between the turbulent flow time t_T and the chemical kinetic time scale t_c and it is given by:

$$Da = \frac{t_T}{t_c} \tag{1.8}$$

Low values of Damköhler number (Da < 1) indicate that the flame is altered by all scales of turbulence and the chemical reactions are slow. On the other hand, high values (Da $>> 1$) mean that the chemical reaction is faster than the eddy turnover time and the flame structure is not affected by turbulence.

The Karlovitz number is the ratio of the chemical kinetic time scale to the Kolmogorov time scale:

$$Ka = \frac{t_c}{t_\eta} \tag{1.9}$$

Low values of Karlovitz number (Ka < 1) imply that turbulence is too slow compared to chemistry and the flame front is not affected. In contrast, high values (Ka > 1) indicate that the flame structure is affected by turbulence because the turnover time of Karlovitz eddies is faster than the chemical reactions.

Other non-dimensional numbers that relate molecular, thermal and momentum diffusivities are Lewis number (Le), Prandtl number (Pr), and Schmidt number (Sc) which are defined respectively as:

$$Le = \frac{\alpha}{D} \tag{1.10}$$

$$Pr = \frac{\nu}{\alpha} \tag{1.11}$$

$$Sc = \frac{\nu}{D} \tag{1.12}$$

where D is the molecular diffusivity, and α is the thermal diffusivity.

1.2.3 Flame regimes

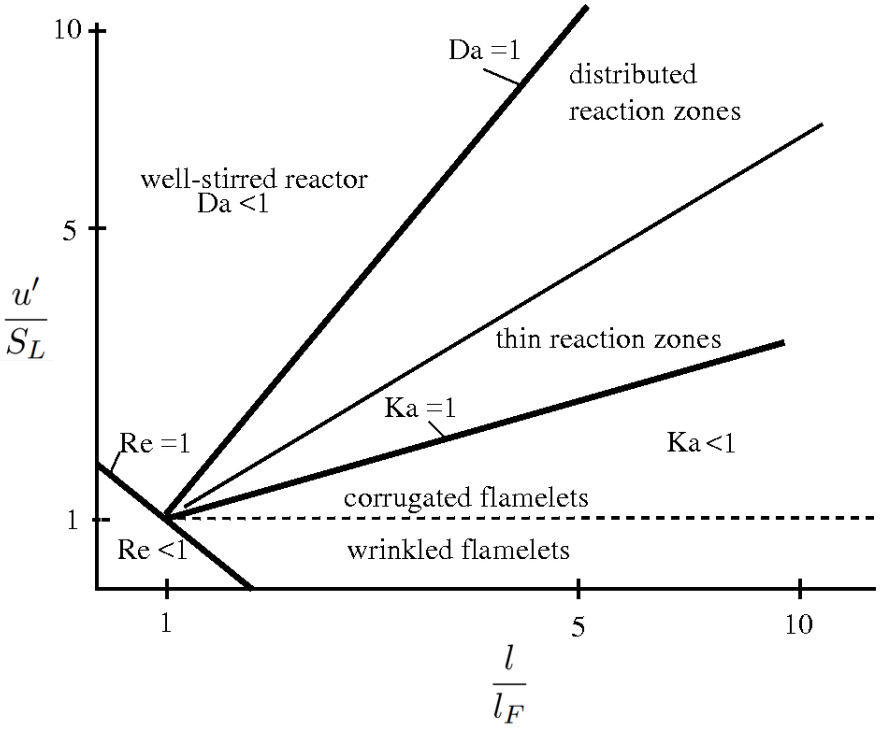

Figure 1.2: The Borghi diagram for regimes of turbulent premixed combustion [14].

The main characteristics of turbulent premixed flames are controlled by the mass fraction of fuel in the mixture and by the interaction between the laminar flame front with multi-scale eddies ranging from the Kolmogorov length scale (l_η) to the integral length scale (l). Hence, turbulence-chemistry interactions can be defined based on the three key non-dimensional parameters Re_T, Da, and Ka. Different flame regimes have been identified in terms of length (l/l_F) and velocity ratios (u'/S_L) by Borghi diagram [14], shown in Figure 1.2, where l_F is the laminar flame thickness and S_L is the laminar flame speed. This diagram identifies the laminar and turbulent combustion regimes. The latter one can be divided further into four regions depending on the values of Da and Ka. The diagram is explained as follows:

1. The first regime is the *laminar combustion regime* occurring for $Re_T < 1$ which is characterized by a very thin flame thickness ($l_F \approx 0.1 - 0.2mm$) and a relatively low flame speeds ($S_L \approx 0.3 - 0.5m/s$).

2. *Wrinkled flamelet regime*: occurs when $u' < S_L$ (turbulence intensity is lower than the laminar flame speed), the reaction sheet is wrinkled by the interaction of large eddies with the flame front. However, none of the eddies penetrates the flame zone.

3. *Corrugated flamelet regime*: occurs when $u' > S_L$ (turbulence intensity is higher than the laminar flame speed) and $Ka < 1$. This small Karlovitz number implies

that the flame thickness is much smaller than the Kolmogorov length scale, thus eddies are able to enter the flame zone but can not penetrate the internal reaction sheet.

4. *Thickened flame regime*: $Ka > 1$, $Da > 1$ and $t_T > t_c > t_\eta$, that is the turbulent integral time scale is larger than the chemical time scale which is larger than the Kolmogorov time scale. In this case, the smallest eddy l_η is smaller than the laminar flame thickness l_F, so the structure of the flame zone is thickened by the small turbulent eddies, and it cannot be considered as a laminar flamlet anymore, leading to the formation of pockets of fresh and burnt mixture in the reaction zone. The flame front is substantially wrinkled, and the Kolmogorov eddies increase the diffusion within the flame front so that thickened flamelets are formed as a result of the increase in the flame front thickness. Thus, for this regime, the flame and turbulent characteristics are implicitly dependent, and turbulence and combustion cannot be dissociated.

5. *Well-stirred reactor regime*: $Da < 1$ that indicates the flame is altered by all scales of turbulence and the chemical reactions are slow resulting in the formation of various distributed reaction zones. Therefore, the combustion process is controlled by the chemical kinetics without the existence of a distinct flame front.

Most practical applications fall in the transition region between the thin and distributed reaction zone regimes. Moreover, volumetric engines (e.g. internal combustion engines) typically lay in the corrugated and wrinkled flame region. Figure 1.3 depicts the schematics of the different four turbulent premixed combustion regimes proposed by Borghi.

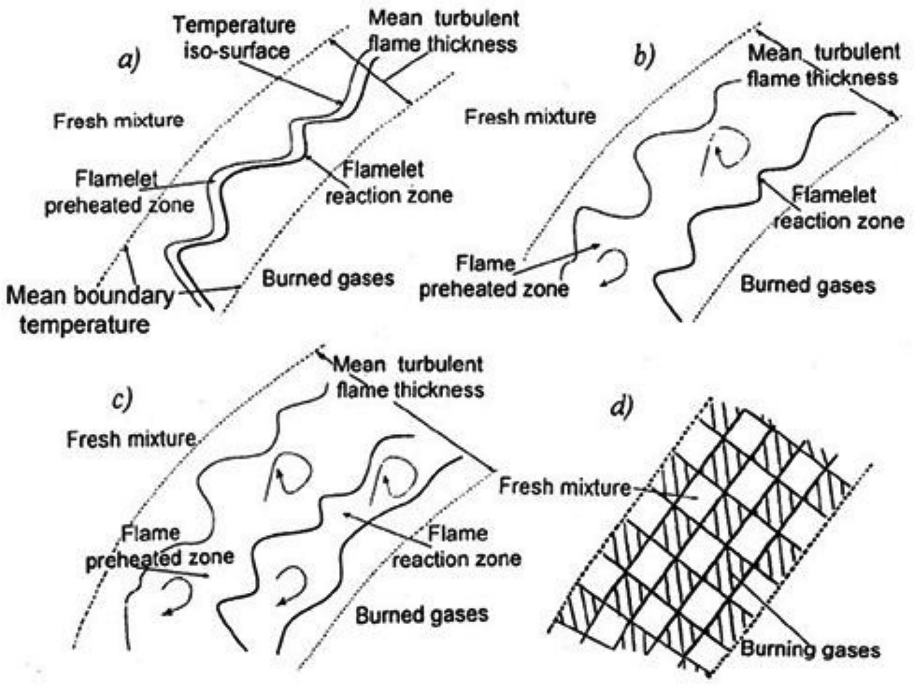

Figure 1.3: Schematics of four turbulent premixed combustion regimes proposed by Borghi: a - wrinkled flamelet regime; b - corrugated flamelet regime; c - distributed reaction zones; d - well-stirred reactor [15].

1.3 Stratified flames

Partially-premixed flames refer to the flames that consist of compositionally inhomogeneous mixtures. The flames contain pockets or zones of a rich premixed fuel-oxidizer mixture, and for complete combustion to occur, the transport of oxidizer from other pockets or zones that contain an oxidizer-rich mixture is required. Partial combustion takes place in fuel-rich zones while the remaining unburned reactants and/or intermediate species are consumed in the oxidizer-rich zones of the mixture. Therefore, the local equivalence ratio in partially-premixed flames is greater than unity in one zone of the mixture and less than unity in another portion. With such non-uniformity in the flow field, the mixture can include flammable and non-flammable fluid.

Stratified flames are defined as partially-premixed flames propagating through a mixture that is within the flammability limits [16]. Perfect mixing is difficult to achieve in practical power generation devices due to combustion instabilities and mixing lengths limitations. However, such stratification in the mixture distribution may also be intentionally introduced to mitigate emissions, decrease throttling losses, and extend the operational range as is the case in direct-injection engines [17–21]. For example, in a stratified-charge spark-ignition engine, the fuel is directly injected inside the cylinder in

such a way that the fuel-air mixture presents different equivalence ratios inside the combustion chamber when the charge is ignited. In particular, the charge is stratified with a local rich composition in the vicinity of the spark-plug electrode while its composition averaged over the cylinder volume is lean. The advantages of such stratification are:

- Combustion begins in the richer part of the charge with a consequent high speed. Later, when the flame front is fully turbulent, it burns leaner parts, thus the overall mixture composition is lean which results in improvement of engine efficiency and completeness of the oxidation reactions.
- The burning process is influenced only by the local air-to-fuel ratio, similar to Diesel engines. Therefore, the load can be controlled by varying the amount of injected fuel (the overall air-to-fuel ratio), eliminating the pumping losses caused by throttling.
- Heat losses through the combustion chamber walls are reduced because the excess air forms an insulating layer between the hot gases and the chamber walls.
- Higher compression ratios (>12) can be achieved since the late injection reduces the residence time of the mixture at high temperature and pressure.

Furthermore, this mode of combustion is usually present in lean premixed (LP) or lean premixed prevaporized (LPP) combustors in gas turbines. There have been a few studies to understand the effect of stratification on the stability limits, pollutant emissions, and flame structure of lean premixed combustors [22–24], although it is an important phenomenon that can be purposely introduced or can occur due to spatial and temporal limitations. Therefore, some fundamental issues are still not fully understood. For example, when a stratified flame burns from locally stoichiometric to lean conditions (back-supported flame), the flame can achieve higher flame speed and the flammability limit is extended compared to the homogeneous counterparts [25]. This can be justified by higher gas temperatures behind the flame front in the preheat zone, which affect chemical kinetics as well as heat and mass transport. However, the implication of this such effect on the turbulent stratified flame modelling is still an open question.

For a better understanding of stratified combustion, a series of workshops on Measurement and Computation of Turbulent Nonpremixed Flames (TNF) was established to facilitate collaboration between experimental and computational researchers in the field of turbulent combustion. The TNF Workshop series was initiated to address validation of RANS based models for turbulent nonpremixed flames, as well as partially premixed flames where combustion occurs mainly in a diffusion flame mode. Although the title of the workshop stayed the same, its scope has expanded since TNF9 (Montreal, 2008) to include other research topics such as mixed-mode and stratified combustion. Among

the various activities of the TNF Workshop, two well-known burners have been designed to provide experimental measurements support to numerical models improvement and validation which are: the Darmstadt turbulent stratified flame (TSF) burner and Cambridge stratified swirl burner (SwB) as shown in Figure 1.4. In this thesis, only the Darmstadt TSF burner will be considered.

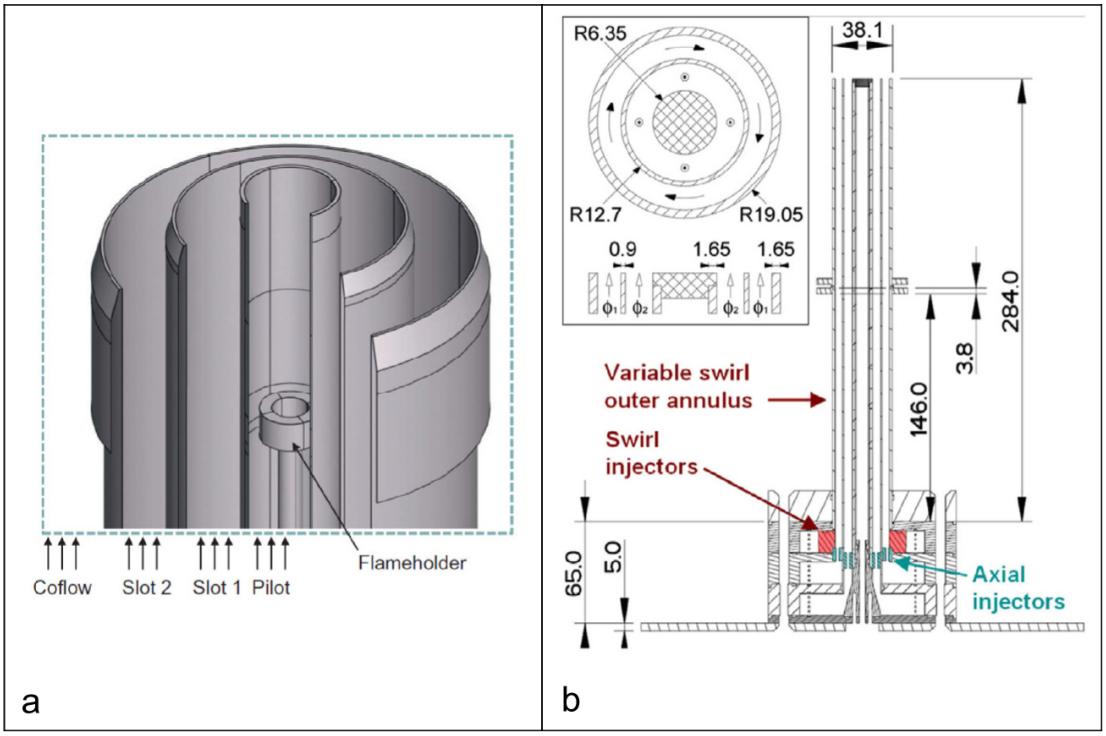

Figure 1.4: Schematics of two high-turbulence ((a) and (b)) stratified burners: (a) Darmstadt turbulent stratified flames (TSF) burner [26], (b) Cambridge stratified swirl burner (SwB) [27].

1.4 Objective and outline

The objective of this thesis work is to assess the Flame Area model proposed by Weller [28] on controlled combustion conditions, with both stratified and homogeneous premixed fuel-air mixtures. Also, this work aims at understanding the differences in performance between the one-equation and tow-equations Weller model. Algebraic closure correlations are used for the flame wrinkling factor, such as Gulder, Peters, and Muppala ones, in the context of the one-equation Weller model; instead, a transport equation is solved for the flame wrinkling factor in the two-equations model version. A preliminary assessment of the Choi-Huh version of the Coherent Flamelet Model (CFM) [29] will also be conducted. The TU-Darmstadt turbulent stratified flame (TSF) burner is selected for these assessments, with the steady-state methane-air flames A-r (premixed stratified) and G-r (premixed homogeneous) as chosen configurations. The intention of this fundamental analysis is to support turbulent engine combustion modelling strategies, where it is more complex to clarify the differences between the aforementioned

modelling approaches. This study also focuses on understanding the limitations of these different models when dealing with stratified flames and turbulent jet flows.

The two combustion models were initially implemented and validated for engine applications [30]. Part of this thesis was dedicated to modifying both combustion solvers from being applied for engine applications into fixed volume cases (e.g. burners and combustors) with the implementation of some new algebraic closure correlations in OpenFOAM.

The thesis text is divided into five chapters apart from the Introduction Chapter as follows:

- **In Chapter 2:** a detailed description of the Darmstadt TSF burner set-up is be presented, along with the operating conditions of target flames.
- **In Chapter 3:** a brief introduction of the main thermo and fluid-dynamics equations governing reacting flows is presented, followed by a theoretical background of turbulence modelling and a detailed explanation of the combustion models used in this thesis.
- **In Chapter 4:** an explanation of the numerical setup of the TSF burner along with the mesh generation and numerical schemes is presented.
- **In Chapter 5:** the main results achieved for the assessment of the Weller flame area combustion model on the TSF burner are included and discussed. First, the non-reacting case A-i2 is validated. Then the reactive cases A-r and G-r are simulated using the one-equation and two-equations Weller model, and a comparison between these versions of the model is conducted. After that, NO_x profiles are compared for both flames under the adiabatic assumption and finally a preliminary assessment of the CFM model is carried out.
- **In Chapter 6:** conclusions of the work are drawn along with possible future outlooks.

Chapter 2

The Darmstadt Turbulent Stratified Flames

In Chapter 2, a detailed description of the Darmstadt TSF burner set-up will be presented, along with the operating conditions of target flames.

2.1 Experimental setup and burner configuration

The Darmstadt TSF burner was designed by the Technical University of Darmstadt to provide a database for stratified flames to validate and examine numerical combustion models [31]. This burner mimics the condition in real burners in industrial applications where flames are typically turbulent, lean premixed and stratified. It is relevant for aircraft combustors where new low-emission engine designs increasingly call for some premixed burning supported by a more stable pilot flame. Moreover, it demonstrates a variety of operating conditions that involve shear and stratification in flames. Both reacting and non-reacting flows have been examined. The design criteria for this burner were:

- unlimited optical access by an open flame;
- simple inflow conditions by fully developed pipe turbulence;
- a central pilot for flame stabilization;
- independent control of shear and stratification in the turbulent mixing layer by two concentric feed lines;
- high Reynolds numbers.

Among the different scenarios of intentional charge stratification for statistically stationary conditions is *lean-lean stratification*, where the two streams enter the combustion chamber at initially different equivalence ratios at lean conditions. This scenario is observed even in simple unconfined premixed flames, where a perfect fuel–air stream mixes with co-flowing air.

The experimental test rig of the Darmstadt TSF burner is characterized by three staged co-flow concentric tubes for optical access. The schematic diagram shown in Figure 2.1 represents the Darmstadt burner configuration.

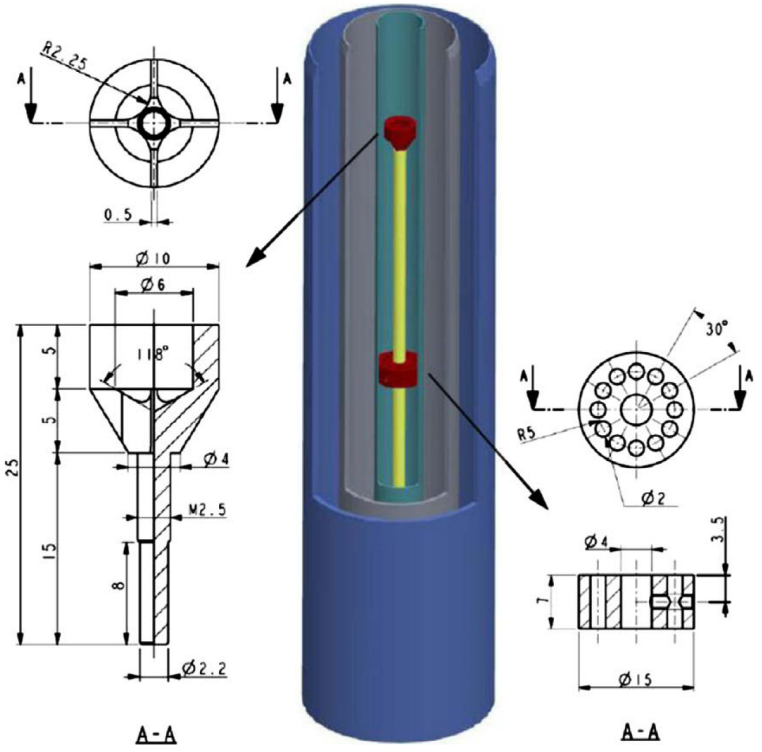

Figure 2.1: 3D model of the experimental rig of the Darmstadt TSF burner, characterized by a central ceramic tube (Pilot) and two co-axial steel pipes (Slot 1 and 2, respectively). The flame holder and the turbulence enhancing perforated plate are highlighted inside the Pilot. Technical drawings of: the flame holder (left) and the turbulence enhancing perforated plate (right) [31].

The corresponding diameters from the central inner tube to the outer tube are 14.8 mm, 37 mm, and 60 mm, respectively.

The central tube is the pilot where the ignition process occurs nearby the flame holder, which is set 40 mm inside and upstream of the pilot exit to stabilize the pilot flame. The hot burnt products are released at the pilot exit which provides the heat required to ignite the surrounding fresh mixture just after its exit section.

The other two annular slots (slots 1 and 2), as shown in Figure 2.2, supply a fresh fuel-air mixture to sustain the main flame. These slots can be operated independently

from the pilot and thus different configurations of shear and stratification can be obtained by varying the equivalence ratio inside each slot.

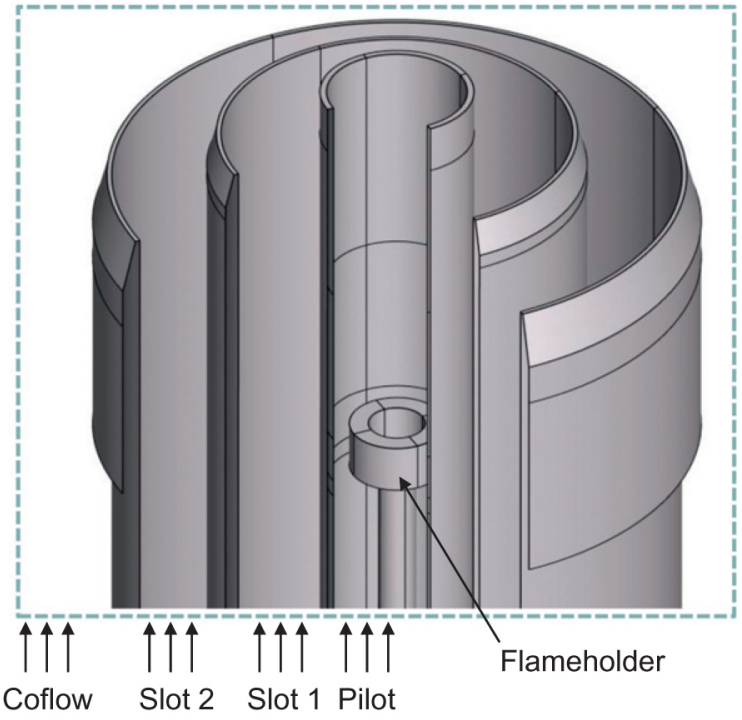

Figure 2.2: Cut out of the geometry at the pip exit region [26].

The minimum tube length of the slots is 500 mm (about 25 hydraulic diameters of the tubes), and slots 1 and 2 tubes have 16 and 24 radial drill holes of 5 mm diameter at the tubes' inlets, respectively, to ensure a fully developed turbulent flow at the tubes exit.

Moreover, the burner is placed inside a 600 mm-wide air co-flow with an axial bulk velocity of 0.1 m/s. The reason is to shield the flames from the surrounding environment and prevent dust penetration which disturbs 1D Raman/Rayleigh scattering measurements, because it prevents dust-induced optical breakdown and reduces background illumination from Mie scattering.

It is worth mentioning that experimental techniques which were used to analyze the stationary conditions of lean-lean charge stratification are:

- Laser Doppler Velocimetry (LDV) for flow velocity components.
- 1D Raman/Rayleigh scattering for species mass fractions and temperature.

For further details about the experimental measurement techniques and procedures for the flow field, one can refer to the article published by Seffrin et al. [31].

2.2 Flames properties and operational conditions

Stratification and shear can be controlled by varying the equivalence ratio (ϕ) and the axial bulk exit velocity (U_y), respectively, in the burner pipes. Several combinations of flame series (named from A to K) with stratification and shear were experimentally carried out, as shown in Figure 2.3. In case there are identical equivalence ratios in both annular slots, the flames are termed "without stratification" and for cases of identical bulk exit velocities, "without shear".

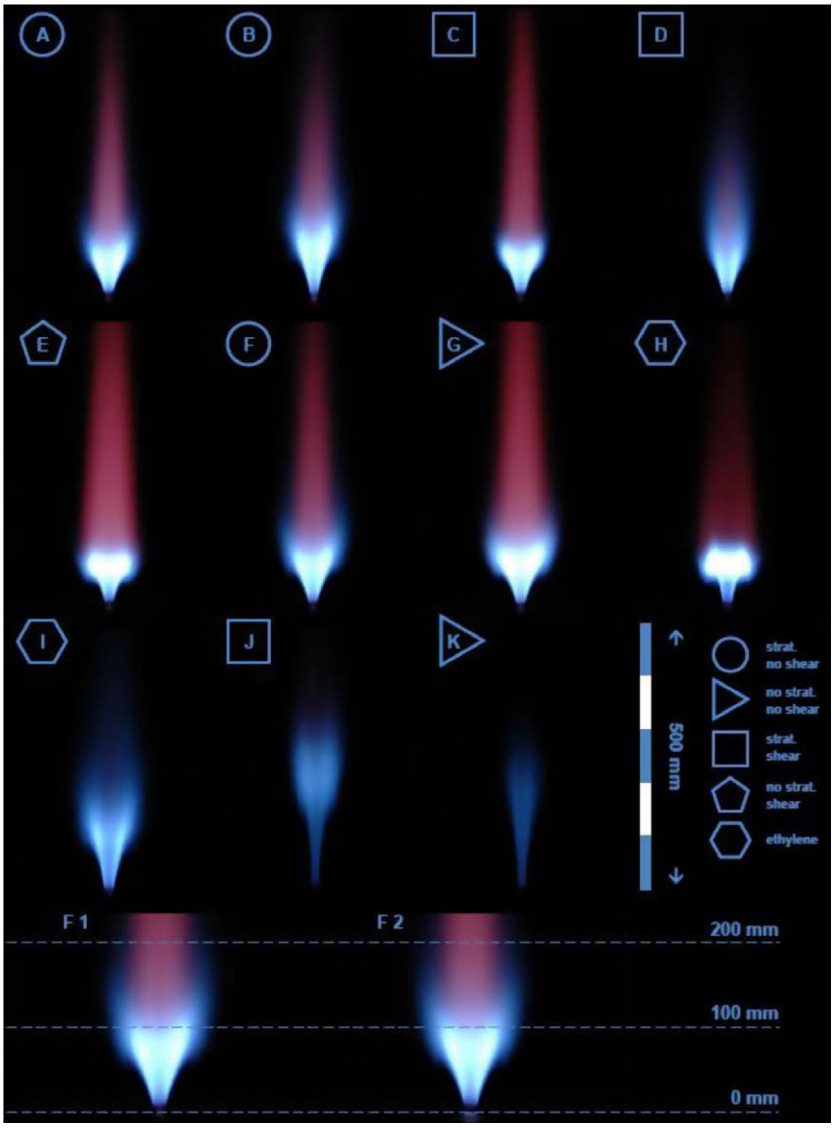

Figure 2.3: Photographs of each reacting condition tested on the TSF burner. The last row shows configuration F for the original burner (F1) and a duplicate (F2), demonstrating the good reproducibility of the technical construction [31].

In the present work, the isothermal flow case (A-i2) and the reactive cases (A-r and G-r) are simulated. The main information for these cases is summarized in Table 2.1.

Case	ϕ_{pilot}	ϕ_{slot1}	ϕ_{slot2}	u_{pilot}	u_{slot1}	u_{slot2}	Re_{pilot}	Re_{slot1}	Re_{slot2}	u_{coflow}
A-i2	0	0	0	10	10	10	9,800	13,800	13,300	0.1
A-r	0.9	0.9	0.6	1	10	10	980	13,800	13,300	0.1
G-r	0.9	0.9	0.9	1	10	10	980	13,800	13,300	0.1

Table 2.1: Flow parameters for the 3 cases simulated in the present work. Equivalence ratios ϕ (–), bulk velocities u (m/s), Reynolds numbers Re (–) (based on the bulk velocity and hydraulic diameter). All bulk velocities are calculated using the unburnt gas density and the corresponding tube exit area.

The isothermal non-reacting case A-i2 is always used as a test case for flow field prediction and as a measure of mesh quality performance. The reacting case A-r was considered because it has the most complete experimental data among all other TSF cases which includes time-averaged mean value and variance of flow field parameters and major scalars. A-r is the reactive case which includes the generation of turbulent stratified flame by varying the equivalence ratios in the annular slots. Finally, the fully premixed reactive G-r case is simulated to have a qualitative comparison with flame A-r and understand the effect of stratification and NO_x formation in both cases. These last two cases were used to assess the performance of the different combustion models presented in this thesis.

The inlet velocity is the same in all cases (10 m/s) except for the pilot. The pilot velocity of the cold flow case A-i2 is set to be 10 m/s to simulate the flow speed for the ignited flame in the pilot. For the reacting case A-r, the stratification is achieved by supplying a methane-air mixture with an equivalence ratio of 0.9 in the inner slot whereas the outer slot has an equivalence ratio of 0.6. The core flame initiated in the pilot will be in a premixed condition since the pilot and the inner slot (slot 1) have similar equivalence ratios. In fact, for the reacting case A-r, the inlet velocity of Pilot fresh mixture (1 m/s) is calibrated in order to achieve a burnt gases velocity which approximately matches the U_y value of surrounding fresh mixture (10 m/s). This is performed with the final purpose to minimize the shear between Pilot and Slot 1. The stratification is anticipated to occur at a relative downstream area where the flame front proceeds from a near-stoichiometric mixture to a leaner mixture leading to back-support combustion. Differently from case A-r, the equivalence ratio in the pilot and the inner and outer slots is kept the same ($\Phi = 0.9$) in case G-r to ensure that fully premixed homogeneous conditions are achieved.

Measurements planes for the cold flow case A-i2 and the reactive case A-r, where velocity, species mass fractions, and temperature were evaluated, are shown in Figure 2.4. Compared to case A-r, measurements for case G-r have been recorded at slightly different planes that will be presented in Chapter 5.

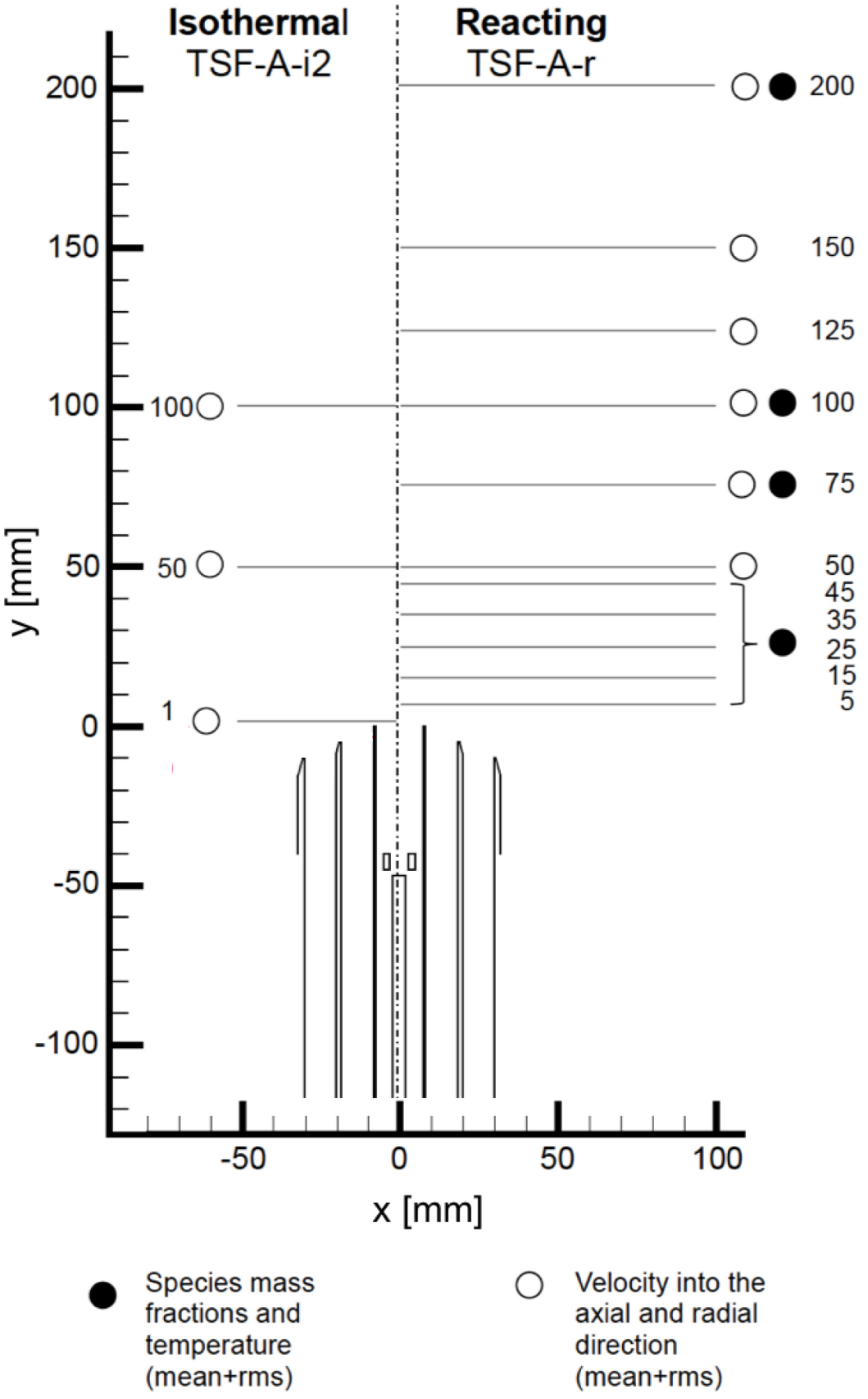

Figure 2.4: Positions of the measurement planes for the isothermal case A-i2 (left) and reactive case A-r (right) to illustrate where data is evaluated.

Based on the experiment measurements [31], the Karlovitz number value of the reacting case A-r is estimated to be around 1.2 to 2.1 and its Damkohler number is about 50 to 80. This estimation is based on the turbulent kinetic energy and the integral length scale resulting from the PIV measurements. These parameters were evaluated along the mean flame position as shown on the left in Figure 2.5.

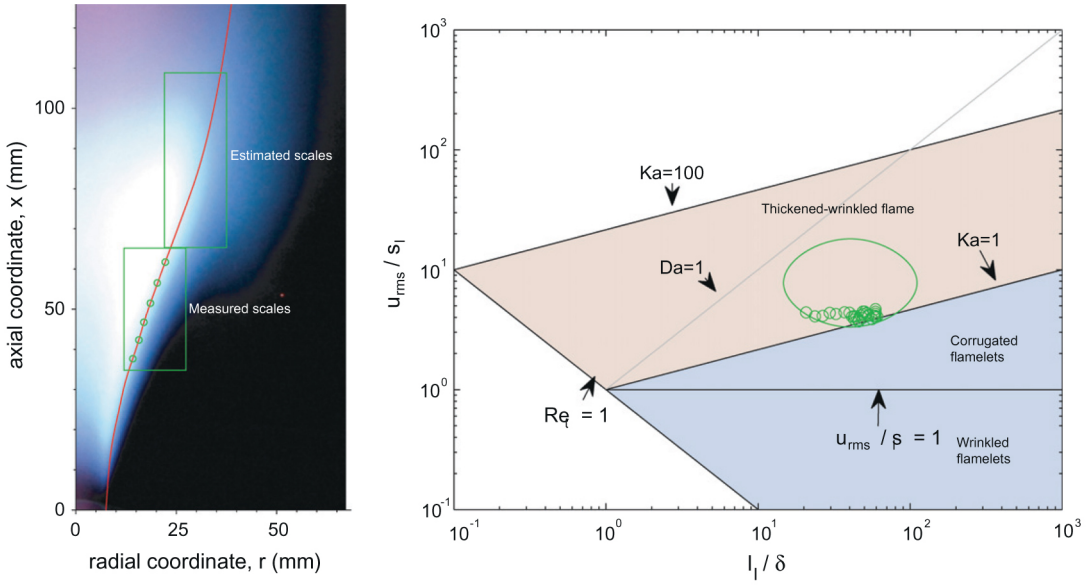

Figure 2.5: Regime diagram classification of the reacting case A-r. Left: flame photograph with the mean flame position highlighted in red. Right: Regime diagram with the classification based on measurements (circles) and estimated scales further downstream (ellipse) [26].

The turbulent integral time scale is larger than the chemical time scale which is larger than the Kolmogorov time scale. This indicates that the reaction in the reactive case A-r proceeds relatively fast. As shown in Figure 2.5, the flame is classified as thickened-wrinkled with a relatively thick flame front that can be affected by small length scale eddies. The Klimov-Williams criterion for the flamelet regime definition is shown by the blue shaded region in Figure 2.5. However, DNS studies by Poinsot et al. [32] showed that the Klimov-Williams criterion underestimates the flamelet regime by more than an order of magnitude. The authors argued that the flame stretch is not affected significantly even in case where the Kolmogorov eddies can penetrate the flame thickness. Those eddies can be too small or decay too rapidly (due to viscous effects) to stretch the flame significantly. Poinsot et al. [32] proposed an extended definition of the flamelet regime based on the existence of an active (not quenched) continuous flame front that separates the fresh and burnt mixtures, and small eddies can alter the integral structure without leading to quenching of the flame.

Chapter 3

Computational Theory

This chapter gives a brief introduction of the main thermo and fluid-dynamics governing equations for the numerical modelling of turbulent reacting flows. Also, a theoretical background of turbulence modelling and a detailed explanation of the combustion models used in this thesis are presented.

3.1 Introduction

Computational fluid dynamics (CFD) is the science of predicting and analyzing systems involving fluid flow, heat transfer, and related phenomena such as chemical reactions by means of computer-based simulation software. Simulations using CFD are very powerful tools in describing phenomena within industrial and non-industrial applications. Some areas of their applications are turbomachinery, internal combustion engines, aerodynamics, weather prediction, and biomedical engineering. In this thesis, CFD is applied to the Darmsdtat TSF burner to understand the capabilities of the combustion models in predicting the flow fields. The chosen burner is relevant for aircraft combustors in that modern low-emission engine designs increasingly call for some premixed burning supported by a more stable pilot flame.

One of the quintessential methods for manufacturers to comply with such low-emission standards is to further optimize the combustion process. This requires a proper understanding of the turbulence-chemistry interaction in such combustion processes. Such understanding can only be achieved by combining advanced experimental techniques and detailed multi-dimensional simulations. Although experiments are essential sources in providing real-world data, they are usually expensive and have some limitations in providing information on certain aspects of the physical phenomena. On the other hand, CFD analysis is comparatively inexpensive and can provide useful data that can aid the design process. It can also be used to investigate a range of physical

phenomena that may be inaccessible using conventional experimental methods. It can be considered as a non-destructive test and permits to predict the flow field simulating the most extreme conditions and performing a wide range of parametric and sensitivity analysis. Therefore, they are very powerful tools that can be utilized for predicting the performance of new designs prior to the production of prototypes. Nevertheless, their performance should be validated first against experimental measurements.

3.2 Governing equations

The basis for the CFD analysis of turbulent reacting flows lies in four quintessential equations governing the flow of fluid. These equations are the conservation of mass, species, momentum, and energy that represent the transport equations.

Conservation of mass

The conservation of mass principle states that the total mass of the system can not be created or destroyed. This principle is the same for both non-reacting and reacting flows (combustion does not generate mass) and can be expressed by the continuity equation:

$$\frac{\partial \rho}{\partial t} + \nabla \cdot (\rho \boldsymbol{v}) = 0 \tag{3.1}$$

Where ρ is the density of the fluid and $\boldsymbol{v}$ is the velocity vector field.

Conservation of species

For modelling reacting flows, the transport equation of species must be considered along with the continuity equation. Also, the reaction term must be taken into account. The mass conservation equation for species k is written as:

$$\frac{\partial \rho Y_k}{\partial t} + \nabla \cdot (\rho(\boldsymbol{V_k} + \boldsymbol{v})Y_k) = \dot{\omega}_k \qquad k = 1, ..., N_s \tag{3.2}$$

Where $\dot{\omega}_k$ is the chemical reaction rate of the single species and $\boldsymbol{V_k}$ is the diffusive velocity of species k. By definition, the summation of all diffusive fluxes is equal to zero and from equation 3.1 the mass produced per unit volume and time is balanced by the mass consumed, thus the sum of the chemical reaction rates of total number of species (N_s) becomes zero ($\sum_{k=1}^{N_s} \dot{\omega}_k = 0$).

The diffusive velocity $\boldsymbol{V_k}$ of species k can be estimated by the Hirschfelder and Curtiss approximation [33] as:

$$\boldsymbol{V_k} Y_k = -D_k \nabla Y_k \tag{3.3}$$

Where D_k is the diffusion coefficient of species k into the rest of the mixture. This coefficient can be linked to the Lewis number (L_k) of individual species defined as the ratio between thermal diffusivity and species diffusion:

$$L_k = \frac{\lambda}{\rho C_p D_k} \tag{3.4}$$

Hence, the final form of the species conservation equation can be expressed as:

$$\frac{\partial \rho Y_k}{\partial t} + \nabla \cdot (\rho \boldsymbol{v} Y_k) - \nabla \cdot (\frac{\lambda}{L_k C_p} \nabla Y_k) = \dot{\omega}_k \tag{3.5}$$

Conservation of momentum

The momentum conservation, in differential form, is a force equilibrium equation applied to an infinitesimal volume of fluid. This equation is the same in reacting and non-reacting flows:

$$\frac{\partial \rho \boldsymbol{v}}{\partial t} + \nabla \cdot (\rho \boldsymbol{v} \boldsymbol{v}) = -\nabla p + \nabla \cdot \overline{\overline{\boldsymbol{\tau}}} + \rho \boldsymbol{F} \tag{3.6}$$

Where the left-hand side of the equation represents the accumulation of momentum over time and the change of momentum flux, respectively. This total variation of momentum is balanced by the gradient of pressure, the viscous dissipation and the external body forces. $\overline{\overline{\boldsymbol{\tau}}}$ is the stress tensor while $\boldsymbol{F}$ is the body forces which is mainly the contribution of gravity term ($\rho \boldsymbol{g}$) in this study.

For a Newtonian fluid, the viscous stress tensor is proportional to the velocity gradient as follows:

$$\tau_{ij} = \mu(\frac{\partial v_i}{\partial x_j} + \frac{\partial v_j}{\partial x_i}) - \delta_{ij} \frac{2}{3} \mu \frac{\partial v_i}{\partial x_i} \tag{3.7}$$

Where μ is the dynamic viscosity and δ_{ij} is the Kronecker delta.

Although the momentum conservation equation is the same with and without combustion, the flow behavior is different because the flow is modified by combustion; the thermodynamic parameters strongly changes with temperature. As a result, the local Reynolds number changes relatively compared to non-reacting flows.

Conservation of energy

The conservation of energy principle is based on the first law of thermodynamics which states that energy can neither be created nor destroyed; energy can only be transferred or changed from one form to another. This principle can be expressed as follows:

$$\frac{\partial \rho h_t}{\partial t} + \nabla \cdot (\rho \boldsymbol{v} h_t) = \frac{\partial p}{\partial t} - \nabla \cdot \boldsymbol{q} + \nabla \cdot (\overline{\overline{\boldsymbol{\tau}}} \cdot \boldsymbol{v}) + \dot{Q} + \rho \sum_{k=1}^{N_s} [Y_k \boldsymbol{f}_k \cdot (\boldsymbol{V_k} + \boldsymbol{v})] \quad (3.8)$$

Where h_t is the total enthalpy defined as $h_t{=}e_t + p/\rho$. The heat source term ($\dot{Q}$) can be, for example, due to an electric spark or a radiative heat flux, and it is different from the heat released by combustion. The term $\rho \sum_{k=1}^{N_s} [Y_k \boldsymbol{f}_k \cdot (\boldsymbol{V_k} + \boldsymbol{v})]$ is the power produced by volume forces $\boldsymbol{f}_k$ on species k. The heat flux $\boldsymbol{q}$ is defined by a heat diffusion term and a term associated with the diffusion of species with different enthalpies which is specific of multi-species gas:

$$\boldsymbol{q} = -\lambda \nabla T + \rho \sum_{k=1}^{N_s} \boldsymbol{V_k} Y_k h_k \quad (3.9)$$

3.3 Turbulence modelling

3.3.1 Introduction to turbulence

The flow regime in the majority of turbo-machines involves turbulence, which can be described by a three-dimensional, unsteady, rotational fluid motion with broad-banded fluctuations of flow quantities (velocity, pressure, temperature, etc) occurring in both time and space. Turbulence consists of a spectrum of different scales (eddy sizes). There is no exact definition of a *turbulent eddy*, but it is characterized by coherent rotational structures formed as a result of the unsteady random fluctuations in the flow variables and exist in a certain region in space for a certain time. These structures are subsequently destroyed as kinetic energy is transferred from the largest to smallest scales (termed the turbulent energy cascade). It has a characteristic velocity and length (called a velocity and length scale). The largest eddies are of the order of the flow geometry. At the smallest micro-scale of eddies, named the Kolmogorov scale, viscous effects dominate as the eddy energy is dissipated into thermal energy resulting in a temperature increase.

Turbulence is chaotic in nature but it is deterministic and is described by the Navier-Stokes equations.

The numerical description of such a set of mathematical equations are:

- **Direct Numerical Simulations (DNS):** the full instantaneous Navier-Stokes equations are solved without any model for turbulent fluxes. The computational grid has to be refined enough to capture the smallest length scales in the domain. Although this is the most accurate method, it implies a very high computational cost and thus it is usually still limited to simple academic flow studies.
- **Large Eddy Simulation (LES):** Only large scales are explicitly solved directly without modelling but a subgrid model is still required to take into account the effects of small turbulent scales in the field using semi-empirical closure rules.
- **Reynolds Averaged Navier Stokes (RANS):** This technique involves ensemble averaging of the Navier-Stokes equation and it models all turbulent scales motion. As a result, the computational time and cost are relatively low allowing it to be the most used method in industrial applications nowadays.

Figure 3.1 shows comparative results obtained by the different approaches.

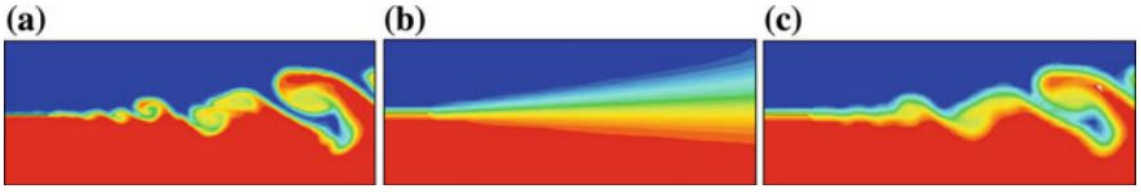

Figure 3.1: Comparative results from a) DNS, b) RANS, and c) LES.

3.3.2 Reynolds-averaged Navier-Stokes (RANS) equations

Each flow quantity is assumed to be written as the summation of a mean (1 st order statistics) and a fluctuating component over time t and space $\boldsymbol{x}$:

$$\phi(\boldsymbol{x}, t) = \overline{\phi}(\boldsymbol{x}, t) + \phi'(\boldsymbol{x}, t) \tag{3.10}$$

Where ϕ represents any flow quantity in the field (e.g. velocity components and pressure); $\overline{\phi}$ and ϕ' are the mean and fluctuating values of the flow quantity, respectively. Reynolds averaging is given by:

$$\overline{\phi}(\boldsymbol{x},t) = \lim_{N\to\infty} \frac{1}{N} \sum_{i}^{N} \phi_i(\boldsymbol{x},t) \tag{3.11}$$

The identification between ensemble and time averages is particularly feasible for statistically stationary processes, whose statistics are invariant to a time shift. The ensemble-average can be used in many unsteady flows, i.e. driven by unsteady boundary conditions.

Inserting equation 3.14 into the continuity equation (3.1) and the momentum equation we obtain the *time-averaged* Navier-Stokes equations

$$\frac{\partial\, \overline{\rho}}{\partial x_i} + \nabla \cdot (\overline{\rho}\, \overline{\boldsymbol{v}}) = -\nabla \cdot (\overline{\rho' \boldsymbol{v}'}) \tag{3.12}$$

The unclosed term between velocity fluctuation and density $\overline{\rho' \boldsymbol{v}'}$ acts as a mass source term for the mean flow quantities ($\overline{\rho}$,$\boldsymbol{v}'$) and need to be modelled which is awkward to be handled in CFD codes. Reynolds averaging for variable density flows introduces many other unclosed relations between flow quantities fluctuation and density ($\overline{\rho'\phi'}$). To avoid this difficulty, Favre average (mass-weighted average) was introduced as:

$$\widetilde{\phi} = \frac{\overline{\rho\phi}}{\overline{\rho}} \tag{3.13}$$

The, any flow quantity ϕ can be written as:

$$\phi(\boldsymbol{x},t) = \widetilde{\phi}(\boldsymbol{x},t) + \phi''(\boldsymbol{x},t) \quad with \quad \widetilde{\phi''(\boldsymbol{x},t)} = 0 \tag{3.14}$$

Applying this formulation for the conservation equations will result in the introduction of some turbulent fluxes terms that need to be closed.

3.3.3 Unclosed terms in Favre-averaged conservation equations

The objective of turbulent combustion modelling is to propose closures for the unknown quantities resulted from the Favre-averaged method for the conservation equations. Some of these terms are:

- **Reynolds stresses ($\widetilde{v_i'' v_j''}$)**
  A new term $-\overline{\rho}\widetilde{v_i'' v_j''}$ appears in the right side of the Favre-averaged momentum conservation equation 3.6 which is called the *Reynolds stress tensor*. The tensor is symmetric (for example $\widetilde{v_1'' v_2''} = \widetilde{v_2'' v_1''}$). It represents correlations between fluctuating velocities. It is an additional stress term due to turbulence (fluctuating velocities) and it is unknown. We need a model for $\widetilde{v_i'' v_j''}$ to close the equation system. This is called the *closure problem* where the number of unknowns is larger than the number of equations.

- **Species ($\widetilde{v_i'' Y_k''}$) and enthalpy ($\widetilde{v_i'' h''}$) turbulent fluxes.**
  These fluxes are generally closed using a classical gradient assumption:

$$\overline{\rho}\widetilde{v_i'' Y_k''} = -\frac{\mu_t}{Sc_{kt}} \frac{\partial \widetilde{Y}_k}{\partial x_i} \tag{3.15}$$

$$\overline{\rho}\widetilde{v_i'' h''} = -\frac{\mu_t}{Pr_t} \frac{\partial \widetilde{h}}{\partial x_i} \tag{3.16}$$

  Where is Sc_{kt} is the turbulent Schmidt number for species k, defined as the ratio of the turbulent kinematic viscosity to the molecular diffusivity as follows:

$$Sc_{kt} = \frac{\mu_t}{\overline{\rho}\overline{D_k}} \tag{3.17}$$

  The turbulent Prandtl number compares momentum and heat transport:

$$Pr_t = \frac{\nu_t C_p}{\overline{\lambda}} \tag{3.18}$$

  The turbulent dynamic viscosity μ_t is estimated from the closure rules of the turbulence model.

- **Species chemical reaction rates ($\widetilde{\dot{\omega}_k}$)**
  The modelling of the species chemical reaction rates is the main objective of many combustion models and will be discussed later in this chapter.

3.3.4 Boussinesq's hypothesis

The Reynolds stress tensor is symmetric and can be expressed as the sum of an isotropic and a deviatoric anisotropic component. The isotropic stress is $-\frac{2}{3}\rho k$, so the Reynolds stress tensor can be written as:

$$-\overline{\rho}\widetilde{v_i''v_j''} = \mu_t(\frac{\partial\widetilde{v}_i}{\partial x_j} + \frac{\partial\widetilde{v}_j}{\partial x_i}) - \frac{2}{3}\overline{\rho}k\delta_{ij} \tag{3.19}$$

where $k = \frac{1}{2}\widetilde{\boldsymbol{v''v''}}$ is the turbulent kinetic energy. Equation 3.19 is based on the presumption that there exists an analogy between the action of viscous stresses and Reynolds stresses on the mean flow. It is important to note that the turbulent viscosity μ_t is not a fluid property, but varies within the flow. In order to close the system of equations, only a solution for the turbulent viscosity is required. A one closure equation model was presented by Prandtl (1925) known as Prandtl's mixing length model which is inaccurate where the transport of turbulence is significant. Thus, more advanced models where the conservation equations for one or more turbulent variables have been developed. Examples of such models are presented in the following sections.

3.3.5 The standard $k-\epsilon$ model

The most famous and widely used in industrial applications and well validated through the years is the standard $k-\epsilon$ model developed by Launder and Spalding in 1974 [34]. The model has two equations one for k and one for ϵ which are used to describe the velocity scale v_T and the length scale l_T as follows:

$$v_T = k^{1/2} \tag{3.20}$$

$$l_T = \frac{k^{3/2}}{\epsilon} \tag{3.21}$$

And through dimensional analysis, the turbulent viscosity μ_t is given by:

$$\mu_t = \rho C_\mu \frac{k^2}{\epsilon} \tag{3.22}$$

Where C_μ is a dimensionless constant.

The standard $k-\epsilon$ model uses the following transport equations:

$$\frac{\partial\overline{\rho}k}{\partial t} + \nabla\cdot(\overline{\rho}k\widetilde{\boldsymbol{v}}) \quad = \quad \nabla[(\mu + \frac{\mu_t}{\sigma_k})\nabla k] + P_k - \overline{\rho}\epsilon \tag{3.23}$$

$$\frac{\partial \overline{\rho}\epsilon}{\partial t} + \nabla \cdot (\overline{\rho}\epsilon\widetilde{\boldsymbol{v}}) \quad = \quad \nabla[(\mu + \frac{\mu_t}{\sigma_\epsilon})\nabla\epsilon] + C_{\epsilon 1}\frac{\epsilon}{k}P_k - C_{\epsilon 2}\overline{\rho}\frac{\epsilon^2}{k} \tag{3.24}$$

Rate of change of k or ϵ + Transport Rate of of k or ϵ by convection = Transport Rate of of k or ϵ by diffusion + Rate of production of k or ϵ - Rate of destruction of k or ϵ.

The source term P_k is given by:

$$P_k = -\overline{\rho}\widetilde{v_i'' v_j''}\frac{\partial \widetilde{v_i}}{\partial x_i} \tag{3.25}$$

Where the Reynolds stresses $-\overline{\rho}\widetilde{v_i'' v_j''}$ are determined from the Boussinesq's hypothesis (3.19).

The standard $k-\epsilon$ model constants are chosen by considering comprehensive data fitting for a wide range of turbulent flows as shown in Table 3.2.

It is noted that the ϵ equation is problematic in near-wall regions, since the term $\frac{\epsilon^2}{k}$ is singular at the wall, therefore a special treatment is required and wall functions must be considered.

C_μ	σ_k	σ_ϵ	$C_{\epsilon 1}$	$C_{\epsilon 2}$
0.09	1.00	1.30	1.44	1.92

Table 3.1: Semi-empirical constants for the $k-\epsilon$ model

3.3.6 The $k-\omega$ SST model

The $k-\omega$ shear-stress transport (SST) model is a two-equation turbulent-viscosity turbulence model developed by Menter (1994) [35]. It blends between the $k-\epsilon$ model (Launder and Spalding [34], 1974) and the $k-\omega$ model (Wilcox [36], 1988) based on the distance from the wall. The motivation behind this model is due the reason that the $k-\epsilon$ model near-wall performance is unsatisfactory for boundary layers with adverse pressure gradients. Therefore Mentor suggested this hybrid model which applies the $k-\epsilon$ model in the fully turbulent region far from the wall and switches to the $k-\omega$ SST model in near-wall regions. This model was described in details by Mentor in this article [35]. The two transport equations are given by:

$$\frac{\partial \rho k}{\partial t} + \nabla \cdot (\rho k\boldsymbol{v}) \quad = \quad \nabla[(\mu + \frac{\mu_t}{\sigma_k})\nabla k] + P_k - \beta^*\rho k\omega \tag{3.26}$$

Where $P_k = 2\mu_t S_{ij} S_{ij} - \frac{2}{3}\rho k \frac{\partial \bar{v}_i}{\partial x_j}\delta_{ij}$ is the rate of production of turbulent kinetic energy,S_{ij} is the rate of deformation , and a second transport equation of the turbulence frequency $\omega = \epsilon/k$:

$$\frac{\partial \rho\omega}{\partial t} + \nabla \cdot (\rho\omega \boldsymbol{v}) = \nabla[(\mu + \frac{\mu_t}{\sigma_\omega})\nabla\omega] + \gamma_2(2\mu_t S_{ij} S_{ij} - \frac{2}{3}\rho\omega\frac{\partial \bar{v}_i}{\partial x_j}\delta_{ij})$$

$$- \beta_2 \rho\omega^2 + 2(1 - F_1)\frac{1}{\sigma_{\omega 2}\omega}\nabla k : \nabla\omega \tag{3.27}$$

The last term in eq 3.27 is called the cross-diffusion term and it is modified by the blending function F_1 described by Mentor [35]. And some limiters are introduced for the eddy viscosity to give an improved performance for flows with adverse pressure gradients and wake regions, and the turbulent kinetic energy production is limited to prevent the build-up of turbulence in stagnation regions. The reader is referred to this reference for further details [37].

σ_k	$\sigma_{\omega 1}$	$\sigma_{\omega 2}$	γ_2	β_2	β_2^*
1.00	2.00	1.17	0.44	0.083	0.09

Table 3.2: Semi-empirical constants for the $k - \omega SST$ model

3.3.7 Near-wall treatment

Numerous experiments in the literature have shown that the mean velocity U in constant-property turbulent flow near a smooth impermeable solid surface of negligible curvature can be correlated to the wall shear stress τ_w, the normal-distance from the wall y and the fluid properties (density and molecular viscosity).

The law of the wall assumes that the turbulence close to the boundary is a function of the flow conditions close to the wall, not the flow conditions far away [38]. Defining the friction velocity $u_\tau = \sqrt{\tau_w/\rho}$ yields dimensionless length $y+ = \frac{y u_\tau}{\nu}$ and velocity $u+ = \frac{U}{u_\tau}$ which characterize the near wall regions into three distinct layers as shown in figure 3.2.

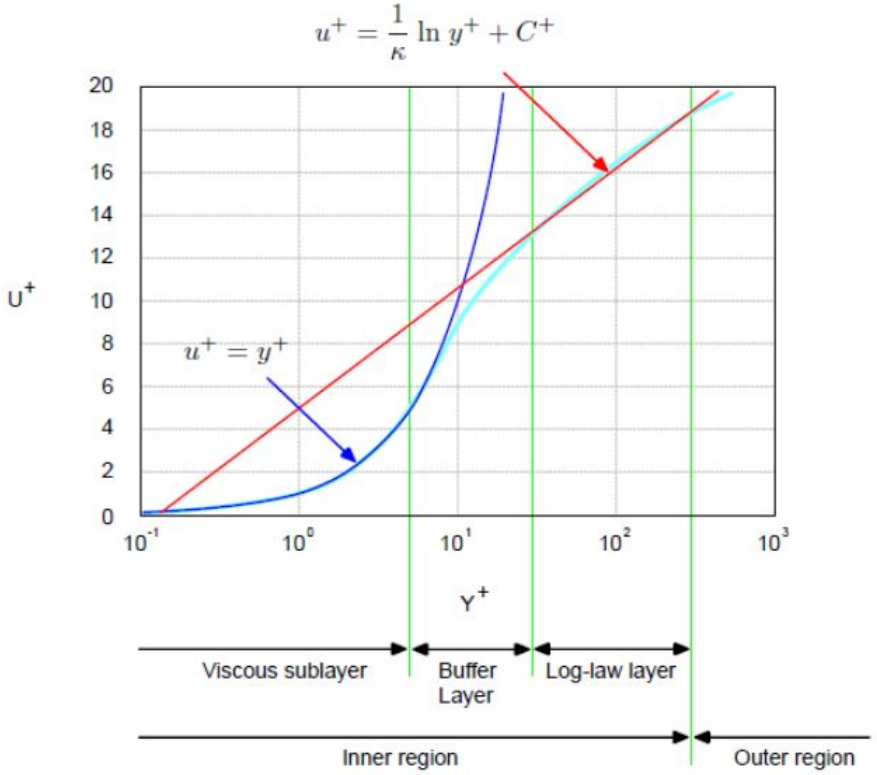

Figure 3.2: Law of the wall with different regions near the wall [39].

Low-Re turbulence models resolve every transport equation up to the viscous sub-layer at the wall, thus such models require that the first computational cell to have its centroid at a $y+ < 1$. In contrast, high-Re turbulence models apply a wall function that describes the universal velocity behavior near the wall, hence, the centroid of the first cell near the wall should lay on the log-law layer with a $30 < y+ < 300$ for good fidelity of numerical solutions. The wall-function approach is commonly used because it is economical, robust, and can be reasonably accurate. Moreover, it does not require the use of fine mesh to capture the viscous sublayer where solution variables change most rapidly, thus this approach substantially saves computational resources. However, this wall function approach should be applied only where the assumption of the law of the wall is valid; thus in other situations, viscosity-affected regions are required to be fully resolved and accordingly integrable all the way to the wall.

3.4 Combustion modelling

As the case for the Reynolds stress tensor or the turbulent diffusive and conductive fluxes, the mean chemical reaction rate ($\widetilde{\dot{\omega}_k}$) term originating from the averaging of the transport equation of species must be modeled. The closure of this term is a rather intricate and complex operation that requires a great attention. The main difficulties are associated with the strong non-linearity of this term with respect to temperature and composition. Therefore, in most situations, estimating the mean chemical reaction rate by the reaction rate based on mean quantities leads to unacceptable errors (usually orders of magnitude) especially in regions of the space where temperature fluctuations are significant. Fluctuations of these quantities (mainly temperature and compositions) must be taken into account. RANS approach is not capable of calculating such fluctuations, thus an appropriate model of these fluctuations based on the mean flow transported quantities taking into account the turbulent mixing as well is required. Unfortunately, until today, it has not been possible to formulate a complete closure model that is valid for a wide range of conditions. Among the many models proposed in the last century, none of them is capable of solving the closure problem for various combustion regimes. Each of these models is often based on very restrictive assumptions. Therefore, users in the simulation of reactive turbulent systems are opt to choose, among the many available models, the most suitable one for the problem to be investigated.

Different combustion models and approaches to simulate turbulence-chemistry interaction have been developed (the Arrhenius approach, the Eddy Break Up (EBU) model, models based on the flamelet assumptions, transported PDF, ...) [40], in this work the models which rely on the flamelet assumptions will be used.

3.4.1 The Weller combustion model

The Weller or Flame Area Evolution (FAE) model is based on the laminar flamelet concept. This concept considers the turbulent flame as an aggregate of thin, laminar ($Re < 2000$), locally one-dimensional flamelet structures embodied within the turbulent flow field. Counterflow diffusion flame is a common laminar flame that is used to represent a flamelet in a turbulent flow. The Weller model was explained in previous studies [28, 30], a brief presentation of the model will be introduced.

3.4.1.1 The one-equation Weller model

The Weller model considers the local wrinkled flame area with a differential evolution equation. This equation considers the area influenced not only by turbulent motion, but also by the flame itself and by non-local effects.

This model solves a transport equation for a local ensemble-average combustion regress variable b, while the reaction rate depends on an algebraic expression of the flame wrinkling factor Ξ. The latter is defined as the ratio between the turbulent flame speed and the unstrained laminar one S_t/S_u and it is related to the flame surface area per unit volume Σ by:

$$\Sigma = \Xi|\nabla\widetilde{b}| \tag{3.28}$$

The regress variable b represents the unburned gas fraction in any computational cell, and its transport equation is derived by conditionally averaging the continuity equation on the unburned gas state:

$$\frac{\partial\rho\widetilde{b}}{\partial t} + \nabla\cdot(\rho\widetilde{\boldsymbol{v}}\widetilde{b}) - \nabla\cdot(\mu_t\nabla\widetilde{b}) \quad = \quad \rho_u\widetilde{S}_u\widetilde{\Xi}|\nabla\widetilde{b}| + \widetilde{\dot{\omega}_{ign}} \tag{3.29}$$

Where S_u is the laminar unstrained flame speed, ρ and ρ_u are the mixture and unburned mixture density, respectively. The turbulent dynamic viscosity μ_t is estimated from the closure rules of the turbulence model. The term $\rho_u\widetilde{S}_u\widetilde{\Xi}|\nabla\widetilde{b}|$ is the reaction rate due to turbulent flame propagation while $\widetilde{\dot{\omega}_{ign}}$ represents the ignition source term. Before the ignition event, the regress variable b is uniformly equal to 1 in each computational cell in the domain representing an unburned gas fraction of 100%. Equation 3.29 can be solved fully implicitly by exploiting differential operator properties. This ensures a stable solution for the flame propagation process even in the presence of complex meshes and long time-steps.

Ignition model

The objective of this model is to initialize the distribution of the regress variable to start the flame propagation process from the flame kernel. A simplified ignition model was implemented in this study [41]. The duration of ignition Δt_{ign} and the initial flame kernel diameter d_{ign} is specified by the user; in cells whose distance from where ignition takes place is less than $r_{ign} = d_{ign}/2$, an ignition source term is imposed:

$$\dot{\omega}_{ign} = \frac{C_s\rho_u b}{\Delta t_{ign}} \tag{3.30}$$

Where C_s is a user-defined ignition strength coefficient, Δt_{ign} is the user-specified duration of the ignition event. This allows the regress variable b to be initialized in a small volume going smoothly to zero around the ignition site. Furthermore, due to the implicit formulation, it does not produce any un-physical effect in those cells where combustion is completed (b = 0).

Turbulent combustion model

The description of the turbulent premixed flames is achieved through the use of the regress variable distribution produced by the ignition model. Nevertheless, a proper expression for the flame wrinkling factor Ξ, which allows the flame front evolution from its initial laminar features to a fully developed turbulent flame, is needed. Weller [28] stated that Ξ distribution depends on its equilibrium value $\Xi^* = f(\Xi^*_{eq})$ and the regress variable b as follows:

$$\Xi = 1 + [1 + 2S_{\Xi}(0.5 - b)](\Xi^* - 1) \tag{3.31}$$

The dependency on Ξ^*_{eq} is due to the fact that laminar to turbulent flame transition is completed when Ξ reaches the value resulting from the equilibrium between production and merging (destruction) of reaction layer corrugations. This last condition is called *equilibrium* and it is characterized by the maximum wrinkling factor value, corresponding to Ξ^*_{eq}. On the other hand, the turbulence distribution across the flame is related to the dependency on b that is calibrated with the user-defined parameter S_{Ξ}. To properly discribe the transition from laminar to turbulent flame, the presence of $\Xi^* = f(\Xi^*_{eq})$ in equation 3.31 is necessary and it is expressed as:

$$\Xi^* = S_t/S_u = I_0 + I_0^{1/2} f(\Xi^*_{eq} - 1) \tag{3.32}$$

where I_0 is the flame stretch coefficient, and the parameter $0 \leq f \leq 1$ is used to model the flame evolution from laminar (f=0) to fully turbulent (f=1). Using the Herweg and Maly formulation [42], f is expressed as:

$$f = \left[1 - exp\left(-\frac{r_k}{\langle L_t \rangle}\right)\right]^{0.5} \left[1 - exp\left(-\frac{\langle v' \rangle + \langle S_u \rangle}{\langle L_t \rangle} t_{ign}\right)\right]^{0.5} \tag{3.33}$$

Where t_{ign} is the time elapsed since the ignition event, while L_t and v' are the turbulence intensity and integral length scale, respectively. The operation of field averaging on a spherical volume with radius of $C_{vol} r_k$ around the ignition site is denoted by $\langle . \rangle$, C_{vol} being a user-specified constant. A 0-D model is used to

describe the flame kernel radius evolution with time:

$$\frac{dr_k}{dt} = \frac{\rho_u}{\rho_b} I_{0,lam} S_u \tag{3.34}$$

Where ρ_b is the burnt mixture density and $I_{0,lam}$ is the laminar flame stretch parameter. The latter parameter can be expressed as:

$$I_{0,lam} = \left(1.0 - \frac{\mathcal{L}_u \kappa}{S_u}\right) \tag{3.35}$$

where $\mathcal{L}_u$ is the Markstein length referred to unburned gases while κ is the flame strain rate given by:

$$\kappa = \frac{2}{r}\frac{dr}{dt} \tag{3.36}$$

assuming a spherical kernel geometry.

The start of the turbulent regime of the combustion is assumed after a certain flame radius value $r_{k,trans}$ defined as a multiple of the Taylor turbulence micro-scale λ [43]:

$$r_{k,trans} = C_{Tay}\lambda = C_{Tay}\sqrt{10\nu\frac{k}{\epsilon}} \tag{3.37}$$

being C_{Tay} a tuning parameter, ν the kinematic viscosity, k and ϵ the turbulent kinetic energy and its dissipation rate, respectively. For turbulent flames, flame kernel radius evolution is described by the the Herweg and Maly formulation [42] :

$$\frac{dr_k}{dt} = \frac{\langle\rho_u\rangle}{\langle\rho_b\rangle}\left[I_0 + I_0^{1/2} f'(\langle\Xi^*_{eq}\rangle - 1)\right]\langle S_u\rangle \tag{3.38}$$

The modelling of laminar to turbulent transition imposes some changes to equation 3.4.2 as follows:

$$f' = \left[1 - exp\left(-\frac{r_k - C_{Tay}\lambda}{\langle L_t\rangle}\right)\right]^{0.5}\left[1 - exp\left(-\frac{\langle v'\rangle + \langle S_u\rangle}{\langle L_t\rangle}t_{ign}\right)\right]^{0.5} \tag{3.39}$$

to compute coefficient f' with respect to the kernel dimension relative to Taylor micro-scale. This slight change in formulation was implemented to make the equations 3.34 and 3.37 more consistent. To ensure the continuity of both turbulence

and laminar stretch effects during flame kernel growth, I_0 is computed as:

$$I_0 = min(I_{0,lam}, I_{0,turb}) \tag{3.40}$$

The estimation of $I_{0,turb}$ is through the use of the empirical formula from Bray [29]:

$$I_{0,turb} = \frac{0.117}{1+\tau} Ka^{-0.784} \tag{3.41}$$

Where $\tau = T_u/T_b - 1$ and Ka is the Karlovitz number.

Equilibrium wrinkling factor correlations

The expression for the Ξ^*_{eq} that used in equation 3.32 and 3.38 is calculated using different correlations derived in the literature [44]. In this thesis, only three correlations will be assessed which are:

1. *Peters correlation:*

$$\Xi^*_{eq} = 1 - \frac{0.78}{2C}\frac{l_T}{\delta_{th}} + \left[\left(\frac{0.78}{2C}\frac{l_T}{\delta_{th}}\right)^2 + 0.78\frac{v'}{S_u}\frac{l_T}{\delta_{th}}\right]^{0.5} \tag{3.42}$$

Where δ_{th} is the thermal flame thickness, and C=2.0 obtained by interpolation of many experimental data.

2. *Gulder correlation [45]:*

$$\Xi^*_{eq} = 1 + \Xi_{coef}\sqrt{\frac{v'}{S_u}}\mathcal{R}_\eta \tag{3.43}$$

where Ξ_{coef} is equal to 0.62, obtained with interpolation of many sets of experimental data in [45]. R_η is the Kolmogorov Reynolds number, defined as:

$$R_\eta = \frac{v'}{\epsilon\tau_\eta} \tag{3.44}$$

$$\tau_\eta = \sqrt{\frac{\mu_u}{\rho\epsilon}} \tag{3.45}$$

In which τ_η is the Kolmogorov time scale and μ_u the dynamic viscosity of unburned mixture.

3. Muppala correlation:

$$\Xi^*_{eq} = 1 + \frac{C}{Le} Re_T^{0.25} (\frac{v'}{S_u})^{0.3} (\frac{P}{0.1MPa})^{0.2} \tag{3.46}$$

Where Le is the Lewis number and P is the pressure, where C=0.46 obtained by interpolation of many experimental data.

3.4.1.2 The two-equations Weller model

Differently from the one-equation Weller model, the flame wrinkling factor can be calculated based on a transport equation instead of an algebraic description. This gives a more detailed description of local parameters of the flow field. The transport equation for the flame wrinkling factor can be written as:

$$\frac{\partial \Xi}{\partial t} + \hat{U} \nabla \Xi = G\Xi - R(\Xi - 1) + max(\sigma_t - \sigma_s, 0)\Xi \tag{3.47}$$

Where σ_t and σ_s are the strain rate relative to the mean flux and the one relative to the local distribution of the flame surface, respectively. $\hat{U}$ is the average of the instantaneous velocities of the flame surface. The Ξ transport equation is used to compute the local relationship between the flame surface wrinkling generation and annihilation. G and R are suitable coefficients which in this formulation were modeled following the flame-speed correlation of Gulder

$$G = R \frac{\Xi_{eq} - 1}{\Xi_{eq}} \tag{3.48}$$

$$R = \frac{0.28}{\tau_\eta} \frac{\Xi^*_{eq} - 1}{\Xi^*_{eq}} \tag{3.49}$$

Where τ_η is the Kolmogorov time scale. It can be noted that the two-equation model could be reduced to the one-equation model, considering a local equilibrium between the flame surface wrinkling generation and annihilation, so that $\Xi_{eq} = \Xi$ and obtaining the main reaction rate as in equation 3.29.

3.4.2 The Coherent Flamelet Model (CFM)

The CFM model is also based on the flamelet concept. The CFM describes the turbulent flame as an aggregate of flamelet elements embedded in a turbulent flow. It is applicable to both premixed and non-premixed flames [29]. Its feature lies in the decoupled treatment of the turbulent flow and chemical reaction. In fact, this model is based on the assumption that the flame can be seen as an infinitely thin layer separating fresh and product gases where the chemical reaction of fuel oxidation occurs. Unlike the Weller model, the propagation of the flame front is described through a progress variable c, representing the burned mass fraction, and a flame surface density Σ defined in each cell of the domain as the ratio between the local flame surface to the cell volume. A high flame surface density at a given location in the flow field corresponds to a high turbulent reaction rate. The flame surface density Σ is computed through a model transport equation after being initialized through a suitable ignition model. The advantage of this approach is to separate chemistry effects incorporated into the average flame speed $\widetilde{S}_u$ from the turbulence-chemistry interaction incorporated into the flame surface density Σ. The transport equation for Σ is expressed as:

$$\frac{\partial \rho\widetilde{\Sigma}}{\partial t} + \nabla \cdot (\rho\widetilde{\boldsymbol{v}}\widetilde{\Sigma}) - \nabla \cdot \left(\mu_t \nabla \left[\frac{(\rho\Sigma)}{\rho} \right] \right) + (\nabla \cdot \widetilde{\boldsymbol{v}})\rho\Sigma = S\rho\Sigma - D\rho\Sigma \tag{3.50}$$

Where S and D are the production and annihilation source terms of the flame surface density, respectively. The formulation of those source terms is linked to the laminar-turbulent transition, to properly simulate the interaction between the turbulence field and the flame front propagation. After the initialization and the evolution of the flame surface density , a transport equation for the progress variable c of the reaction (c = 0 in fresh gases and c = 1 in fully burnt gases) is solved to describe the reacting flow according to:

$$\frac{\partial \rho\widetilde{c}}{\partial t} + \nabla \cdot (\rho\widetilde{\boldsymbol{v}}\widetilde{c}) - \nabla \cdot (\mu_t \nabla\widetilde{c}) = \rho_u I_0 \widetilde{S}_u \Sigma \tag{3.51}$$

The reaction rate expressed as $\rho_u I_0 \widetilde{S}_u \Sigma$ is solved explicitly, unlike the Weller model where the regress variable b is treated fully implicitly. Another difference between the two models is that the flame stretch in the CFM model should be included in equation 3.51, while in the Weller model this effect is already included in the flame wrinkling factor Ξ expression [45].

Ignition model

The initialization of flame surface density is done starting from the concept that at the ignition site the mixture fraction is to be consumed propagating towards the surrounding areas. Based on the assumption that the ignition event is of a spherical geometry, at the sphere center cell is initialized as follows:

$$\Sigma_k = \frac{S_{kernel}}{V_{cell}} \tag{3.52}$$

Where k is the ignition cell position, $S_{kernel} = 4\pi r_{ign}^2$ is the imposed flame kernel surface area, and V_{cell} being the cell volume. The user is opt to tune the duration of ignition Δt_{ign} to generate a constant source term, the flame kernel diameter d_{ign}, and the ignition site.

Turbulent combustion model

The implemented two-equation CFM model described by equations 3.50 and 3.51 is capable of describing the flame front evolution from laminar to turbulent regimes. The source terms are selected following the Choi-Huh approach [29] and keeping a consistency with the Weller model as well. Two sets of production and annihilation terms are listed:

$$\text{1. Laminar stage} \begin{cases} S_{lam} = 2\rho_u/\rho_b \, (I_0 S_u)/r_k \\ D_{lam} = 0 \end{cases} \tag{3.53}$$

$$\text{2. Turbulent stage} \begin{cases} S_{turb} = u'/l_{tc} \\ D_{turb} = (I_0 S_u \Sigma)/[c(1-c)] \end{cases} \tag{3.54}$$

Being r_k is as computed previously in the Weller model using the $0-D$ model, and l_{tc} is a length scale introduced for dimensional reasons according to [29]. The Herweg and Maly approach in equation was implemented to describe the laminar-turbulent flame transition by averaging equations 3.53 and 3.54 as follows:

$$\bullet \text{ Laminar-turbulent flame transition} \begin{cases} S = \alpha[(1-f)S_{lam} + fS_{turb}] \\ D = \beta[(1-f)D_{lam} + fD_{turb}] \end{cases} \tag{3.55}$$

Where α and β are model constants that need a proper tuning.

3.4.3 Laminar flame speed correlation

The unstrained laminar flame speed S_u is estimated according to:

$$S_u = S_{u,ref}(\phi) \cdot (\frac{T}{T_{ref}})^{\alpha} \cdot (\frac{P}{P_{ref}})^{\beta} \tag{3.56}$$

Where $S_{u,ref}$ depends on equivalence ratio and is computed at reference conditions. $S_{u,ref}$ is calculated according to Gulder's correlation [46]:

$$S_{u,ref} = W \cdot \phi^{\eta} \cdot e^{-\xi(\phi-1.075)^2} \tag{3.57}$$

Where $W, \eta, \xi, \alpha, \beta$ are provided in [46] for Methene, Propane and Isooctane fuels.

3.4.4 Tabulated kinetics

The combination of the mass fraction of chemical species of the burned $Y_{b,i}$ and unburned $Y_{b,i}$ state balanced with the regress variable b can be used to determine the chemical composition in any computational cell as follows:

$$Y_i = b \cdot Y_{u,i} + (1-b) \cdot Y_{b,i} \tag{3.58}$$

The burned gas chemical composition $Y_{b,i}$ is computed from a lookup table and the detailed scheme is described in [47]. Reaction rates and chemical composition are stored in a lookup table, which is generated by processing results of constant-pressure homogeneous reactor calculations. These computations were performed at different values of equivalence ratio, pressure, and unburned gas temperature, using the GRI 3.0 mechanism with 53 species and 325 reactions. In this thesis, only chemical composition at equilibrium conditions is retrieved while the reaction rate from premixed combustion comes from equations 3.29 or 3.51, depending on the implemented combustion model.

In order to correctly access the lookup table, a transport equation is solved for the unburned gas enthalpy h_u, which provides the fresh mixture temperature T_u. The burned gas enthalpy h_b is estimated from h_u and the mean cell value:

$$h_b = \frac{h - b \cdot h_u}{1-b} \tag{3.59}$$

Consequently, the burned gas temperature T_b is computed from h_b and composition $Y_{b,i}$. It is worth mentioning that the chemistry table used in this study was observed to have a slight amount of exhaust gas recirculations (EGR) that will be

corrected in future work; however, the main focus, for now, is to understand the capabilities of the implemented combustion models.

Chapter 4

Numerical Setup

In this Chapter, an explanation of the numerical setup of the TSF burner along with the mesh generation and numerical schemes is presented.

4.1 OpenFOAM and LibICE

4.1.1 OpenFOAM

OpenFOAM, that stands for "Open source Field Operation and Manipulation" is the leading open-source software for computational fluid dynamics, written in C++. The software was first developed at the Imperial College London by Henry Weller in the early 1990s in Prof. David Gosman's group. OpenFOAM now has a large user base across most areas of engineering and science, from both commercial and academic organizations. An overview of the software structure is shown in Figure 4.1.

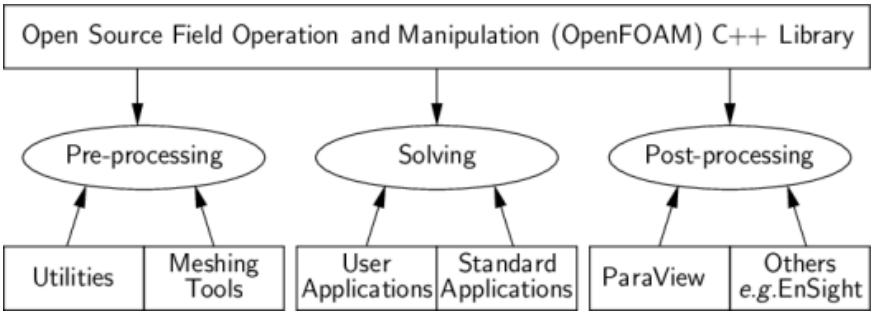

Figure 4.1: Overview of OpenFOAM structure.

The basic directory structure for an OpenFOAM case, that contains the minimum set of files required to run an application, is shown in Figure 4.2 and the three basic folders are described as follows:

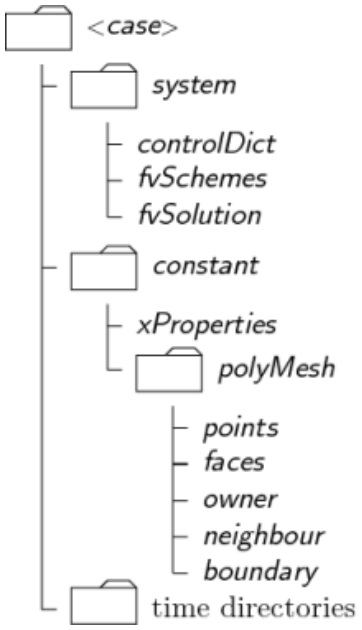

Figure 4.2: Case directory structure.

- **A 'system' directory:** This folder is for managing the solution procedure itself. It should contain at least 3 files: the `controlDict` file which gives the run control parameters such as the start and end time, the time step, the options for data output parameters; the `fvSchemes` file which is for specifying the discretization schemes of the governing equations; the `fvSolution` file which controls the equation solvers, tolerances and convergence criteria.
- **A 'constant' directory:** that contains a full description of the case mesh in a subdirectory `polyMesh`. Other files specifying physical properties for the application concerned, such as transportProperties, chemistryProperties, chemistryTableProperties, combustionProperties, etc.
- **The 'time' directories:** This folder contains individual files of data for all the fields involved in the calculations. The "0" folder contains all the initial and boundary conditions for the considered case.

4.1.2 LibICE

The ICE group of Politecnico di Milano has developed a set of libraries, solvers, and utilities grouped under Lib-ICE in-house code: it is a code based on OpenFOAM environment focused on internal combustion engines simulations. This code provides a modified version of the base OpenFOAM solvers and utilities for mesh management, combustion, direct-injection strategies, and other typical engine applications.

4.2 Computational domain

A 2-D axisymmetric analysis of the Darmstadt TSF burner is considered because of the symmetrical feature of the geometry of the burner that is made up of concentric tubes as shown previously in Figure 2.2. The computational domain of the burner consists of a wedge of 5 degrees, as depicted in Figure 4.3. Thanks to the `'wedge'` boundary condition, the flow effects on the third dimension (z-axis) are also considered.

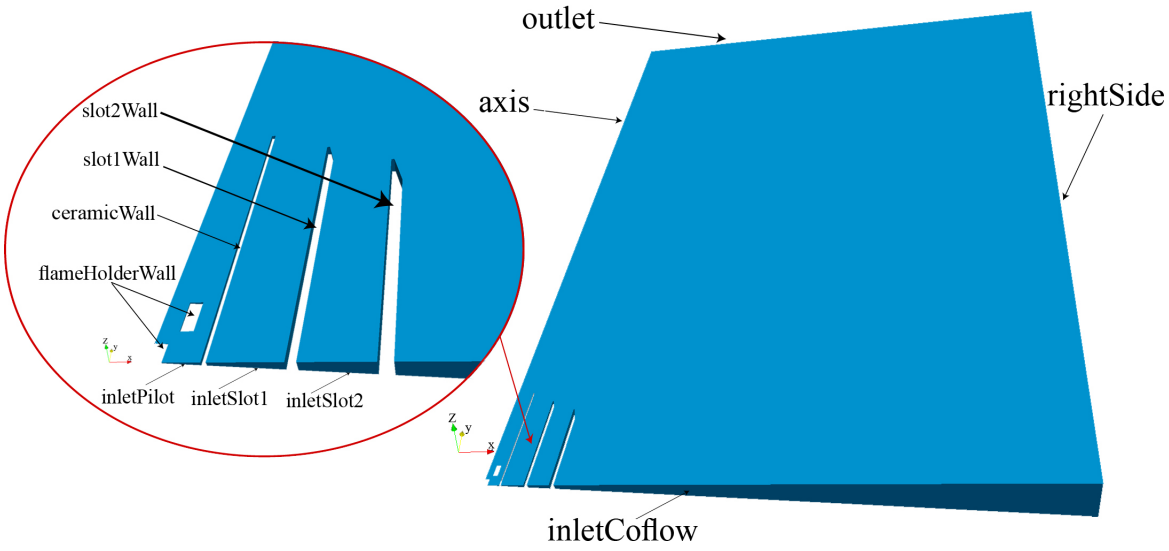

Figure 4.3: 2-D axisymmetric wedge domain for the Darmstadt TSF burner.

The computational domain has been drawn according to the measures given by the Technical University of Darmstadt [31]. In order to simulate the effect of the flame holder, the computational domain contains the geometrical details of the axial extensions of the burner pipes of 50 mm upstream the burner exit, as shown in Figure 4.4. To obtain fully turbulent profiles of the flow streams at the tube inlets, separate simulations of turbulent pipe flow with streamwise periodic conditions are performed. According to [31], the experimental measurements were obtained until 200 mm downstream of the burner exit. As a result, 300 mm downstream of the burner exit is included in the computational domain ensuring that the numerical simulations can cover all the experimental measurement sections. In the radial direction, the domain ranges from the axis of symmetry (0 mm) to the end boundary (`rightSide`) of the co-flow (250 mm). The jet injection direction is defined as y coordinate, whereas the radial direction is defined as x (or r). The pilot exit position is defined as y=0 mm and the axis of symmetry is defined as x (or r) = 0 mm, as depicted in Figure 4.4. Thus, the overall domain ranges from [-50 , 300] mm in the y-direction and [0 , 250] mm in the x-(or r-)direction.

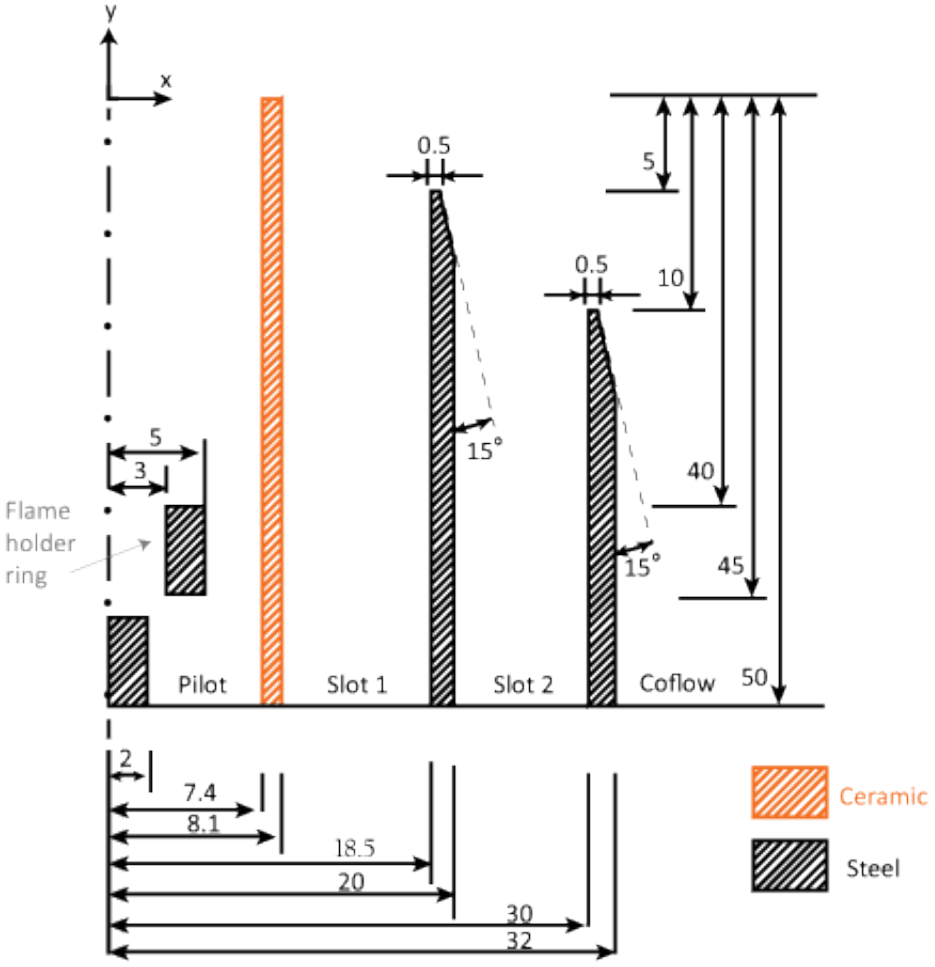

Figure 4.4: 2-D axisymmetric cut with dimensions in mm (not to scale) and geometrical details of the TSF burner pipes showing the axial extensions of their final part, wall thicknesses and exit rims.

Table 4.1 illustrates the type of patches that are used to describe the computational domain of the TSF burner as shown in Figure 4.3. The specification of the boundary conditions will depend on the used turbulence or combustion model and will be tabulated accordingly in the next chapter.

Patch name	Type
inletPilot	Patch
inletSlot1	Patch
inletSlot2	Patch
inletCoflow	Patch
rightSide	Patch
outlet	Patch
ceramicWall	Wall
slot1Wall	Wall
slot2Wall	Wall
flameHolderWall	Wall
front	Wedge
back	Wedge
axis	Empty

Table 4.1: Patch types

4.3 Mesh generation & sensitivity analysis

The `blockMesh` utility of OpenFOAM was used for the discretization of the domain. The objective of this tool is to decompose the domain geometry into a set of one or more three-dimensional hexahedral blocks. A block is defined by 8 vertices, one at each corner of a hexahedron. The TSF burner domain is composed of 40 blocks, as indicated in Figure 4.5. The dimensions in Figure 4.5 are not to scale and actually the axial and radial extensions of the domain were not fully shown only to save space. Many blocks were introduced in the pilot section in order to include the flame holder configuration and for the purpose of constructing a structured mesh. According to this, it is possible to refine the mesh in most critical regions, like near the flame holder and in the injection jet direction, and use a coarser mesh in the faraway regions. It is obvious that far away in the radial direction (the coflow region) the mesh density should be reduced to save computational time. The cell sizes can be changed inside the block using the `simpleGrading` technique. In the coflow region, in the right far-most region, cells are bigger than those in the left using an expansion ratio of 6 along the radial direction. Also, blocks that are above the pilot exit have an expansion ratio of 2 along the jet injection direction. That means the cell size grows with the increase in distance downstream of the pilot exit. This technique is used as a compromise

of capturing the physical phenomena and saving the computational time. Since the work is a 2-D axisymmetric analysis, there is just one cell along the z-direction.

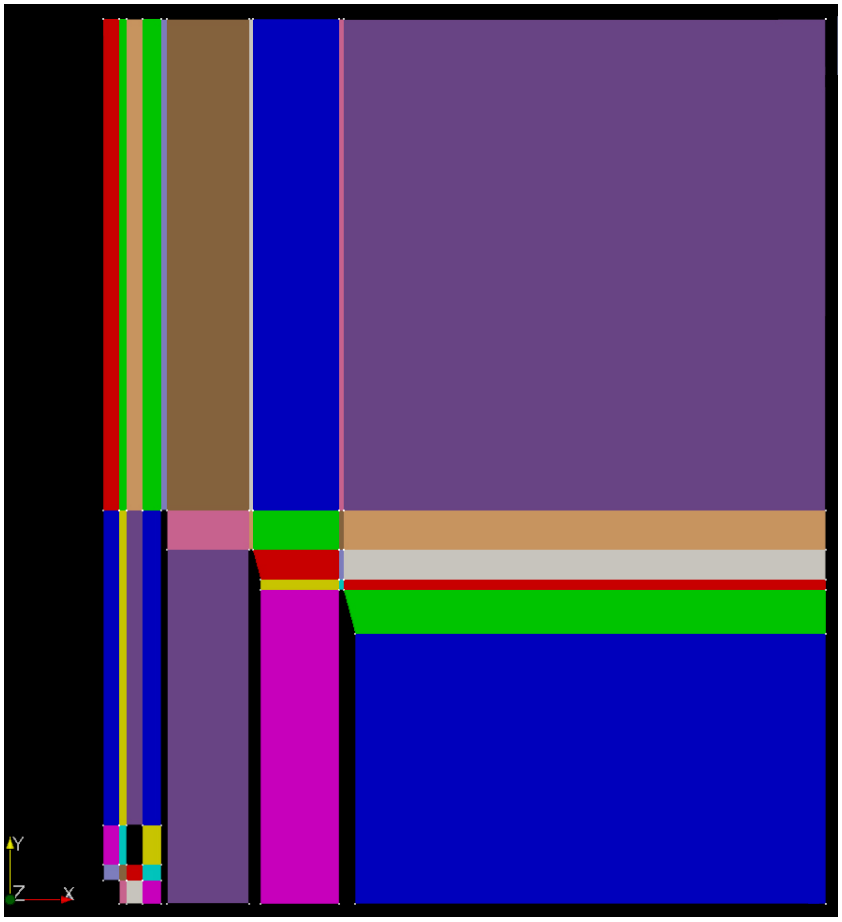

Figure 4.5: Blocks in the domain (not to scale).

A mesh sensitivity analysis only on the non-reacting case A-i2 was carried out using the $k-\omega$ SST turbulence model with the well-known SIMPLE (Semi-Implicit Method for Pressure Linked Equations) algorithm for this steady-state simulations. The final decision on the number of cells is always a compromise between the computational cost and the solution accuracy but, in any case, a mesh independent solution should be achieved where the solution does not vary significantly even when a further refinement of the mesh is introduced. For the TSF geometry shown before, a structured mesh was generated for the whole domain, i.e. each central cell in the internal field is connected by four neighboring cells, considering only a single cell in the z-direction. This is an advantage for decreasing the computational time. Moreover, structured meshes with low non-orthogonality values allow achieving robust results from a physical point of view because few cells are affected by interpolation errors between neighboring cells. However, the only drawback of adopting such kind of grids particularly for more complex geometries

is the increase in grid non-orthogonality or skewness that can cause unphysical solutions and numerical instabilities.

Different mesh resolutions were tested. At the very beginning, a coarse mesh is used to perform calculations in a reasonable time. Afterward, it is refined until mesh independence is reached. The axial velocity U_y at various sections downstream of the burner exit was used for this analysis, namely at y equal to 1, 50, and 100 mm. Figure 4.7 shows that 160,000 cells achieve convergence; however, it was decided to use 80,000 cells since it shows a satisfactory level of convergence at various distances of the burner exit. Only a slight overestimation was observed of the velocity at y = 1 mm in the shear mixing layer produced by the presence of the ceramic tube. However, the number of cells can not be too high because in the combustion analysis the number of variables is increased with respect to the non-reacting case. Thus, an 80k-cells mesh has been chosen to obtain the best tradeoff between the computational time and the precision of the results. The overall optimized mesh is illustrated in Figure 4.6.

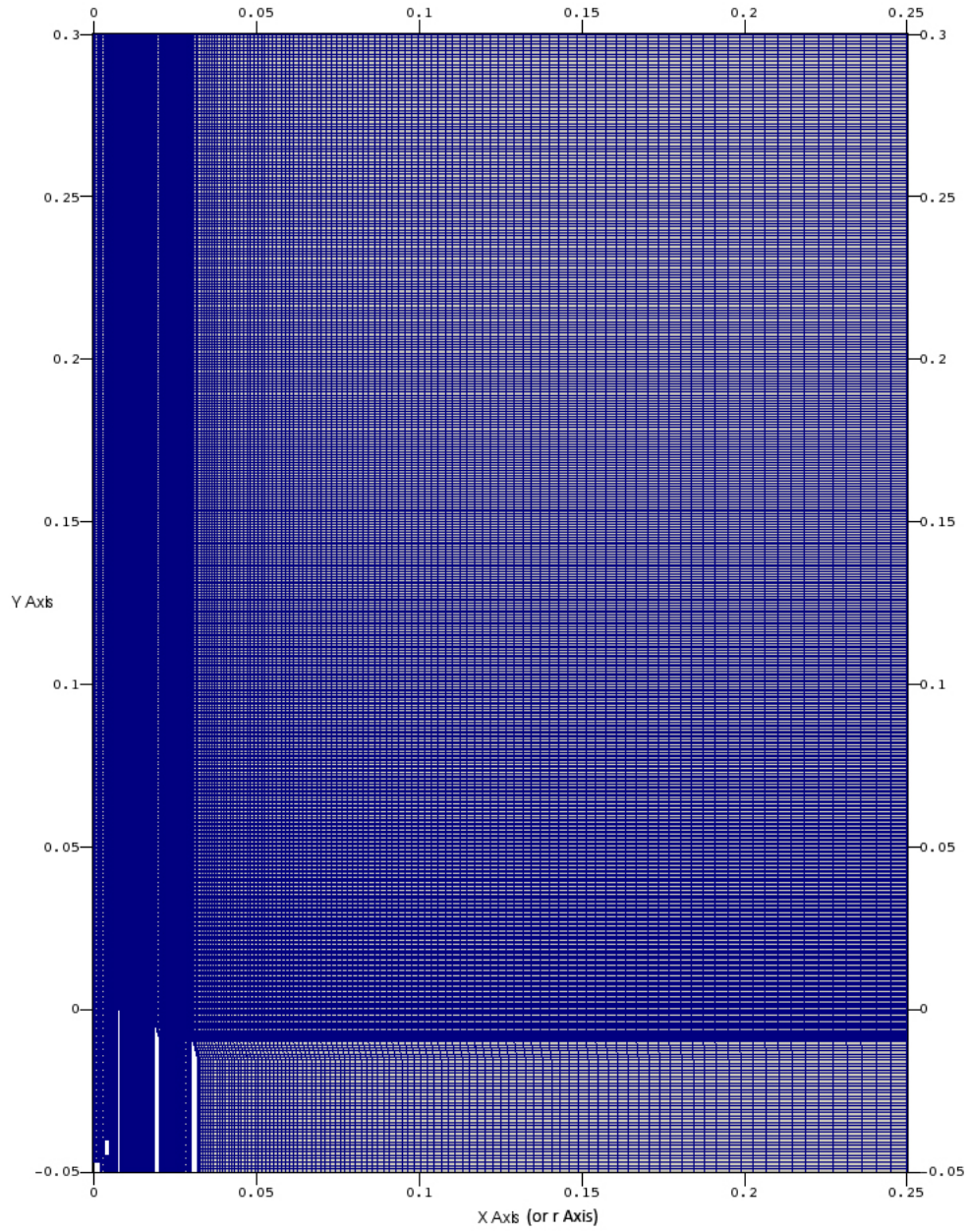

Figure 4.6: The overall optimized mesh of 80k cells (dimensions are in meters and not to scale).

It is worth mentioning that the average cell dimension in the refined regions (jet-direction and inside the burner) is in the order of 0.5 mm, while the far-away region is in the order of 1 mm.

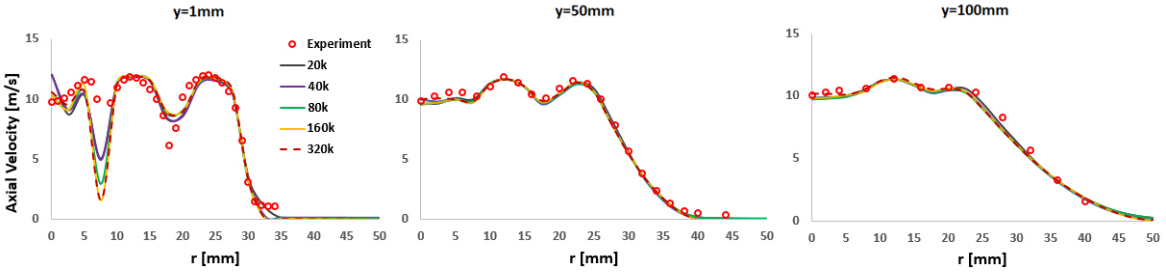

Figure 4.7: Axial velocity profiles at various axial locations y for non-reacting case A-i2 with different meshes.

The mesh details are shown in Figure 4.8 for both turbulence models: the standard $k-\epsilon$ and the $k-\omega$ SST models. The only difference between the two meshes is the near-wall treatment approach. The standard $k-\epsilon$ model is a high-Re turbulence model, meaning that the $y+$ value should not be lower than 11 (viscous sublayer) and try to avoid the buffer layer as well because the solution accuracy might degrade in an uncontrolled manner. For this reason, the first cell near the walls in the slots has been slightly enlarged to have a $y+$ value more than 20 to allow the use of the wall functions introduced previously in Chapter 3. However, it is difficult to coarsen the mesh near the flame holder with the use of structured mesh techniques because the mesh density in the wake of the flame holder should be refined enough to capture the flow field correctly. Thus, only a $y+ > 11$ was ensured in that region. On the other hand, the $k-\omega$ SST model is a low-Re model that resolves every transport equation up to the viscous sub-layer at the wall, thus it requires the first computational cell to have its centroid at a $y+ < 1$. For this reason, boundary layers were added using "refineWallLayer" in all wall patches to ensure a $y+ < 1$ in the first computational cell near any wall patch.

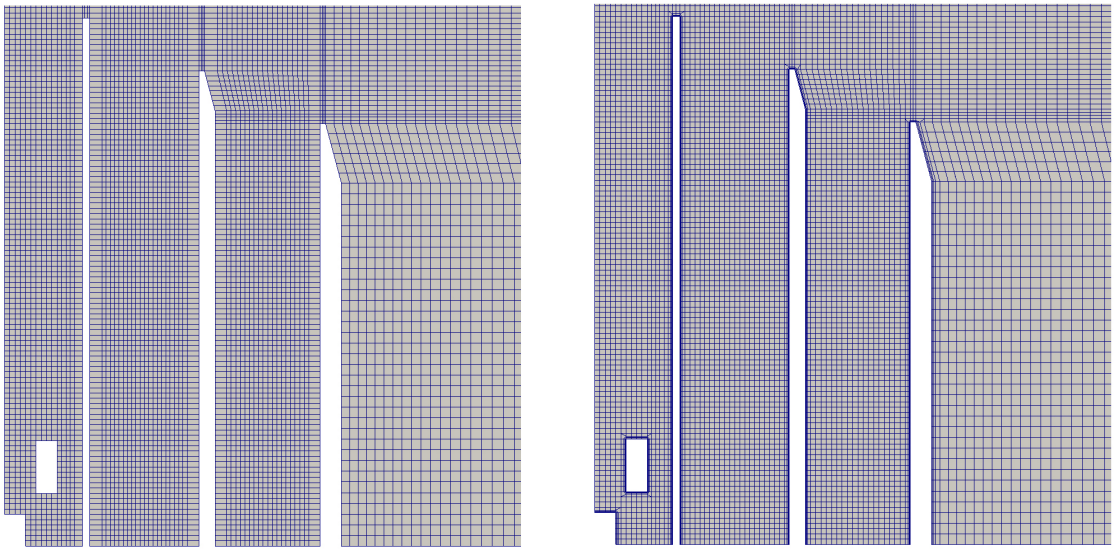

Figure 4.8: Partial mesh around the burner for the $k-\epsilon$ and the $k-\omega$ SST models.

4.3.1 Mesh quality check

Quality indicators are used to assess the mesh quality which includes:
For the $k-\epsilon$ mesh:

- **Mesh non-orthogonality, Max: 14.9 Average: 1.1 (Acceptable).**
- **Maximum aspect ratio = 4.0 (Acceptable).**
- **Maximum skewness = 0.65 (Acceptable).**

For the $k-\omega SST$ mesh:

- **Mesh non-orthogonality, Max: 46.1 Average: 1.1 (Acceptable).**
- **Maximum aspect ratio = 14.7 (Acceptable).**
- **Maximum skewness = 1.1 (Acceptable).**

The slight increase of aspect ratio in the $k-\omega$ SST mesh is due to the very fine boundary layers. High aspect ratio cells usually appear in very fine boundary layers. It is not fatal for the solver stability, but can significantly decrease convergence speed. Generally, the maximum accepted values for mesh non-orthogonality, aspect ratio, and skewness are 70°, 20, and 4, respectively. The mesh has about 80k cells in both cases and according to quality indicators, the final chosen mesh is acceptable to be applied for different numerical schemes and going further in the non-reacting and reacting simulations.

4.4 Cyclic-flow simulations for turbulence initialization

Separate cyclic-flow simulations were carried out mainly for two purposes which are:

1. To generate fully turbulent velocity profiles that are then mapped at the tubes inlets without the need of increasing the length of the computational domain to ensure this condition.

2. To estimate the minimum number of cells needed in the radial direction at each tube through a convergence analysis on the velocity profile that ensures the desired $y+$ value based on the selected turbulence model.

The method is as follows: three blocks, that are basically an extension of the inlet of the tubes with equal dimensions of the inlet and exit patches, are built using *blockMesh* utility. Only two cells in the axial direction are enough with a reasonable user-defined length of the blocks (70 mm is randomly selected in this case). The boundary condition of the inlet and outlet patches of this cyclic-flow simulations are specified for all vector and scalar fields as a cyclic boundary condition with its appropriate value. For example, the turbulent kinematic viscosity ν_t boundary condition of inlet and outlet patches of slot 1 is set as:

```
inlet
{
    type            cyclic;
    value           uniform 0;
}

outlet
{
    type            cyclic;
    value           uniform 0;
}
```

Other patches are treated normally with the usual appropriate boundary conditions. Figure 4.9 shows the fully turbulent velocity profile that will be mapped as an inlet boundary conditions at the burner inlet along with other scalar fields. All simulations were carried out using the SIMPLE algorithm.

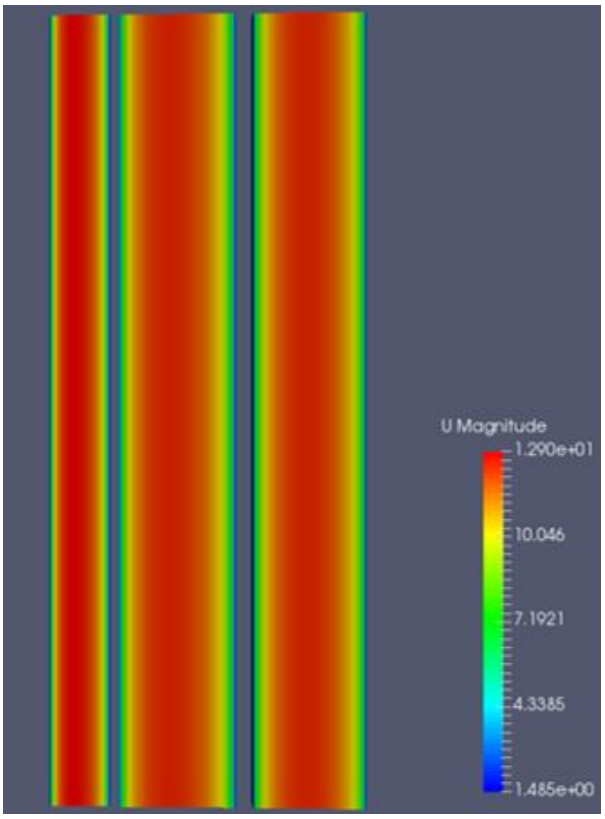

Figure 4.9: Fully turbulent velocity profiles obtained from the cyclic-flow simulations.

The second objective of such simulations is to estimate the required number of cells for achieving convergence and proper analysis of the boundary layer. Figure 4.10 shows the axial velocity profile at the pilot inlet in the cyclic simulations, the number of cells here represents only the initial number of cells in the radial direction before applying a further refinement on the last cell near both walls to ensure the desired $y+$ value. For example, an initial number of cells of 16 showed a good convergence on the velocity profile, then the $y+$ is computed and if it is more than 1 (in case of the $k-\omega$ SST model) then further refinements are applied only on the last cell of both walls and the process is repeated until a $y+$ value of less than 1 is achieved. For this purpose, the OpenFOAM utility `'refineWallLayer'` was used to refine cells next to the wall patches. This procedure was also applied for slot 1 and slot 2 using both turbulence models the standard $k-\epsilon$ and $k-\omega$ SST. In both models, it was found that starting from an initial number of cells of 16 and then managing the last cell in the boundary layer in all the tubes inlet will result in a velocity profile convergence.

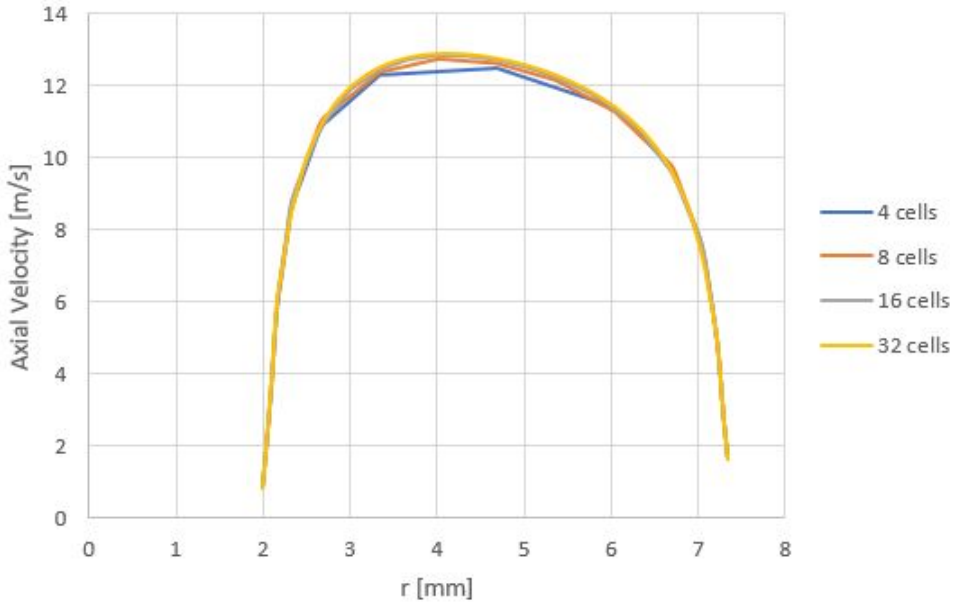

Figure 4.10: Estimation of the required number of cells in the pilot tube based on velocity convergence on the cyclic simulations.

4.5 Numerical schemes and solutions

The `fvSchemes` dictionary in the `system` folder specifies the numerical schemes for derivatives in the governing equations. This section describes the schemes that have been used in the present work after a comprehensive theoretical explanation of the various discretization schemes. An example of the `fvScheme` dictionary for numerical schemes specifications in OpenFOAM is given in Table 4.2.

Table 4.2: Example of fvSchemes dictionary in OpenFOAM.

keyword	Numrical Schemes
ddtSchemes	*default* Euler
gradSchemes	*default* Gauss linear
divSchemes	*default* none
	div(phi,U) bounded Gauss upwind
	div(phi,k) bounded Gauss upwind
	div(phi,epsilon bounded Gauss upwind
	div(phi,omega) Gauss linear
	*div((nuEff*dev2(T(grad(U)))))* Gauss linear
	div(nonlinearStress) Gauss linear
laplacianSchemes	*default* Gauss linear corrected
interpolationSchemes	*default* linear
snGradSchemes	*default* corrected

The `fvSchemes` dictionary in the `system` folder specifies the numerical schemes for derivatives in the governing equations. The terms for which numerical schemes

must be specified are divided in sub-dictionary as follows:

- timeScheme: first and second order time derivatives terms.
- gradSchemes: the gradient term.
- divSchemes: the divergence term.
- laplacianSchemes: the Laplacian term.
- interpolationSchemes: cell to face interpolations of values.
- snGradSchemes: component of gradient normal to a cell face.
- wallDist: distance to wall calculation, where required.

First the possible discretization schemes for the various terms will be presented then the selection of the suitable schemes for the non-reacting and reacting cases will be discussed.

4.5.1 Time schemes

The first time derivative $\partial/\partial t$ terms are set in the ddtSchemes sub-dictionary. The available discretization schemes in OpenFOAM are listed in Table 4.3. It is noteworthy that solvers for unsteady simulations such as *pimpleDyMFoam* are designed for transient flow calculations, simulations will not converge if *steadyState* is specified in the dictionary. However, The *steadyState* condition is suitable for steady-state solvers such as *simpleFoam*. The coefficient ψ in *CrankNicholson* Scheme can help to improve stability by means of blending it with Euler scheme. $\psi = 1$ corresponds to pure *CrankNicholson* and $\psi = 0$ corresponds to pure Euler. In such case, it is possible to make the trade-off between accuracy and stability.

1. **Euler**: first order, implicit, and bounded

$$\frac{\partial \phi}{\partial t}|_n = \frac{\phi^n - \phi^{n-1}}{\Delta t} \tag{4.1}$$

2. **CrankNicholson**: Second order, implicit and bounded.

$$\frac{1}{1+\psi}\frac{\partial \phi}{\partial t}|_n + (1 - \frac{1}{1+\psi})\frac{\partial \phi}{\partial t}|_{n-1} = \frac{\phi^n - \phi^{n-1}}{\Delta t} \tag{4.2}$$

Table 4.3: Time discretization schemes.

Scheme	Description
Euler	First order, bounded, implicit
localEuler	Local-time step, first order, bounded, implicit
CrankNicholson ψ	Second order, bounded, implicit
backWard	Second order, implicit
steadyState	Does not solve for time derivative

4.5.2 Gradient schemes

The gradient of a scalar property ϕ is defined as:

$$\nabla\phi \quad = \quad \mathbf{e_1}\frac{\partial\phi}{\partial x_1} + \mathbf{e_2}\frac{\partial\phi}{\partial x_2} + \mathbf{e_3}\frac{\partial\phi}{\partial x_3} \tag{4.3}$$

where the **e** vectors are the unit vectors in the 3-D space. The gradSchemes sub-dictionary in OpenFoam contains gradient terms. The default discretization scheme that is primarily used for gradient terms is: "default Gauss linear". Gradient schemes are specified in the gradSchemes sub-dictionary using the syntax:

```
gradSchemes
{
    default         Gauss none;
    grad(p)         <optional limiter> <gradient scheme> <interpolation scheme>;
}
```

For the gradient operator the available discretization schemes are shown in Table 4.4:

Table 4.4: Gradient discretization schemes.

Scheme	Description
Gauss <interpolation scheme>	First order, bounded, implicit
leastSquares	a second-order, least squares distance calculation using all neighbour cells
fourth	a fourth-order, least squares
cellLimited <gradScheme>	a gradient scheme applied to a selected base gradient scheme
cellMDLimited <gradScheme>	a gradient scheme applied to a selected base gradient scheme
faceLimited <gradScheme>	a gradient scheme applied to a selected base gradient scheme
faceMDLimited <gradScheme>	a gradient scheme applied to a selected base gradient scheme

The limited gradient schemes impose that the extrapolated face value is bounded by the neighbouring cell values by limiting the gradient. Cell limiting specifies the limited gradient along a line connecting adjacent cell centers while

face limiting determines the limited gradient on the face itself. The velocity gradient $grad(U)$, where its value is computed among the cells faces and centers, can be computed using different schemes. The different available schemes, used to check the power coefficient value for the gradient operator on the velocity, are the following:

- **Gauss Linear:** This is the default case where the value at the face center ϕ_f is determined by linear interpolation between the primary cell center and the neighboring cell center. Gradient calculated using integrals over faces

$$\int_V \nabla\phi \, dV = \oint_S d\mathbf{S}\phi = \sum_f \mathbf{S}\phi_f \tag{4.4}$$

  The face value of ϕ is evaluated from cell centre values:

$$\phi_f = f_x\phi_P + (1 - f_x)\phi_N \tag{4.5}$$

  Where $f_x = \overline{fN}/\overline{PN}$. It is a second-order accurate scheme.

- **Cell Limited Gauss Linear 1:** The linear interpolation may lead to unboundedness of the solution. This scheme was chosen because it improves boundedness and stability of the gradient in order to have a bounded value at the face. cellLimited scheme limits the gradient such that when cell values are extrapolated to faces using the calculated gradient, the face values do not fall outside the bounds of values in neighbouring cells.

- **Least Square:** it is a second order accuracy scheme on all type of meshes. Consider a cell centre P and a cluster of points around it N such that:

$$e_N = \phi_N - (\phi_P - \mathbf{d_N} \cdot (\nabla\phi)_P) \tag{4.6}$$

  Minimizing the weighted error:

$$e_P^2 = \sum_N w_N e_N^2; \quad where \quad w_N = \frac{1}{|\mathbf{d_N}|} \tag{4.7}$$

  yields a second-order least-square form of gradient:

$$(\nabla\phi)_P = \sum_N w_N^2 \mathbf{G^{-1}} \cdot \mathbf{d_N}(\phi_N - \phi_P) \tag{4.8}$$

Where **G** is a 3×3 matrix:

$$\mathbf{G} = \sum_N w_N^2 \mathbf{d_N} \mathbf{d_N} \tag{4.9}$$

- **Gauss Cubic:** The Gauss cubic is a third-order scheme mainly used for structured meshes not inclined with respect to the flow. Errors accumulate in the case of the unstructured mesh.

4.5.3 Divergence schemes

The divergence of a property Q describes the net rate at which it changes as a function of space and is defined as:

$$\nabla \cdot Q \tag{4.10}$$

And if **Q** is a vector quantity:

$$\nabla \cdot \mathbf{Q} = \frac{\partial Q_x}{\partial x} + \frac{\partial Q_y}{\partial y} + \frac{\partial Q_z}{\partial z} \tag{4.11}$$

The default discretization scheme that is used for divergence terms is none (not specified). Divergence schemes are specified in the divSchemes sub-dictionary using the general syntax:

```
divSchemes
{
    default         none;
    div(Q)          Gauss <interpolation scheme>;
}
```

This includes also the advective term where the transport of **Q** is under the influence *phi* which represents the (volumetric) flux of velocity on the cell faces for constant-density flows and the mass flux for compressible flows such that it is written div(phi,Q) (e.g. div(phi,k) for the advection of turbulent kinetic energy). There are many schemes implemented in OpenFoam, only few schemes will be presented here which are:

- **Bounded Gauss Upwind:** first-order bounded, generally it is not accurate. Usually, the physics of the flow is not captured correctly. But it is the most stable scheme for convection dominated flows. Therefore, it can be used to generate an initial stable solution.

- **Gauss linearUpwind:** second-order, upwind-biased, unbounded. Usually, it is required to limit the gradient of the cell center to prevent instabilities and oscillations of the solution domain because of the presence of peaks on the face center that are greater than neighboring cells which is not physical.
- **Gauss limitedLinear <coff>:**linear scheme that limits towards upwind in regions of rapidly changing gradient; requires a coefficient, where 1 is the strongest limiting, tending towards linear as the coefficient tends to 0. It is bounded using a Sweby limiter. 'V'-schemes are specialized versions of schemes designed for vector fields.

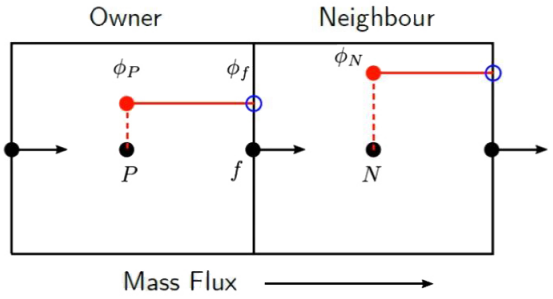

Figure 4.11: Gauss upwind discretization scheme.

4.5.4 Laplacian schemes

The *Laplacian Schemes* sub-dictionary contains Laplacian terms. A typical Laplacian term is the diffusion term in the momentum equations, which corresponds to the keyword laplacian(nu, U) in laplacianSchemes. The Gauss scheme is the only choice of discretization and requires a selection of both an interpolation scheme for the diffusion coefficient, nu, and a surface normal gradient scheme: Gauss 'interpolationScheme' 'snGradScheme'. The most important part for the discretization of the Laplacian is related to the discretization of the surface normal gradient with SnGradScheme because in all cases, the linear interpolation scheme is used for interpolationScheme of the diffusivity. Possible available choices are the following one:

- *Gauss linear corrected*
- *Gauss linear limited corrected 0.33*
- *Gauss linear limited corrected 0.5*
- *Gauss linear limited orthogonal*
- *Gauss linear limited uncorrected*

The basis of the gradient calculation at a face is to subtract the value at the cell centre on one side of the face from the value in the centre on the other side and divide by the distance. The calculation is second-order accurate for the gradient normal to the face if the vector connecting the cell centres is orthogonal to the face, i.e. they are at right-angles. This is the *orthogonal* scheme.

Orthogonality requires a regular mesh, typically aligned with the Cartesian coordinate system, which does not normally occur in meshes for the real world, and of course, in the adopted mesh. Therefore, to maintain second-order accuracy, an explicit non-orthogonal correction can be added to the orthogonal component, known as the *corrected* scheme. The correction increases in size as the non-orthogonality, the angle α between the cell-cell vector and face normal vector, increases. As α tends towards 90 degrees, the explicit correction can be so large to cause a solution to go unstable, since it produces a sparser matrix.

The solution can be stabilized by applying the *limited*. Typically, ψ is chosen to be 0.33 or 0.5, where 0.33 offers a greater stability and 0.5 a greater accuracy. The corrected scheme applies under-relaxation in which the implicit orthogonal calculation is increased with an equivalent boost within the non-orthogonal correction. The uncorrected scheme is equivalent to the corrected scheme, without the non-orthogonal correction. Generally, the uncorrected and orthogonal schemes are only recommended for meshes with very low non-orthogonality (e.g. maximum 5 degrees). The corrected scheme is generally recommended, but for maximum non-orthogonality above 60 degrees, limited may be required.

4.5.5 Surface normal gradient schemes

The *snGradSchemes* sub-dictionary contains surface normal gradient terms, which is evaluated at cell face. It is the component, normal to the face, of the gradient of values at the centres of the 2 cells that the face connects, which is used to evaluate Laplacian term using Gaussian integration:

$$\int_{V_p} \nabla \cdot (\rho\Gamma_\phi \nabla\phi) = \sum_f S \cdot (\rho\Gamma_\phi \nabla\phi)_f = \sum_f (\rho\Gamma_\phi)_f S \cdot (\nabla\phi)_f \tag{4.12}$$

The surface normal gradient scheme is necessarily specified to calculate the $S \cdot (\nabla\phi)_f$ The available schemes are listed in Table 4.5 and are specified by simply quoting the keyword and entry, with exception of Limited which requires a

coefficient ψ, $0 \leq \psi \leq 1$

$$\psi = \begin{cases} 0 & \text{corresponds to uncorrected,} \\ 0.333 & \text{non-orthogonal correction} \leq 0.5\times \text{ orthogonal part,} \\ 0.5 & \text{non-orthogonal correction} \leq \text{orthogonal part,} \\ 1 & \text{corresponds to corrected.} \end{cases} \tag{4.13}$$

It should be highlighted that the choice of different surface normal gradient schemes usually depends on the non-orthogonality of the mesh. The general examples will be given in the Laplacian schemes part.

Table 4.5: Surface normal gradient schemes

Scheme	Description
corrected	Explicit non-orthogonal correction
uncorrected	No non-orthogonal correction
limited ψ	Limited non-orthogonal correction
bounded	Bounded correction for positive scalars
fourth	Fourth order

4.5.6 fvSchemes for the non-reacting and reacting cases

The finite volume discretization schemes (fvSchemes) dictionary is shown in Figure 4.12 for both the non-reacting and reacting case. The non-reacting case is simulated using the SIMPLE algorithm, wheres the reacting cases are simulated using combustion solvers that are based on the Weller and CFM combustion models.

In the reacting analysis, it has been selected the Euler scheme which is a transient, first-order implicit and bounded scheme:

```
ddtSchemes
{
default Euler;
}
```

Imposing the default option means that the scheme will be applied to all the time first derivative terms of the Navier-Stokes, continuity, momentum, combustion, and turbulence equations. While the non-reacting case is a steady-state simulation and no discretization schemes are required for the time derivatives.

A second-order accurate scheme is selected for the gradient term in both cases. The value at the face center ϕ_f is determined by linear interpolation between the primary cell center and the neighboring cell center. This type of scheme does not

need a further correction when a high-quality computational mesh is used, as the case in this study.

The divergence scheme `Gauss limitedLinear1` is used in many terms in order to avoid non-physical results, when the tendency of oscillation of the solution generates values outside the physical range of the problem. It is bounded using a Sweby limiter.

The laplacian scheme is `Gauss linear corrected` in both cases, meaning that the Gauss scheme is used for discretization with a linear interpolation of the diffusivity. The most important part for the discretization of the Laplacian is related to the discretization of the surface normal gradient with SnGradScheme and it is of second-order accuracy if the vector connecting the two cell centres is orthogonal to the face. In case if the maximum non-orthoganality in mesh exceeds 5 degrees, then a `corrected` scheme is used to account for this non-orthoganality.

Non-reacting case

```
ddtSchemes
{
    default         steadyState;
}

gradSchemes
{
    default         Gauss linear;
}

divSchemes
{
    default         none;

    div(phi,U)            bounded Gauss linearUpwind grad(U);
    div(phi,k)            bounded Gauss limitedLinear 1;
    div(phi,epsilon)      bounded Gauss limitedLinear 1;
    div(phi,omega)        bounded Gauss limitedLinear 1;
    div((nuEff*dev(T(grad(U))))  Gauss linear;
    div((nuEff*dev2(T(grad(U))))) Gauss linear;
    div(nonlinearStress)          Gauss linear;
}

laplacianSchemes
{
    default          Gauss linear corrected;
}

interpolationSchemes
{
    default          linear;
}
snGradSchemes
{
    default          corrected;
}

fluxRequired
{
    default          no;
    p;
    Phi;
}

wallDist
{
    method           meshWave;
}
```

Reacting case

```
ddtSchemes
{
    default Euler;
}

gradSchemes
{
    default         Gauss linear;
    grad(p)         Gauss linear;
}

divSchemes
{
    default          none;

    div(U)                              Gauss linear;
    div(phi,U)                          Gauss linearUpwind grad(U);
    div(phi,Z2)                         Gauss limitedLinear 1;
    div(phi,YNOPollutant)               Gauss limitedLinear 1;
    div(phi,YNOPollutantCFD)            Gauss limitedLinear 1;
    div(phi,YNOCFDRifSource)            Gauss limitedLinear 1;
    div(phi,NOx)                        Gauss limitedLinear 1;
    div(phi,NOxMix)                     Gauss limitedLinear 1;
    div(phi,k)                          Gauss limitedLinear 1;
    div(phi,epsilon)                    Gauss limitedLinear 1;
    div(phi,Sigma)                      Gauss limitedLinear 1;
    div(phiU,p)                         Gauss limitedLinear 1;
    div(phid,p)                         Gauss limitedLinear 1;
    div(phi,Yi_h)                       Gauss limitedLinear 1;
    div(phiSt,c)                        Gauss limitedLinear 1;
    div(phiSt,b)                        Gauss limitedLinear 1;
    div((phiSt|interpolate((cMax-c0))),c) Gauss limitedLinear 1;
    div((phi|interpolate(rho)),p)       Gauss limitedLinear 1;
    div(phiXi,Xi)                       Gauss limitedLinear 1;
    div((muEff*dev2(T(grad(U)))))       Gauss linear;
    div((phi|interpolate(rho)),cNp)     Gauss limitedLinear 1;
    div((phi|interpolate(rho)),rhosFv)  Gauss limitedLinear 1;
    div((U+((Su*Xi)*grad(b))))          Gauss linear;
    div((Su*grad(b)))                   Gauss linear;
    div((U+((Su0*Xi)*grad(b))))         Gauss linear;
    div((Su0*grad(b)))                  Gauss linear;
}

laplacianSchemes
{
    default                             Gauss linear corrected;
}

interpolationSchemes
{
    default          linear;
    interpolate(HbyA) linear;
}

snGradSchemes
{
    default          corrected;
}

fluxRequired
{
    default          no;
    p;
    Phi;
}
```

Figure 4.12: Finite volume discretization schemes.

4.5.7 fvSolution for the non-reacting and reacting cases

In this subsection, the fvSolution of the reacting case will be discussed first and then the non-reacting case.

The equation solvers, tolerances, and algorithms are managed from the file `fvSolution` dictionary in the `system` directory.

Linear solver control

The first sub-dictionary in the `fvSolution` file is solvers. It determines the *linear-solver* which refers to the method of number-crunching to solve a matrix equation. In this sub-dictionary, the variable to be solved in the particular equation is specified, followed by the solver scheme, pre-conditioner, tolerance and relative tolerance. For example:

```
"(U|h|hu|enthalpy|c|b|cForRR|Sigma|Xi)"
{
solver PBiCGStab;
preconditioner DILU;
tolerance 1e-8;
relTol 0.1;
}
```

Where the PBiCGStab stands for stabilized preconditioned (bi-)conjugate gradient, for both symmetric and asymmetric matrices. A (bi-)conjugate method belongs to the iterative solver methods opposed to direct solvers, which gives an exact solution but with high CPU time. It is based in an iterative procedure of multi-grid methods that start from mapping the solution of a coarse mesh into more refined ones to accelerate the solution process. Thus the high-frequency errors are easily removed, going faster to the convergence of the solution.

The preconditioner is DILU which stands for diagonal incomplete-Cholesky (symmetric) and incomplete-LU (asymmetric). It is used to improve the efficiency in looking for the correct direction to get the right solution. Finally, the tolerance and relative tolerance are specified as criteria of convergence. The convergence criteria are achieved based on one of these scenarios: the residual is lower than the absolute *tolerance*; the ratio of current to initial residual is lower than the *relTol*; the number of iterations exceeds the maximum specified number *maxIter*. The solution algorithm is specified in a sub-dictionary such as SIMPLE, PISO (Pressure Implicit with Splitting of Operators), or PIMPLE. In the reacting case, the PIMPLE algorithm operating in a PISO mode was used.

The PIMPLE algorithm is working in PISO mode has been used, which utilizes the PISO solution algorithm to solve time-dependent compressible flows. It is used to couple the pressure and momentum quantities whilst satisfying the mass conservation. The number of outer loops (i.e. momentum predictor steps) was generally set at 1, with the number of inner loops (i.e. pressure corrector steps) set at 1. The non-orthogonal correctors is set to be 15 for $\theta > 65$. No under-relaxation was used between outer loops and the turbulent parameter transport equations were solved at each outer loop. For each outer corrector, the momentum equation is solved while for each inner corrector the pressure equation is solved.

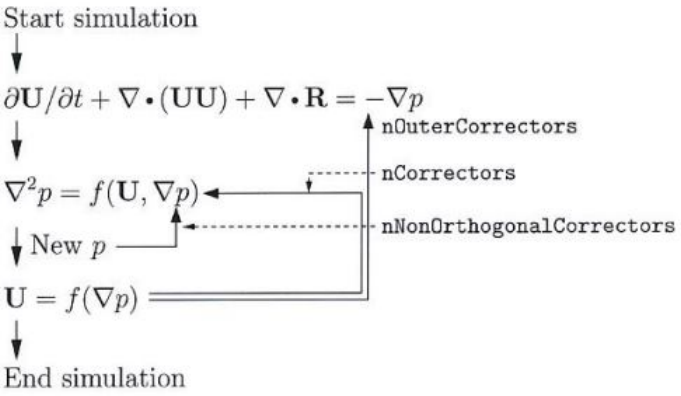

Figure 4.13: Flow chart of the PISO algorithm

The PIMPLE sub-dictionary is as follows:

```
PIMPLE
{
momentumPredictor off;
nOuterCorrectors 1;
nCorrectors 1;
nNonOrthogonalCorrectors 15;
}
```

On the other hand, for the non-reacting case, the SIMPLE algorithm is used with an under-relaxation of the pressure and velocity. The linear-solver was selected to be GAMG (geometric-algebraic multi-grid) with GaussSeidel smoother. The generalized method of geometric-algebraic multi-grid (GAMG) uses the principle of: generating a quick solution on a coarse mesh; mapping this solution onto a finer mesh; using it as an initial guess to obtain an accurate solution on the fine mesh which make the solution process faster. The user is only required to specify an approximate mesh-size at the most coarse level in terms of the number of cells.

Chapter 5

Simulation Results and Discussions

In this chapter, the main results achieved for the assessment of the Weller flame area combustion model on the TSF burner are included and discussed. First, the non-reacting case A-i2 is validated. Then, the reactive cases A-r and G-r are simulated using the one-equation and two-equations Weller model, and a comparison between these versions of the model is conducted. After that, a first attempt to model NO_x for both flames is performed under the adiabatic assumption. Finally, a preliminary assessment of the CFM model is carried out.

5.1 Non-reacting validation case Ai-2

The non-reacting case Ai-2 is basically used to assess the numerical setup and the mesh quality before advancing to the reactive cases. No combustion modelling is required because of the nature of the case, and the governing equations reduce to equations 3.1 and 3.6. Basically, in case Ai-2, pure air is flowing out from all pipes with a bulk velocity of 10 m/s surrounded by a coflow of 0.1 m/s. The characteristics of this case are described in Table 2.1.

The RANS simulations were done using the SIMPLE algorithm. The boundary conditions of this case are shown in Table 5.1. The boundary condition type for the `'axis'` patch is set to be `empty`, in fact, the axis line contains no cells since the mesh is considered to be axi-symmetric. Regarding the `'front'` and `'back'` patches, they have been set as a `wedge` boundary type in all involved field variables.

The `fixedValue` boundary condition imposes a user-specified value on the boundary patch that does not change during simulations. Another important boundary condition is `zeroGradient` which implies that the normal gradient of the patch field is equal to zero, i.g. the boundary patch assumes the same value of the internal field cell next to the boundary itself. The condition `inletOutlet` is basically a `zeroGradient` condition when flow outwards, `fixedValue` when flow is inwards. The condition `kqRWallFunction` provides Neumann boundary condition, that means it enforces a `zeroGradient` condition. It is worth mentioning that this wall function type is only suitable for high-Re turbulence models, e.g. the standard $k-\epsilon$ model. However, for the case of low-Re models such as the $k-\omega$ SST, the `kLowReWallFunction` is used and it is based on the position of y+. Finally, the `omegaWallFunction` is used for the $k-\omega$ SST model. This wall function implemented in OpenFOAM is a special wall function which can switch between viscous and logarithmic region according to the position of y+.

The velocity inlet boundary condition is mapped from the separate cyclic-flow simulations that resulted in fully turbulent flow fields shown previously in section 4.4, and then considered as a `fixedValue`. Also k, ϵ and ω fields are mapped form the cyclic-flow simulations for consistency reasons.

Table 5.1: Boundary conditions for the case A-i2.

Boundary	P	U	k	ϵ	ω
inletPilot	zeroGradient	fixedValue (mapped)	TIKEI*(mapped)	TMLDRI*(mapped)	TMLFI*(mapped)
inletSlot1	zeroGradient	fixedValue (mapped)	TIKEI (mapped)	TMLDRI (mapped)	TMLFI (mapped)
inletSlot2	zeroGradient	fixedValue (mapped)	TIKEI (mapped)	TMLDRI (mapped)	TMLFI (mapped)
inletCoflow	zeroGradient	fixedValue	TIKEI	TMLDRI	TMLFI
outlet	fixedValue	inletOutlet	inletOutlet	inletOutlet	inletOutlet
rightSide	zeroGradient	slip	slip	slip	slip
Walls	zeroGradient	fixedValue	kqRWallFunction	epsilonWallFunction	omegaWallFunction

*TIKEI stands for turbulentIntensityKineticEnergyInlet, while TMLDRI and TMLFI means turbulentMixingLengthDissipationRateInlet and turbulentMixingLengthFrequencyInlet, respectively.

In Figure 5.1, the mean axial and radial velocity results from the RANS simulations are compared with the experimental measurements. Near the burner exit at low axial locations, the trend shows three hump-shaped axial velocity profiles because of the presence of mixing shear layers behind the wake of the concentric pipes caused by three outflow jets. Further downstream, the velocity humps smear out due to the flow mixing. Both turbulence models showed a satisfactory agreement of mean axial velocity with experimental measurements. The slight over-prediction at y = 1 mm of the mean axial velocity in the wake of

slot 1 wall of the $k-\epsilon$ model might be due to the coarse mesh that is required near the wall to achieve a y+>30 while maintaining the use of the structured grid. Also, the agreement of mean radial velocity, in particular at y = 50 mm to y = 100 mm, is satisfactory.

Figure 5.2 shows the distribution of the turbulent kinetic energy at various locations downstream of the burner. Three peaks are found at y = 1 mm due to the presence of the mixing shear layers. Further downstream the burner, the flow is mixed and only one peak appears due to the velocity gradient between the jet flows and the co-flow. Both models performed well, in particular at y = 50 mm and y = 100 mm, however, the $k-\epsilon$ model shows more consistent results with experimental measurements especially at y = 1 mm compared to the $k-\omega$ SST model.

The good agreement of the numerical results from both turbulence models with the cold flow experimental data of the case A-i2 indicates that the numerical setup, the mesh quality, and the way of imposing the boundary conditions are indeed suitable to numerically study the TSF burner and advance to the combustion cases.

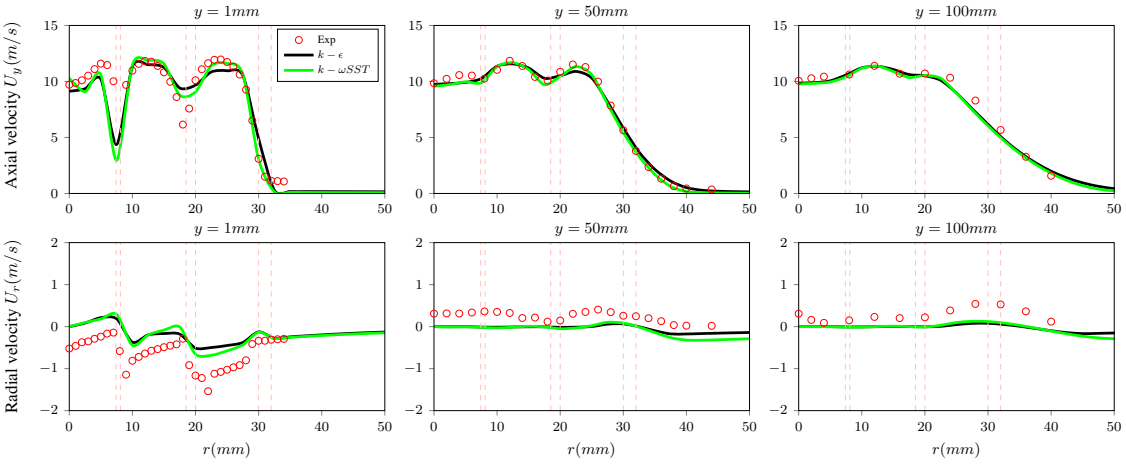

Figure 5.1: Mean axial and radial velocities at various axial locations y for the non-reacting case A-i2. Hereafter, the vertical pink dashed-lines correspond to the radial positions of the inner and outer walls of the pilot, slot 1, and slot 2, respectively.

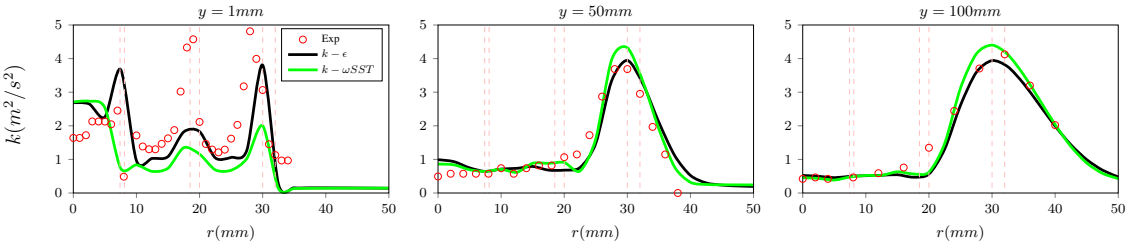

Figure 5.2: Turbulent kinetic energy k at various axial locations y for the non-reacting case A-i2.

5.2 Stratified reactive case A-r

5.2.1 Cold flow initialization

The first step towards simulating the reactive case A-r is to initialize the fields until it reaches a steady-state condition before igniting the mixture. The characteristics of this reactive case (A-r) are described in Table 2.1. The major challenges related to this first step is the proper initialization of:

- the flow velocity and turbulence fields of the three annular pipes;
- the distribution of the mixture fraction Z.

The flow velocity and turbulence initialization are based on the cyclic-flow simulations that were performed previously in section 4.4. However, the pilot pipe flow velocity is set to be 1 m/s since the flow there is laminar before ignition. In theory, the velocity profile at the pilot exit should also reach a value of around 10 m/s after ignition because of the pilot flame. The boundary conditions for the reactive case A-r are given in Table 5.2 and 5.3. The fuel–air equivalence ratio ϕ (denoted here by Eqvr) is equal to 0.9 at the inlet of the pilot and slot 1, while it is equal to 0.6 at the inlet of slot 2 to achieve stratification in the mixture. Thus, a simple conversion analysis from equivalence ratio to mixture fraction Z reveals that $Z \approx 0.05$ at the pilot and slot 1 inlet, while at slot 2 inlet $Z \approx 0.0338$. All other species are initialized accordingly, in particular the reactants CH_4, O_2, and N_2, while combustion products and intermediate species are assigned a `zeroGradient` boundary condition. The OpenFOAM utility `setFields` was used to initialize the mixture fraction field Z inside the three pipes. The same boundary conditions apply to flame G-r, except that the equivalence ratio at the inlet of slot 2 is equal to 0.9 to achieve a fully premixed homogeneous combustion as described in Table 2.1.

Table 5.2: Boundary conditions for the reactive cases A-r and G-r.

Boundary	P	U	Z	k
inletPilot	zeroGradient	fixedValue (mapped)	fixedValue	TIKEI (mapped)
inletSlot1	zeroGradient	fixedValue (mapped)	fixedValue	TIKEI (mapped)
inletSlot2	zeroGradient	fixedValue (mapped)	fixedValue	TIKEI (mapped)
inletCoflow	zeroGradient	fixedValue	fixedValue	TIKEI
outlet	fixedValue	inletOutlet	zeroGradient	inletOutlet
rightSide	zeroGradient	slip	zeroGradient	slip
Walls	zeroGradient	fixedValue	zeroGradient	compressible::kqRWallFunction

Table 5.3: Boundary conditions of ϵ and ω fields for the reactive cases A-r and G-r.

Boundary	ϵ	ω
inletPilot	compressible::TMLDRI (mapped)	compressible::TMLFI (mapped)
inletSlot1	compressible::TMLDRI (mapped)	compressible::TMLFI (mapped)
inletSlot2	compressible::TMLDRI (mapped)	compressible::TMLFI (mapped)
inletCoflow	compressible::TMLDRI	compressible::TMLFI
outlet	inletOutlet	inletOutlet
rightSide	slip	slip
Walls	compressible::epsilonWallFunction	compressible::omegaWallFunction

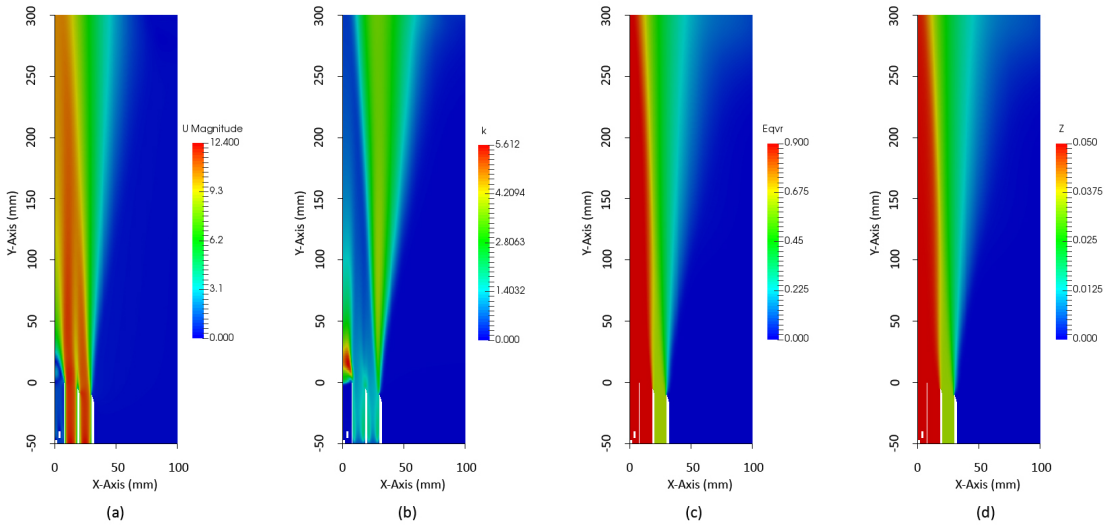

Figure 5.3: Fields initialization of the reactive flow A-r: (a) velocity field $U_{magnitude}(m/s)$, (b) turbulent kinetic energy $k(m^2/s^2)$,(c) Equivalence ratio $Eqvr(-)$ and (d) mixture fraction $Z(-)$.

5.2.2 Initial assessment of Weller model for case A-r

The Weller model was implemented in the solver `betaFlameletXiFoam` which was used in this analysis to simulate flame A-r, which features stratification between

the two annular slots, slot 1 and slot 2. The aim of this analysis is to assess the capability of the one-equation and two-equations Weller combustion model for stratified combustion applications and compare them. First of all, a sensitivity analysis of the effects of the turbulence model, ignition near the flame holder, the pilot inlet turbulence intensity, and the pilot inlet mean velocity has to be conducted. A complete explanation of the one-equation and two-equations Weller model is presented in section 3.4.1.

The initialized fields resulted from the cold flow simulations, as shown in Figure 5.3, are used as the initial time step for the reactive case A-r in the folder `0` with the same boundary conditions shown in Table 5.2 and 5.3. The settings and characteristics of the spark ignitions and the spark kernel initial diameter are included in the file `combustionProperties` inside the `constant` folder. The ignition parameters of the Weller model are as follows:

```
ignitionSites
(
{
location (4e-4 -38e-3 0.0) ;
diameter 4e-3;
start 0.0;
duration 3e-3;
strength 3.5;
electricDelay 0;
}
);
```

The chosen diameter is able to ignite a little quantity of the mixture and at the same time trigger complete combustion of the mixture. The intensity is selected in a way to sustain the ignition and ensure proper propagation of the flame in the pilot. It is worth mentioning that, the sensitivity of the ignition parameters is not included here because it affects only the initial transient part of the flame propagation while the simulation here is concerned with the steady-state condition after the flame is stabilized and does not change anymore.

Regarding the **chemistry modelling**, a flamelet database is generated in OpenFOAM-LibICE by representing the flame as an unstretched freely propagating premixed flame with a unity Lewis numbers assumption. The tabulated kinetic scheme is described in section 3.4.4. The fuel is methane and the non-normalized progress variable is defined here as the sum of HO_2, CO, H_2O and CO_2 mass fractions. This information is included in the file `chemistryProperties` inside the `constant` folder as follows:

```
progressVariableType multiSpecies;
multiSpeciesCoeffs
{
whatToTabulate h298;
speciesNames (HO2 CO H2O CO2);
coefficients (1 1 1 1 );
}
```

The first simulation is carried out using the one-equation Weller model with Gulder correlation for the equilibrium wrinkling factor Ξ^*_{eq} as shown in equation 3.43. However, the influence of the different sub-models for Ξ^*_{eq} on the mean flame brush will be discussed in the next sections along with the two-equation model version. Figure 5.4 shows the evolution of the flame temperature after igniting the mixture near the flame holder. The standard $k-\epsilon$ and the $k-\omega$ SST are used for modelling turbulence.

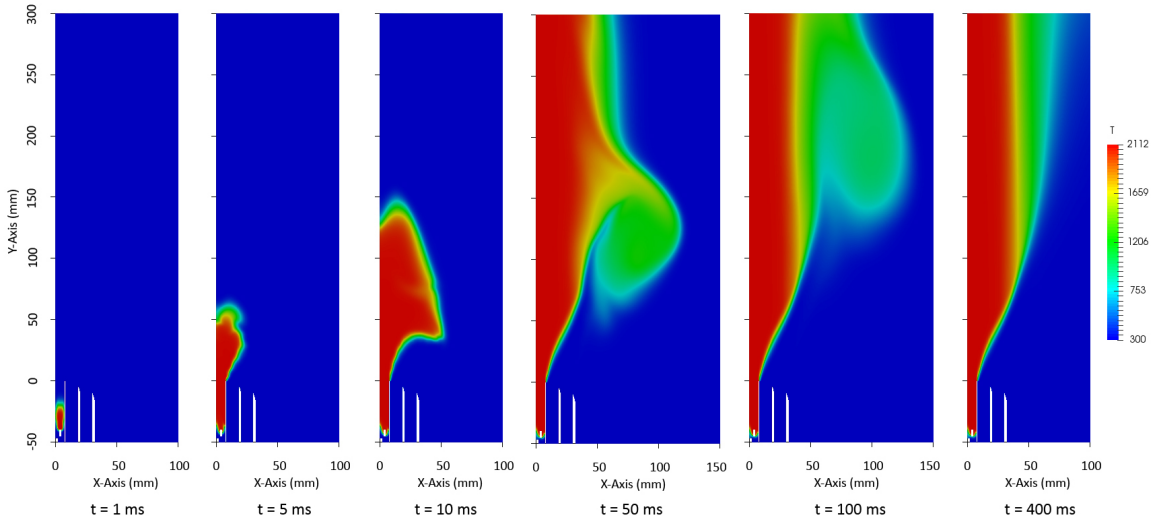

Figure 5.4: Snapshots of the evolution of the temperature field $T(K)$ of flame A-r at various time steps using the one-equation Weller model with Gulder correlation for Ξ^*_{eq}.

- **Sensitivity to turbulence model**

The objective of this section is first to identify the results sensitivity to the turbulence model. For that purpose, the simulation of flame A-r is performed under adiabatic assumption on two different grids presented previously in section 4.3 with the use of the standard $k-\epsilon$ and $k-\omega$ SST for modelling turbulence and the one-equation Weller model using Gulder correlation for the equilibrium wrinkling factor Ξ^*_{eq}. Mean velocity fields, turbulent kinetic energy, and temperature fields predicted by both simulations are compared with the experimental measurements in Figures 5.5, 5.6, 5.7, and 5.5, respectively.

Figure 5.5 shows that mean axial velocity profiles have a wider jet spreading angle compared the non-reacting case A-i2 shown in Figure 5.1. This is attributed to the heat expansion caused by the reactive flow. The adiabatic RANS simulation overestimates the axial velocity and the flame position is shifted towards larger radii because of the under-predicted density in the pilot near the centerline. This deviation shows that the velocity, turbulent kinetic energy and temperature fields near the burner exit are very sensitive to the heat loss in the pilot wall.

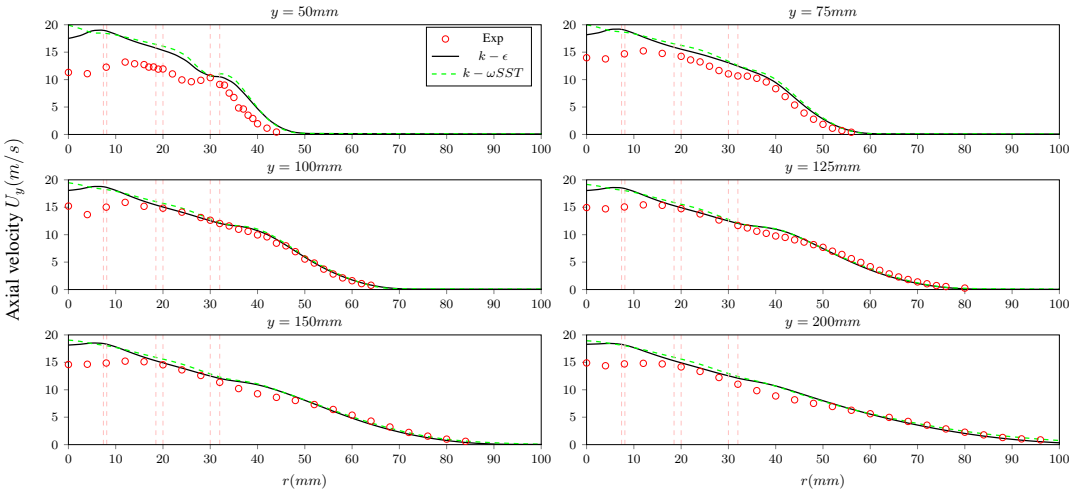

Figure 5.5: Mean axial velocity U_y at various axial locations y for the reactive case A-r.

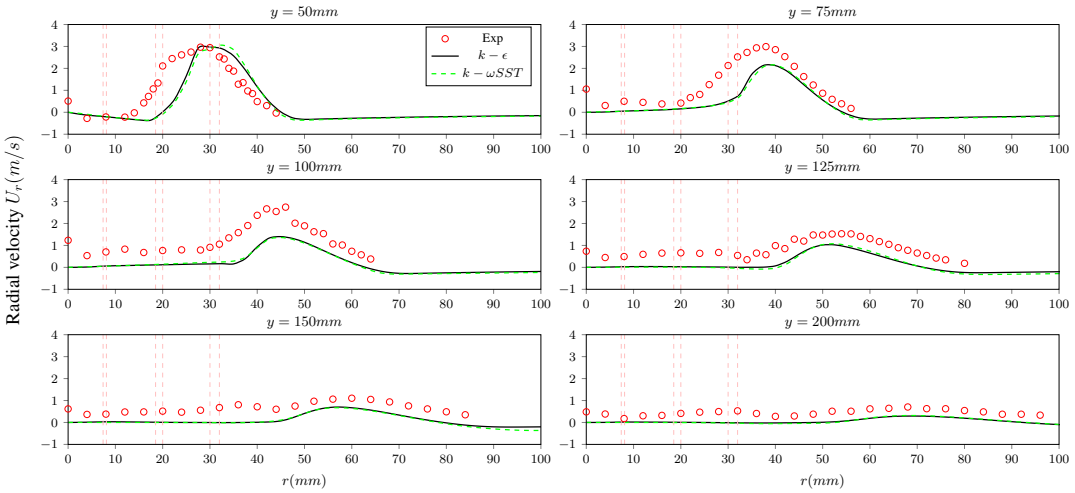

Figure 5.6: Mean radial velocity U_r at various axial locations y for the reactive case A-r.

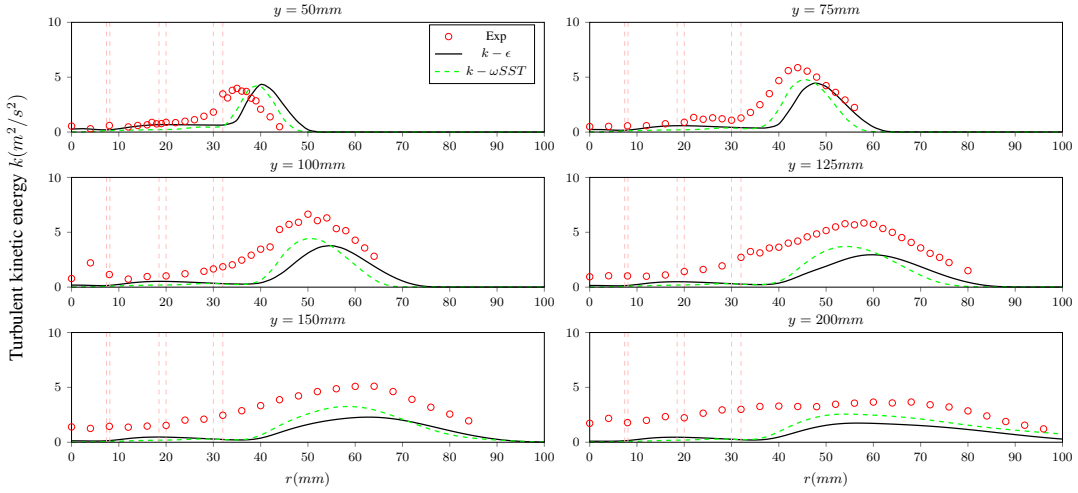

Figure 5.7: Turbulent kinetic energy k at various axial locations y for the reactive case A-r.

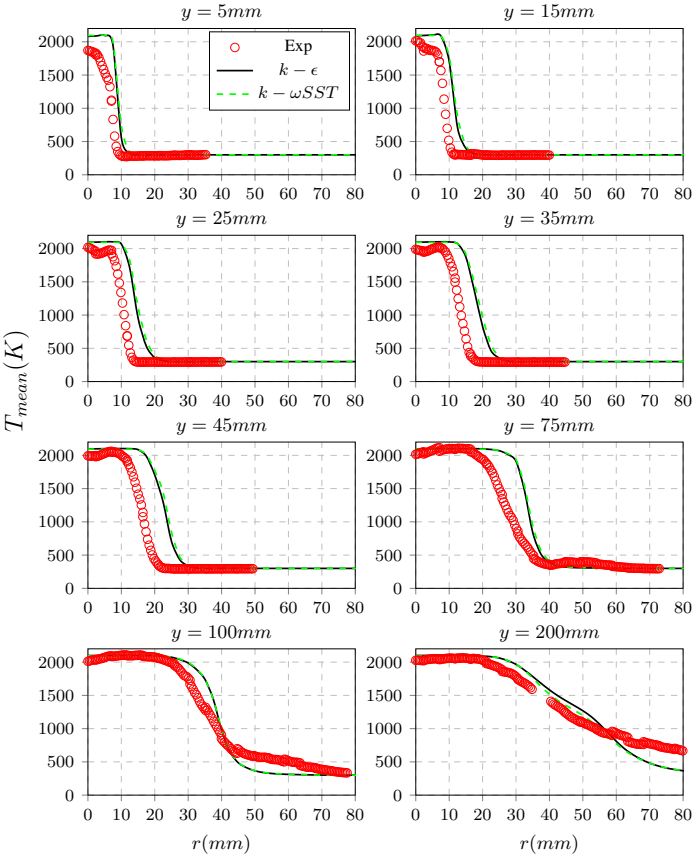

Figure 5.8: Mean temperature T at various axial locations y for the reactive case A-r.

As expected, the results are found to be weakly sensitive to the used turbulence model except for downstream the pilot region where the modelling of the wake behind the flame holder influences the stream-wise velocity distribution. As little differences are observed, the standard $k-\epsilon$ model is well-suited to the present configuration and shows a better agreement with experimental data of the mean axial velocity, particularly downstream of the pilot region. Therefore, the standard $k-\epsilon$ model is selected for the rest of the next simulations in the thesis.

However, to improve the overall results especially for the axial velocity profile at y = 50 mm and the radial shift of the temperature profiles, it has been decided to remove the flame holder part from the mesh and consider a fully burnt mixture inlet boundary condition for the pilot region. The only modification of the mesh is to remove the flame holder so that the pilot inlet is selected to be y = 15 mm upstream of the burner exit (the reader is referred to Figure 5.13 case b). This, as will be shown later in next sections, improved the results substantially because the Weller combustion model is originally suited for turbulent premixed combustion while near the flame holder region the flow is laminar and the turbulence intensity is very low, which might cause a misprediction of the correct flow field. In fact, it will

be shown that low turbulence intensity values in the pilot region provide a better agreement with experimental measurements, however, reducing the turbulence intensity in this region causes misfiring of the mixture in the case of ignition near the flame holder.

Another important sensitivity analysis is related to the pilot inlet boundary conditions considering a fully burnt mixture. There are no accurate experimental measurements of such quantities (velocity and turbulence fields) inside the pilot, however, the burner was designed in such a way to have a mean axial velocity exiting the pilot after ignition of about 10 m/s [31]. An investigation of such effects can result in a better agreement between simulations and experimental data.

- **Sensitivity to the pilot turbulence intensity considering a fully burnt mixture inlet condition**

The turbulent kinetic energy k (TKE) is a very important condition defined as mean kinetic energy per unit mass associated with eddies in a turbulent flow. Accurate prescription of TKE as initial conditions in CFD simulations are important to accurately predict flow fields, especially in high Reynolds-number simulations. It is expressed as:

$$k = \frac{3}{2}(IU)^2 = \frac{3}{2}(u')^2 \tag{5.1}$$

where I is the initial turbulence intensity in percentage (%), and U is the reference velocity magnitude. u' is the turbulent velocity component defined here as the turbulence intensity in (m/s). Since the standard $k-\epsilon$ turbulence model has been used, the solution of the ϵ transport equation 3.24 is problematic in the near-wall regions due to the term ϵ/k which represents a singularity near the walls. Thus the `compressible::kqRWallFunction` is used to overcome this issue. However, due to the lack of experimental data of this quantity inside the pilot, a sensitivity analysis is carried out. The flow inside the pilot is initially laminar, meaning that the turbulence intensity is expected to be very low after ignition. Thus the initial turbulence intensity I is varied and namely takes the values of $1\%, 5\%$, and 10% of a reference velocity that is the pilot inlet velocity $U_{pilot} = 9m/s$. The reason for choosing this value for the pilot inlet velocity will be demonstrated in the next section. Consequently, u' takes the values of 0.9, 0.45, and 0.09 m/s.

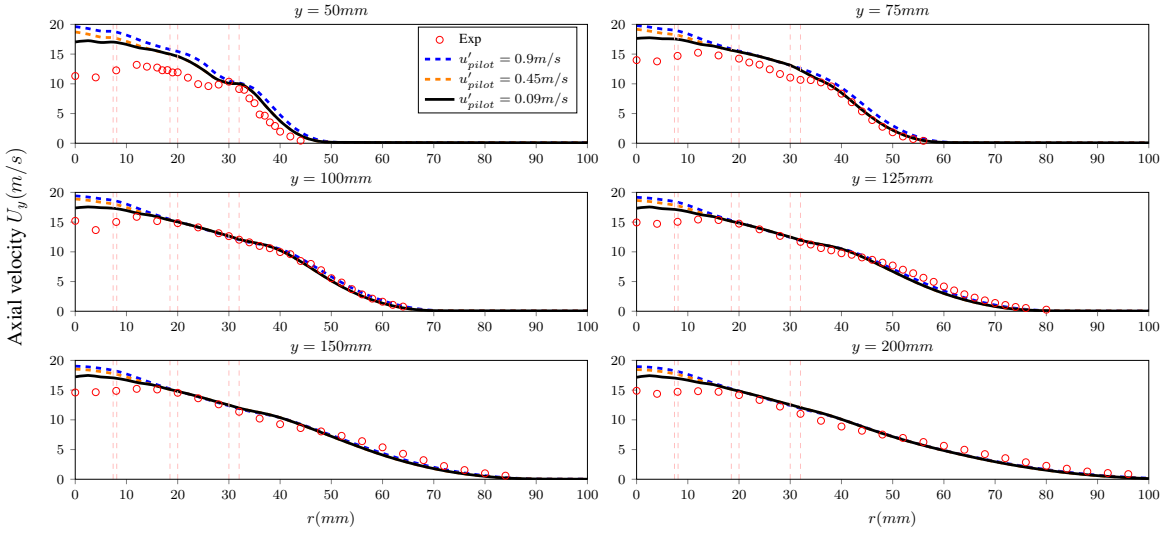

Figure 5.9: Mean axial velocity U_y at various axial locations y for the reactive case A-r by imposing different pilot turbulence intensities u'_{pilot} considering a fully burnt mixture flow, using Gulder correlation for Ξ^*_{eq}.

Figure 5.9 illustrates that considering a fully bunt mixture at the pilot inlet with a very low turbulence intensity ($u'_{pilot} = 0.09m/s$) shows a less expansion of the flow at y = 50 mm and a less radial shift of the mean axial velocity profile compared to the case of igniting the mixture inside the pilot shown previously in Figure 5.5. As expected, it is observed that the most influenced region by the reduction of turbulence intensity is downstream of the pilot region. Far away from the centerline, the effect is not significant and the velocity profiles are in good agreement with experimental data.

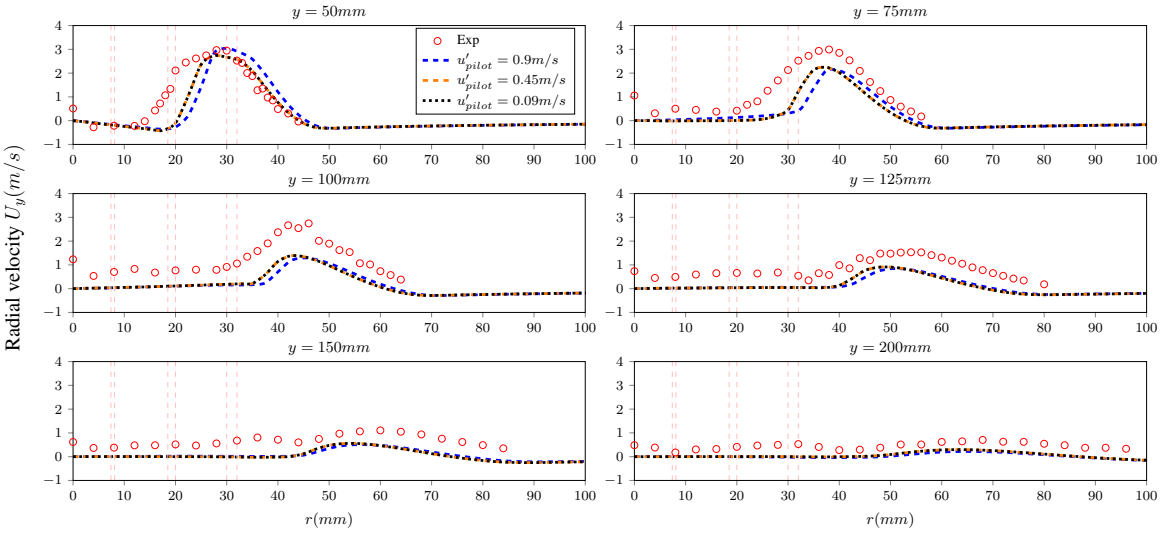

Figure 5.10: Mean radial velocity U_r at various axial locations y for the reactive case A-r by imposing different pilot turbulence intensities u'_{pilot} considering a fully burnt mixture flow, using Gulder correlation for Ξ^*_{eq}.

The influence of decreasing the turbulence intensity in the pilot region on the mean radial velocity profiles is depicted in Figure 5.10. It is clear that the velocity profiles are shifted towards the centerline and thus better matching the locations of the peaks shown in the experimental measurements. However, a slight underprediction of the magnitude is noticed at locations beyond y = 75 mm.

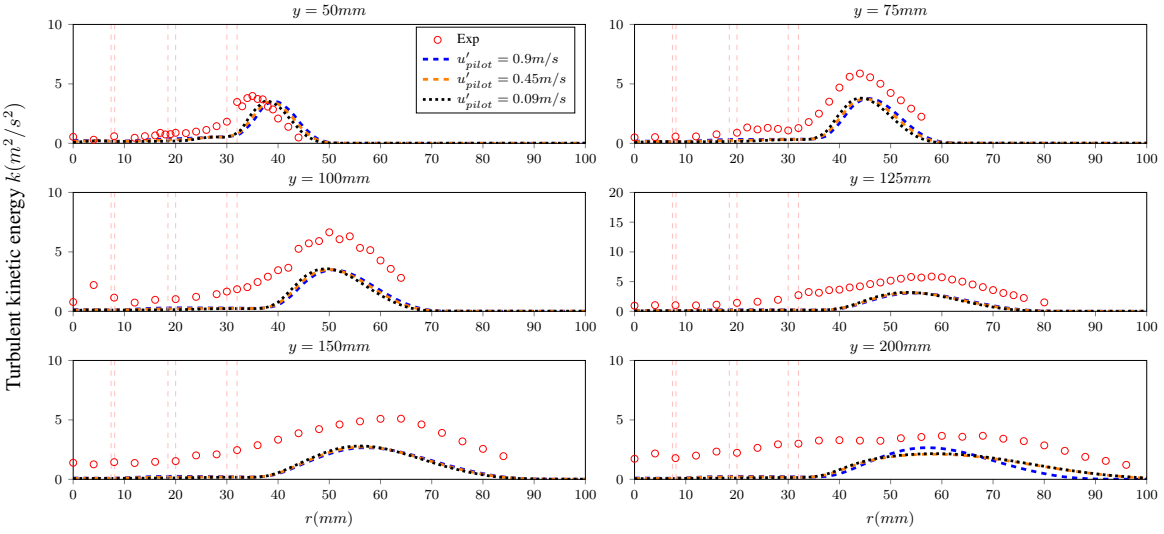

Figure 5.11: Turbulent kinetic energy k at various axial locations y for the reactive case A-r by imposing different pilot turbulence intensities u'_{pilot} considering a fully burnt mixture flow, using Gulder correlation for Ξ^*_{eq}.

Finally, the sensitivity of the turbulent kinetic energy profiles at various axial locations to the turbulence intensity in the pilot region is illustrated in Figure

5.10. The turbulent kinetic energy can show the instability of the flow. With the decrease of turbulence intensity, the TKE profiles are shifted radially toward the centerline matching the peak of experimental data except at y = 50 mm. The peak missing phenomenon could be attributed to the inaccurate flame front prediction, which affects the jet flow expansion, since the hump away from the centerline could be triggered by velocity gradients between the jet flow and the co-flow.

Therefore, low turbulence intensity values at the pilot inlet, in particular $u'_{pilot} = 0.09m/s$, show a better agreement with experimental data and will be adopted hereafter. The complete results of the sensitivity analysis on temperature and main species will be shown in the coming sections to avoid unnecessary repetition.

- **Sensitivity to the pilot mean velocity considering a fully burnt mixture inlet condition**

The need for this sensitivity analysis arises from the uncertainty of the mean axial velocity at the pilot inlet. Many studies showed such calibration of the pilot inlet velocity adjusted to match the experimental profile [48]. All simulations were run starting from the previously suggested result of a pilot turbulence intensity of $u'_{pilot} = 0.09m/s$. The pilot mean axial velocity U_{pilot} was varied from 9 to 11 m/s.

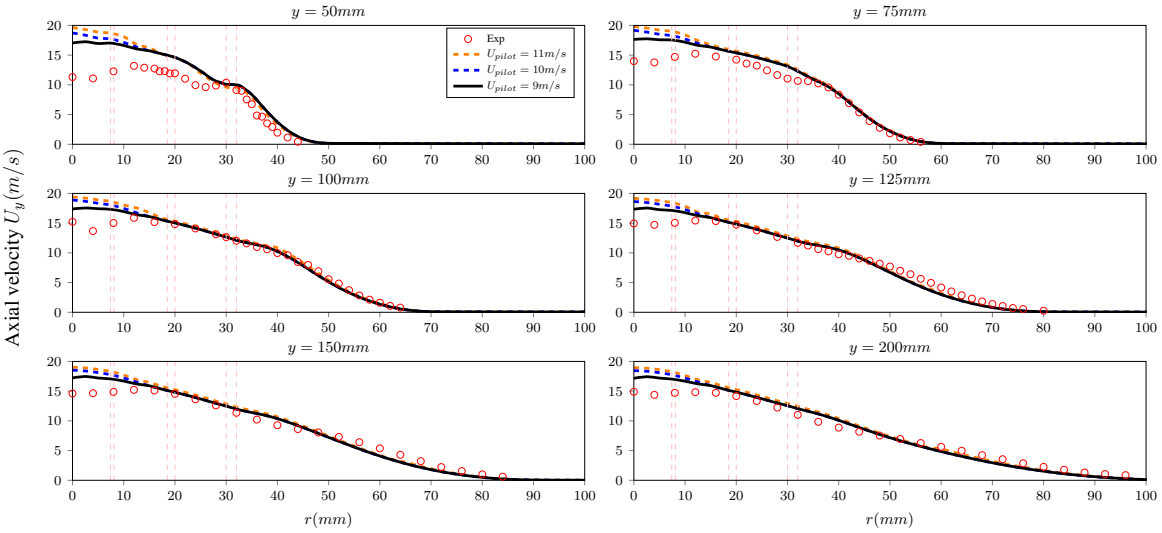

Figure 5.12: Mean axial velocity U_y at various axial locations y for the reactive case A-r by imposing different pilot inlet velocities U_{pilot} considering a fully burnt mixture flow, using Gulder correlation for Ξ^*_{eq}.

The results in Figure 5.12 suggest that calibration of the inlet mean axial velocity indicates that a lower mean axial velocity gives a better agreement to experimental data, however, decreasing the pilot velocity further will affect the

expansion of the flow causing a mismatch of the velocity profiles away from the centerline.

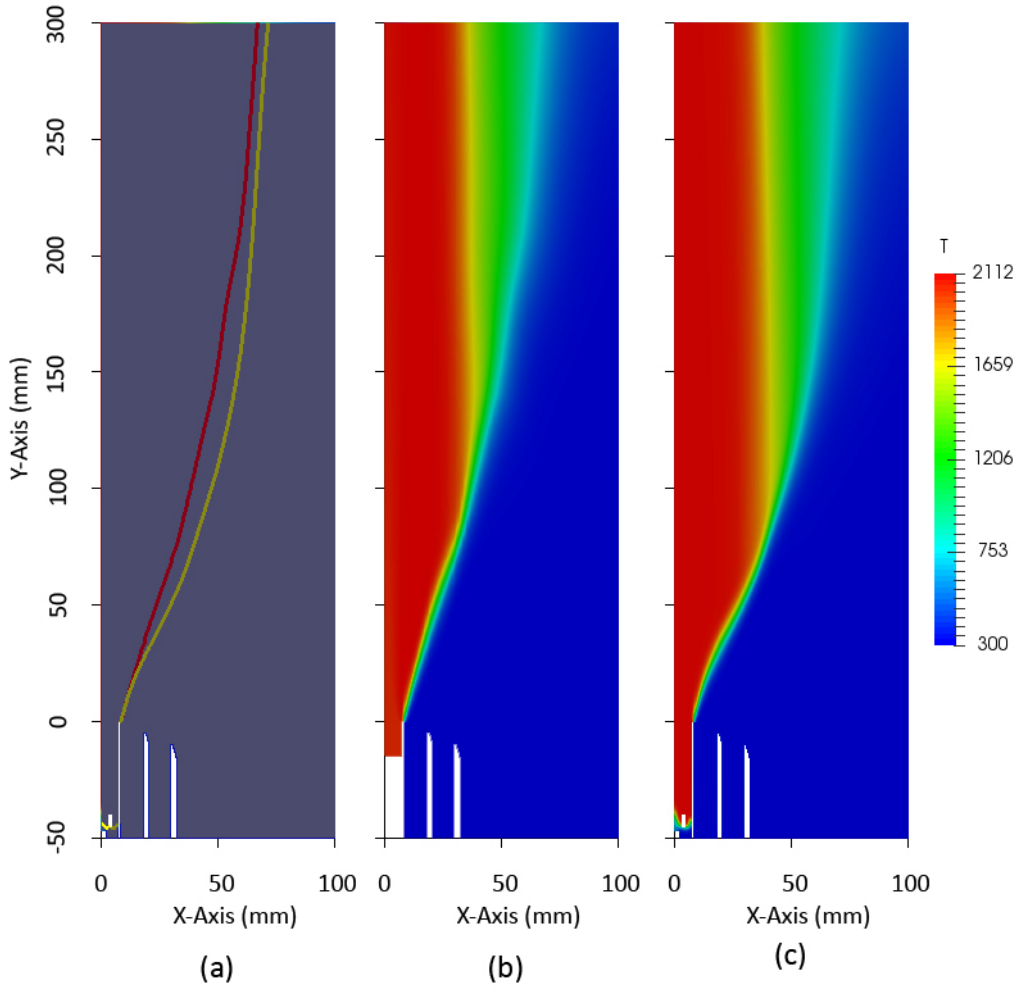

Figure 5.13: (a) Iso-line of mean temperature (750 K) for the adiabatic simulations. Red: in the case of a fully burnt mixture boundary condition (case b); yellow: in the case of ignition near the flame holder (case c). Mean temperature field of (b) fully burnt mixture boundary conditions, (c) ignition near the flame holder.

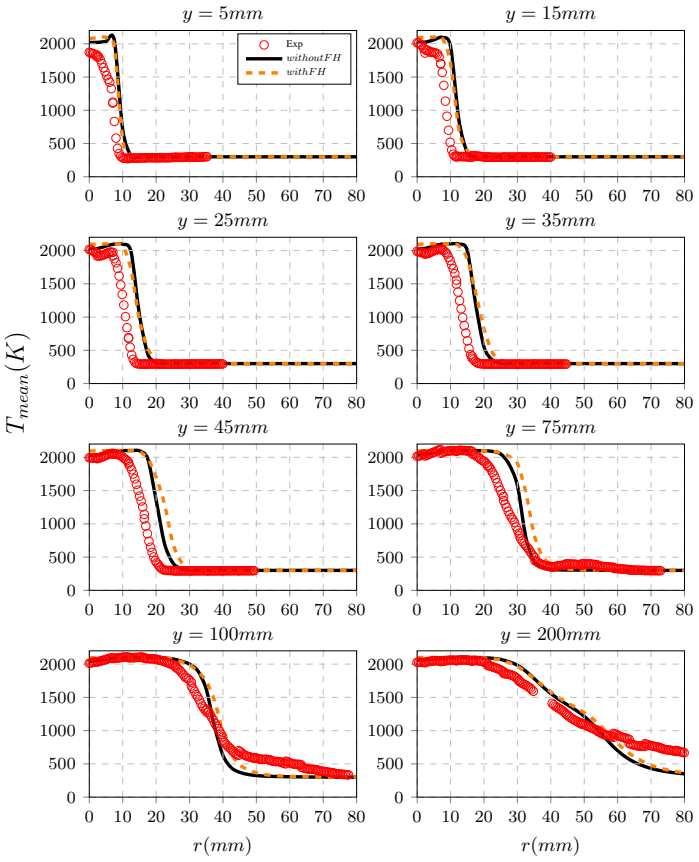

Figure 5.14: Mean temperature T at various axial locations y for the reactive case A-r. Black line: by imposing $U_{pilot} = 9m/s$ and $u'_{pilot} = 0.09m/s$ considering a fully burnt mixture flow without flame holder (without FH); Dashed orange line: the original case with ignition near the flame holder (with FH). FH stand for flame holder.

Finally, the combined effect on the temperature profiles of the sensitivity analysis applying a pilot inlet turbulence intensity of $u'_{pilot} = 0.09m/s$, and a mean axial velocity of $U_{pilot} = 9m/s$ considering a fully burnt mixture inlet condition compared to the case of igniting the mixture near the flame holder is shown in Figures 5.13 and 5.14. The iso-line of mean temperature for the adiabatic case simulation, shown in Figure 5.13 *(a)*, gives a good indication of the over-expansion of the temperature field in *case (c)* compared to *case (b)* which better matches the experimental data. This behavior is reflected in Figure 5.14 which indicates more consistent results of *case (b)* which is more shifted toward the centerline giving a better prediction of the mean temperature field. The slight mismatch is attributed to the adiabatic assumption of the pilot wall. In fact, the reaction products are cooled at the pilot wall and convected downstream.

5.2.3 One-equation Vs two-equations Weller model

In this subsection, the stratified flame A-r is simulated using the combustion model in which the wrinkling factor Ξ is modelled with an algebraic parameterized relation (one-equation model) or using a transport equation for Ξ (two-equations model). The detailed description of the Weller one-equation and two-equations model is presented in section 3.4.1. For the one-equation model, three algebraic closure correlations were considered in this study which are Peters (equation 3.42), Gulder (equation 3.43), and Muppala (equation 3.46) parameterized relations. The main calibration coefficients in these equations are $C = 2.0$ (suggested by Peters), $\Xi_{coef} = 0.62$ (suggested by Gulder) and $C = 0.46$ (suggested by Muppala). These calibration coefficients are based on interpolation of many experimental data. However, a slight variation and calibration of those coefficients show a better agreement with experimental data in this study, and parametric variation study is recommended. For example, a recent study by Muppala et al.[49] shows a need for fine-tuning of Muppala's correlation. The study shows that the coefficients $C = 0.46$ of Muppala's correlation needs to be tuned for each equivalence ratio which resulted in converged solutions and a correct prediction of the flame brush compared to experimental measurements. Hence, a parametric variation study on the main calibration coefficients is carried out.

It is found that in the one-equation model, the main calibration coefficients obtained from the interpolation of many experimental data for each correlation have an effect on the flame brush location and thus they affect also other dependent fields such as temperature, velocity, and species. This effect was more significant in Muppala's correlation, where the suggested value in this study of the main coefficient is $C = 0.9$ instead of 0.46. This can be justified by the fact that the ratio $\frac{C}{Le}$ is linked to the Lewis number which is assumed to be unity in this study, but in fact previous studies showed that this assumption can affect the solution [50]. Thus the incorporated uncertainties of Lewis number led to the selection of a higher value of the ratio $\frac{C}{Le} = 0.9$ with a unity Lewis number.

The coefficient Ξ_{coef} of Gulder's correlation was also slightly decreased from 0.62 to 0.50 to improve the agreement between numerical results and experimental data. This can be justified by the fact that turbulence is very low in the pilot region and cannot accurately be determined, leaving some uncertainties on the used values. Finally, Peters coefficient is selected to be the same as $C = 2.0$ which gives good agreement with experimental data. Table 5.4 summaries the suggested

main calibration coefficients in all correlations by their authors along with the ones tuned and suggested in this study.

Correlation	Suggested by the author of the correlation	Tuned in this study
Peters	$C = 2.0$	$C = 2.0$
Gulder	$\Xi_{coef} = 0.62$	$\Xi_{coef} = 0.50$
Muppala	$C = 0.46$	$C = 0.90$

Table 5.4: summary of the suggested main calibration coefficients in various correlations by their authors along with the ones tuned and suggested in this study.

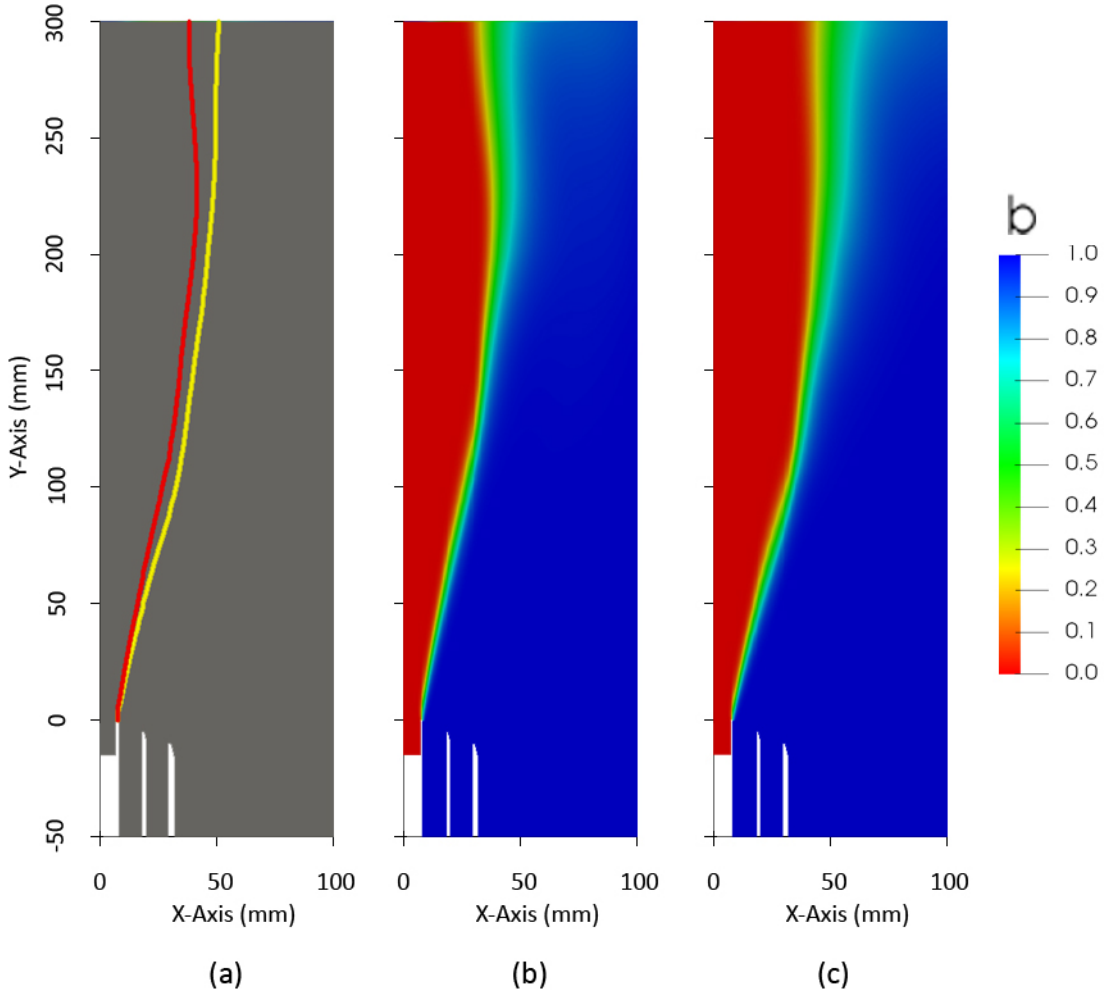

Figure 5.15: (a) Iso-line of a regress variable b=0.5 using Muppala's correlation C=0.46 (red) and C=0.90 (yellow). Regress variable b field for the case (b) with Muppala coefficient C=0.46, and the case (c) with C=0.90.

Figure 5.15 shows the parametric variation effect in the case of using Muppala's correlation with the suggested value by its author (C=0.46) compared to

the suggested value in this study (C=0.90). The regress variable color convention red (b=0) is burnt or combustion product gas and blue (b=1) is un-burnt. The iso-line of b=0.5 gives a good indication of the location of the flame front. The result shows that increasing the coefficient C makes the flame spread wider and improves the agreement between numerical and experimental data as will be shown in this section.

Simulations for the stratified flame A-r were carried out using the two-equations model ($\Xi - Trasport$) and the one-equation model with different correlations for Ξ^*_{eq} including the one from Peters, Gulder, and Muppala. Two simulations were carried out for Muppala correlation, one using the suggested value by Muppala C=0.46 ($\Xi^*_{eq} - Muppala$) and the other with the recommended value in this study C=0.9 ($\Xi^*_{eq} - Muppala$, $C = 0.9$) to show the effect of the main calibration coefficients on the results. Statistics of velocity, temperature, and species were assessed against experimental measurements obtained from the TU Darmstadt.

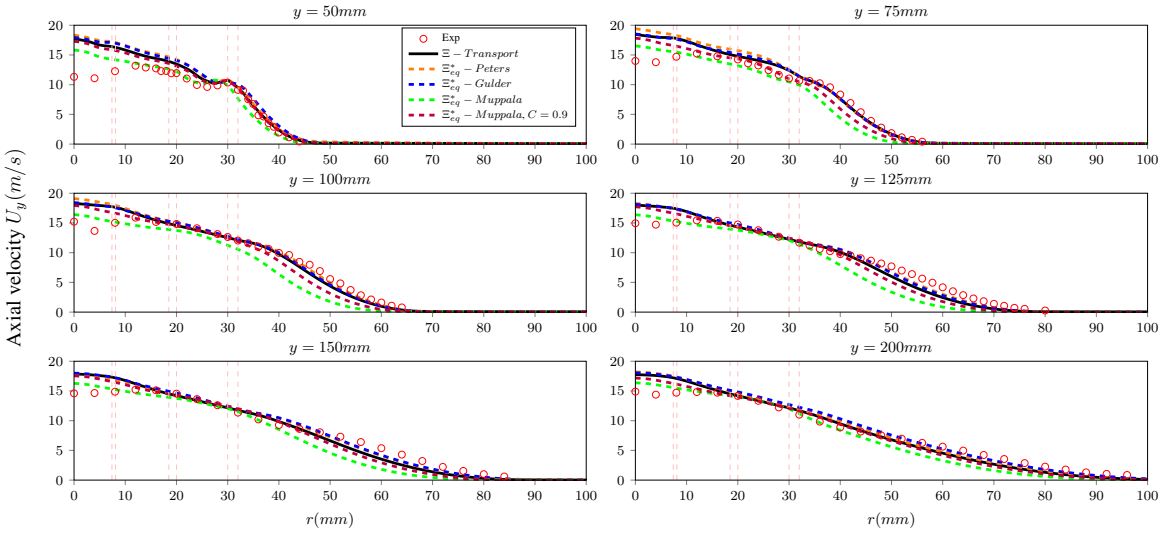

Figure 5.16: Mean axial velocity U_y for simulations with different flame wrinkling models at various axial locations y for the case A-r.

In Figure 5.16, the predicted mean axial velocities agree well with the experiment except of Muppala-C=0.46 in the faraway region from the burner exit with the increase of the radial direction ($\Xi^*_{eq} - Muppala$) (green dashed line). However, $\Xi^*_{eq} - Muppala$ model shows a rather good agreement in the region downstream from the centerline up to r = 30 mm at various axial locations suggesting that this correlation might be suitable for jet flows with narrow spreading angles. The decrease along the radial direction might be attributed to the lower turbulent flame speed S_T predicted by the correlation and with increasing C to 0.9 the results are significantly improved. At 50 mm above the burner exit, the peak due to the

flow from the outer tube (slot 2) is captured well, however, the velocity closer to the centerline is overpredicted due to the heat loss in the pilot tube that was not considered in this study. Further downstream, the spreading rate of the jet is well captured especially by Gulder, Peters correlations, and $\Xi - Transport$.

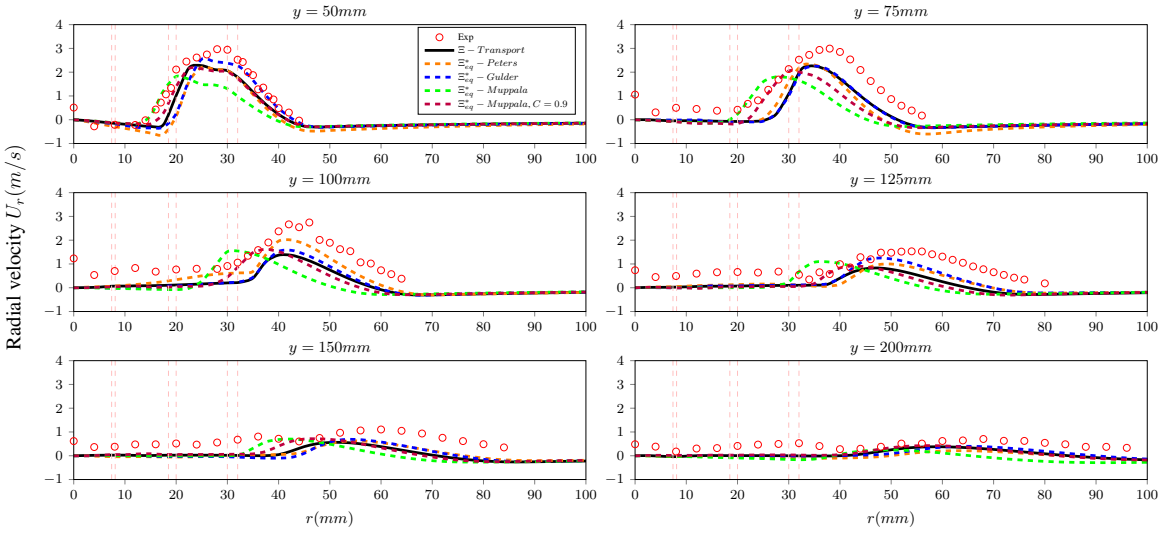

Figure 5.17: Mean radial velocity U_r for simulations with different flame wrinkling models at various axial locations y for the case A-r.

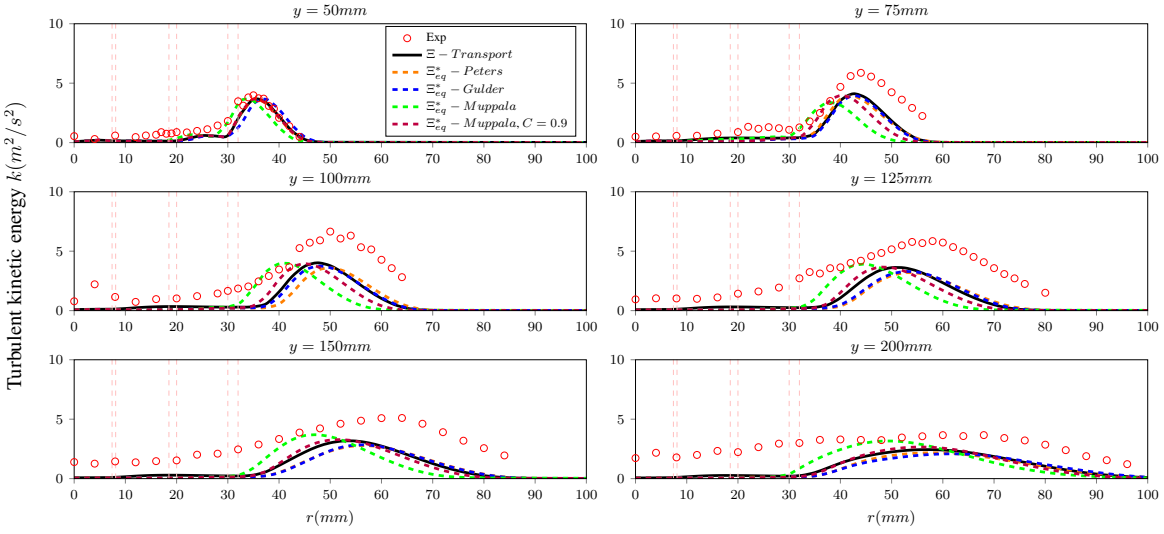

Figure 5.18: Turbulent kinetic energy k for simulations with different flame wrinkling models at various axial locations y for the case A-r.

The peak missing phenomena for Muppala correlation in the mean radial velocity and turbulent kinetic energy, as shown in Figures 5.18 and 5.19, implies an incorrect flame front prediction. The clear improvement is noticed with the calibrated coefficient of C=0.9 and this effect can be seen in Figure 5.15. All other flame wrinkling models showed a rather good agreement at y = 50 mm; further

downstream, a slight reduction is observed in the predicted magnitudes and can be explained by the uncertainties in the inlet boundary conditions.

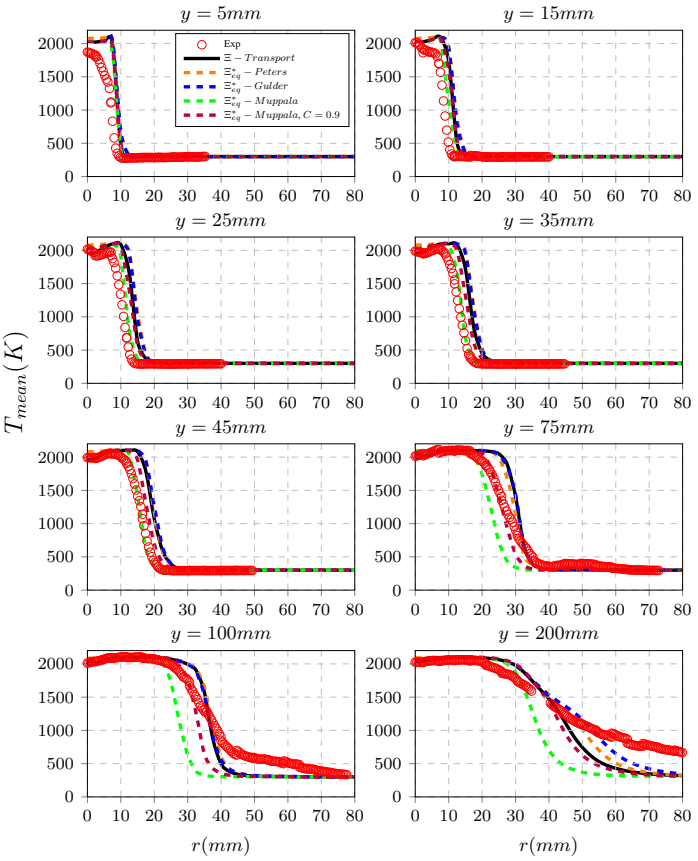

Figure 5.19: Mean temperature T for simulations with different flame wrinkling models at various axial locations y for the case A-r.

For the radial profiles of temperature, the results are shown in Figure 5.19. The general trend of the mean temperature is predicted well, except at the lower axial positions where the peak of temperature is overestimated in the center due to the adiabatic assumption of the pilot wall while heat loss is evident in many studies related to the TSF burner [26]. The heat loss has basically two primary effects. First, the relatively higher density than the considered by the adiabatic assumption and hence the velocity decreases, and second, the heat transfer phenomena taking place from the flame to the pilot wall reduces the reaction rate and thus the propagation speed is reduced as well. This may be the reason why the flame is slightly shifted towards higher radial positions in all simulations. However, further away from the pipe exit, this effect becomes less significant, since the mass flow of the pilot is small compared to the mass flow of slots 1 and 2, and the burnt gas temperature is well captured by the simulations.

The discrepancies start from the axial position y = 75 mm onwards, suggesting that the flame and turbulence interaction is particularly intricate in the range of 75 mm up to 100 mm where stratification is prevailing. In this region, the rate of reaction is slower than in upstream (higher equivalence ratio in upstream) and the turbulence–chemistry interaction plays an important role in the flow field behavior. Beyond 50 mm downstream, mostly pure mixing of the hot exhaust with cold coflow air is present. Also, the alignment of the mixing layer and the reaction layer starts to deviate in this region causing a differential diffusion effect that was not taken into account in this study as illustrated in Figure 5.20 (a). However, this misalignment is limited, in fact, the mixing and reaction layers can be considered almost parallel with a very small error.

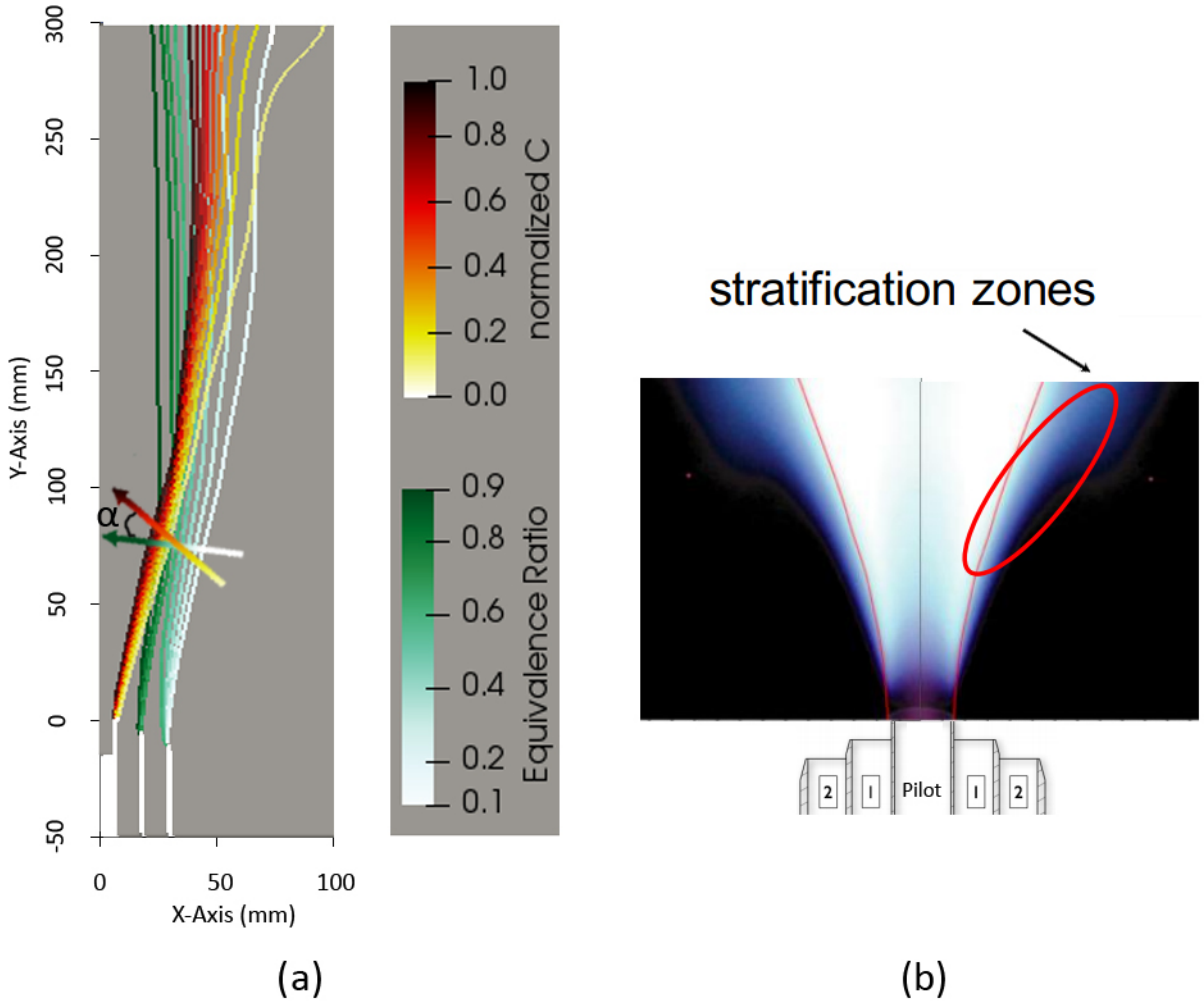

Figure 5.20: (a) Iso-lines of the normalized progress variable C and the equivalence ratio. Around y = 75 mm the ∇C from unburnt to burnt and $\nabla\phi$ or (∇Z) from lean to rich are illustrated, α is the alignment angle between the two gradients. (b) The stratification zones in flame A-r.

It has been shown by many researchers that the burning rate is influenced by the orientation of iso-C versus iso-Z contours where differential diffusion occurs across both of those contours [51, 52]. Depending on the angle α burning can be towards leaner ($\alpha = 0$ back-supported flames) or richer ($\alpha = \pi$ front-supported flames) equivalence ratio conditions. Pires Da Cruz et al. [51] found that the production of molecular hydrogen from the original fuel and its transport to the reaction zone as well as heat transfer from the burned to the fresh gases increase the burning rate in back-supported flames. Sforza [53] developed an LES model to take this effect into account in the TSF burner case A-r, the results indicate that the misalignment between the mixture and reaction layers is very small, hence, the gradients are almost always close to parallel. Therefore, this advanced issue of differential diffusion was neglected and not considered in this study.

In summary, all flame wrinkling models give a good prediction of the temperature profiles except Muppala which has been improved significantly when using C=0.9 especially at y = 75 mm. Further downstream, slight deviations from the experiment are noticed in the faraway regions with the increase of radial direction that might be due to the assumption of an adiabatic pilot wall and other effects that are not yet fully understood.

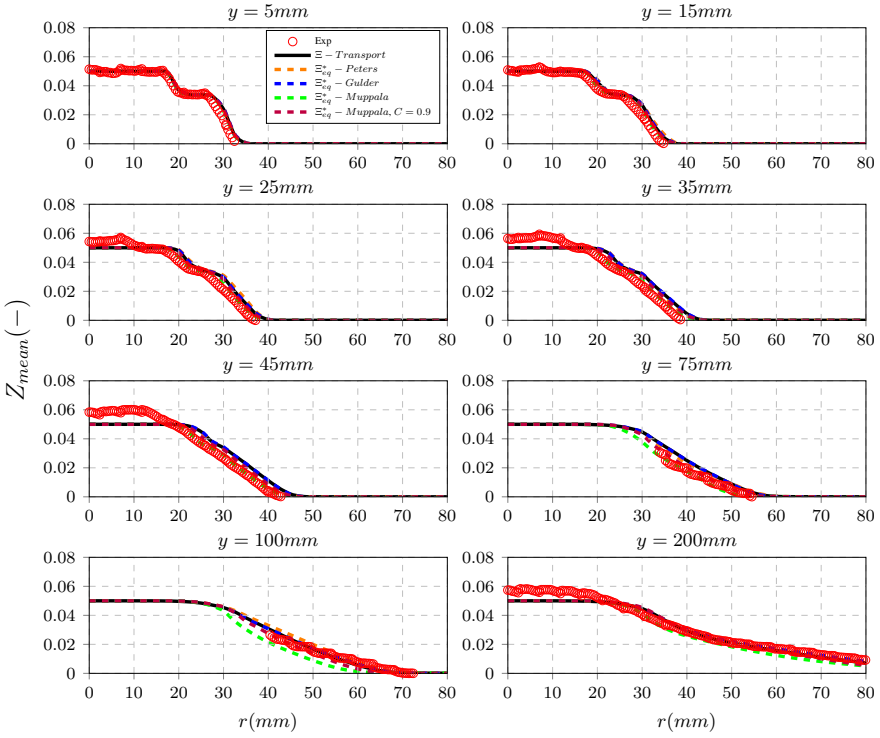

Figure 5.21: Mixture fraction Z for simulations with different flame wrinkling models at various axial locations y for the case A-r.

The mixture fraction Z is expected to reach its maximum at the burner exit and decrease as the injected flow is mixed with the co-flow. Thus, its maximum for this flame is $Z = 0.05$ corresponding to $\phi = 0.9$. The flamelet generated table depends on the progress variable and the mixture fraction, thus the accurate prediction of this scalar quantity is of great importance. All flame wrinkling models predicted well the mixture fraction at various axial locations. Unphysical values were observed close to the centerline causing an overestimation of the mixture fraction (see y = 25 mm and above). This was attributed to improper background corrections at low number densities of CO and CH4 by the experimentalists researchers from the TU Darmstadt [26]. By comparing the slope part of the results (the transition from $\phi = 0.9$ to $\phi = 0.6$ in slot 2 and finally into the coflow air) away from the centerline, the simulation shows a very good match to the experiments at all axial locations.

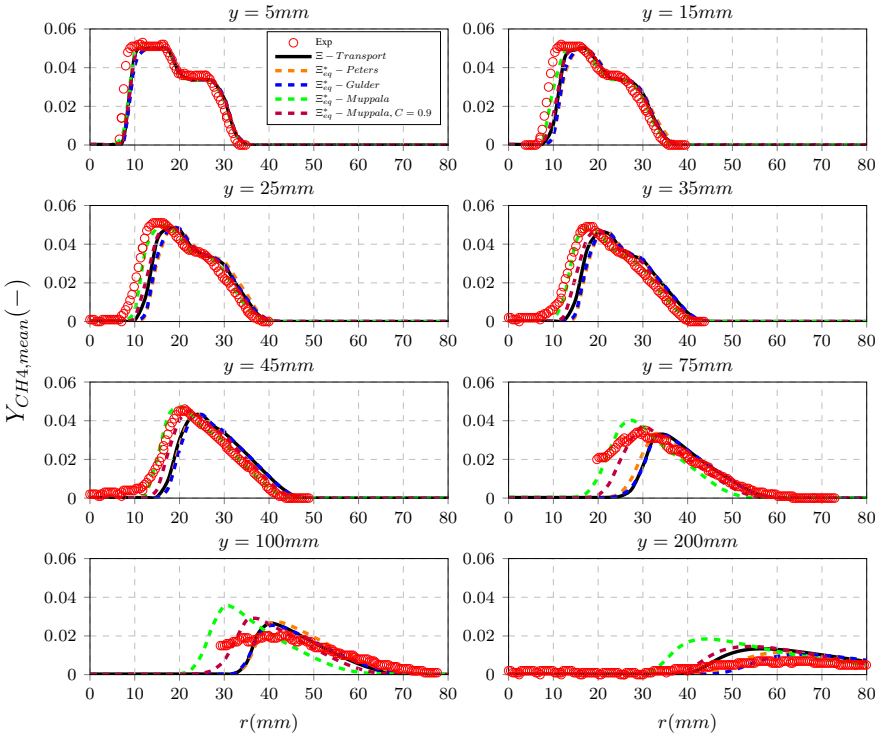

Figure 5.22: Mean mass fraction of CH_4 for simulations with different flame wrinkling models at various axial locations y for the case A-r.

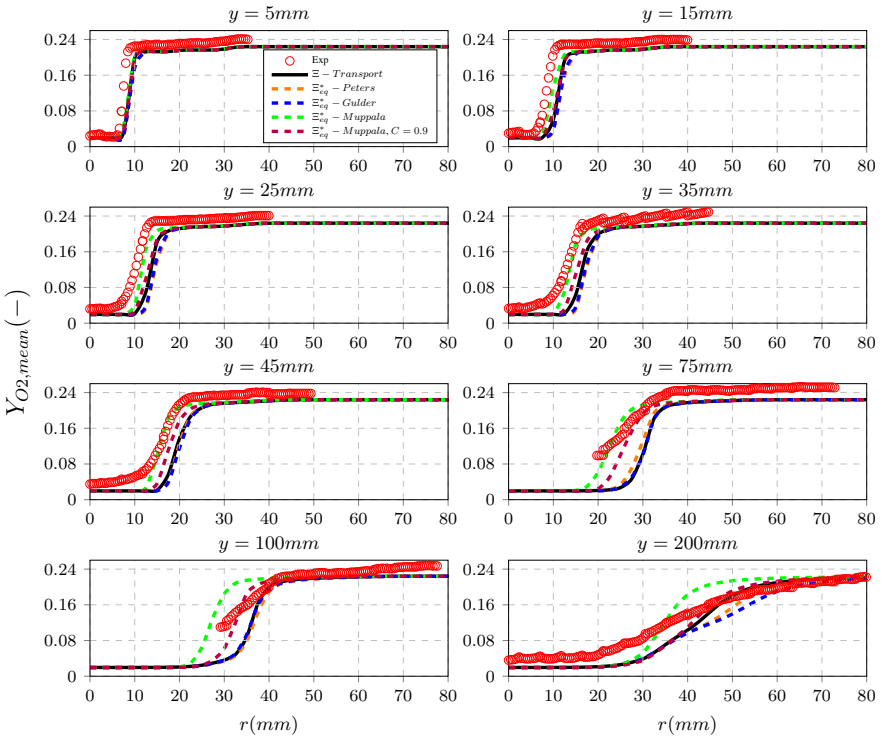

Figure 5.23: Mean mass fraction of O_2 for simulations with different flame wrinkling models at various axial locations y for the case A-r.

Figures 5.22 and 5.23 represent the mass fractions of the reactants of the combustion process which are CH_4 and O_2, respectively. In the pilot region that corresponds to high flame temperatures, the concentration of CH_4 and O_2 is very low suggesting complete combustion in that region, while at the lower temperature region higher concentrations are observed. Agreement between the RANS results and experimental data is good. Only a slight shift towards the radial direction is observed which is attributed to the slight shift of the temperature profile because of the adiabatic assumption of the pilot wall. Muppala shows a perfect agreement until y = 75 mm and then deviates significantly from experimental data suggesting the lack of accuracy of this correlation in stratified regions. However, the effect of tuning C=0.9 in Muppala's correlation indicates a significant improvement to the numerical results compared to the experiments. Very similar behavior was observed by Gulder, Peters, and $\Xi - Transport$. All models seem to lack the accuracy beyond y = 75 mm.

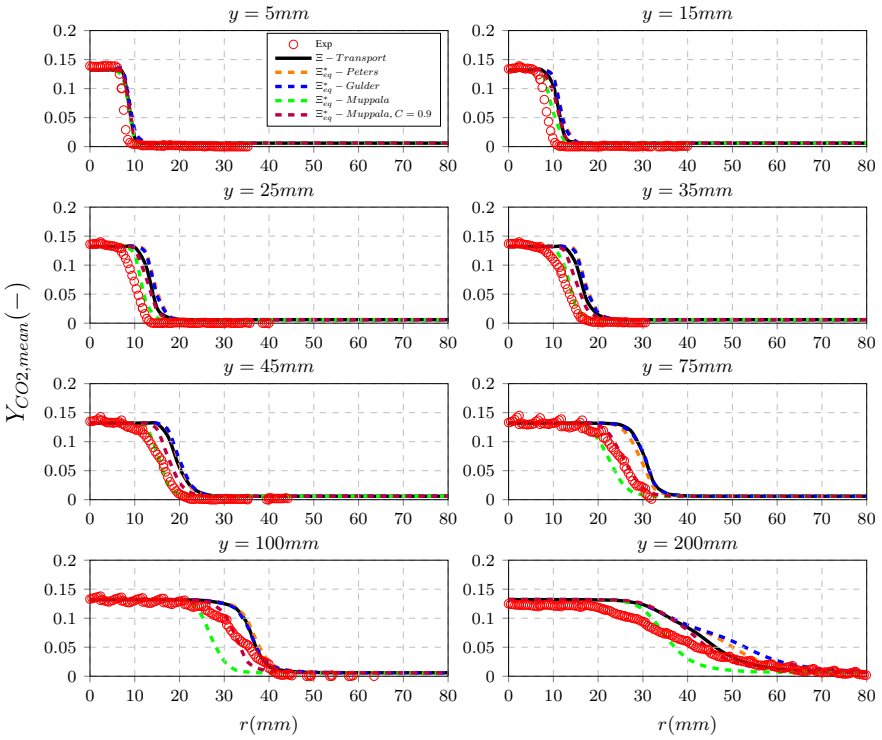

Figure 5.24: Mean mass fraction of CO_2 for simulations with different flame wrinkling models at various axial locations y for the case A-r.

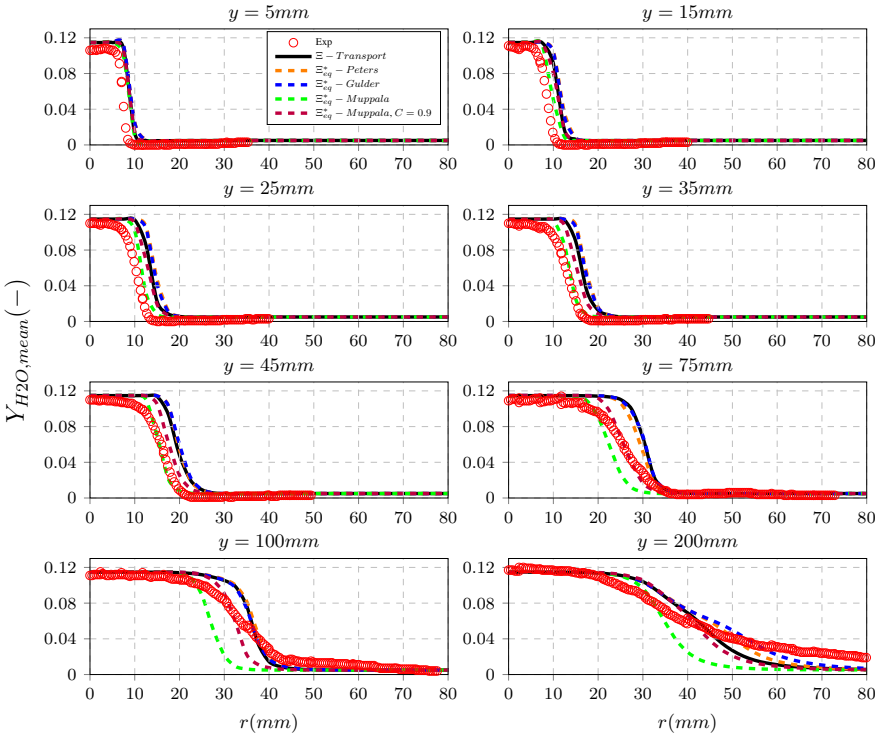

Figure 5.25: Mean mass fraction of H_2O for simulations with different flame wrinkling models at various axial locations y for the case A-r.

Figures 5.24 and 5.25 represent the mass fractions of the products of the combustion process which are CO_2 and H_2O, respectively. Radial shift is observed in all axial locations following the shift in the temperature profile, however, the general trend is in good agreement with the experiment. Muppala agrees well with the experiments up to y = 75 mm where stratification prevails, then a strong deviation is observed. The modified Muppala with C=0.9 shows an excellent agreement with the experiments, particularly at y = 75 mm, indicating that this correlation has promising results in stratified combustion compared to other models. Gulder, Peters and $\Xi - Transport$ show similar behavior except at y = 200 mm where Gulder and Peters indicate slightly higher values than $\Xi - Transport$ toward the radial direction.

Overall, the Weller model is able to predict stratified combustion successfully using the one-equation and the two-equations model. All models show a satisfactory level of agreement with experiment except Muppala where it shows rather good agreement only in narrow regions from centerline to r = 30 mm above the burner at various axial locations. Further in the radial direction, Muppala seems to lack accuracy in predicting the flow field correctly and the main calibration coefficient C is selected to take the value of 0.9 which shows significant improvements in the results. Similar behavior is observed between Gulder, Peters and $\Xi - Transport$ models. The general trend indicates that the one-equation model is as accurate as the two-equations model and can also give sometimes better results especially in the faraway regions with the increase of radial direction.

5.3 Fully premixed reactive case G-r

In this section, the fully premixed reactive case G-r is simulated basically because of three reasons, which are:

- To have a qualitative comparison with flame A-r and understand the effect of stratification and the difference between the two cases.
- To examine Muppala correlation where it shows a very good agreement in the case A-r up to y = 75 mm (where stratification prevails) indicating that it might be more suitable for fully premixed flames instead of stratified ones.
- To compare the NO_x profiles of the two cases and understand the significance of stratification on NO_x emissions which is of great interest of this study.

Flame G_r characteristics were introduced in Table 2.1. It is basically similar to flame A-r except that slot 2 has an equivalence ratio of 0.9 instead of 0.6 ensuring the reduction of the stratification effect. However, slight stratification will still be present in the transition region between slot 2 and the coflow. However, the core of the flow jet is fully premixed.

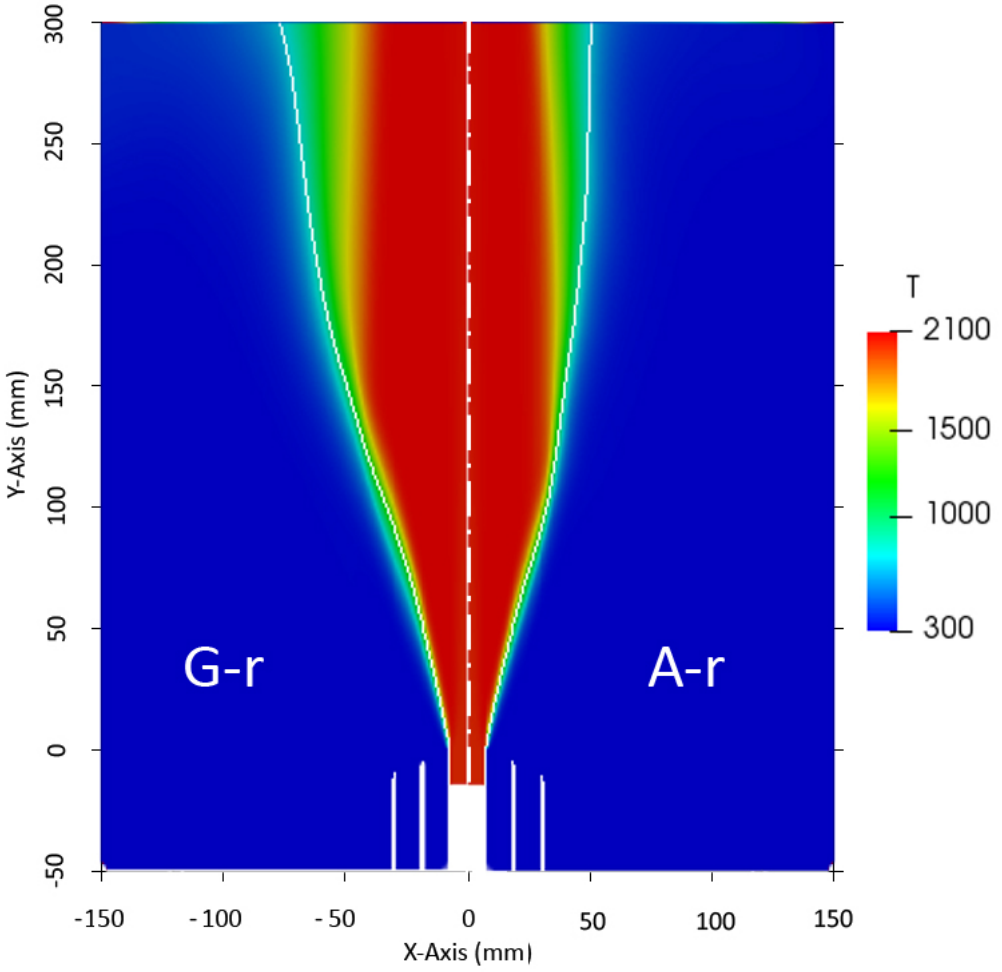

Figure 5.26: Mean temperature field $T(K)$ with iso-line of a regress variable b=0.5 (white). Left: case G-r, right: case A-r.

Figure 5.26 shows the mean temperature field with iso-line of a regress variable b = 0.5 that gives an indication about the flame front location for both cases G-r and A-r. In the upstream region y < 30 mm, it is noticed that the flame spreading angles of both cases is similar. Further downstream, the hot product gases expand radially faster for the G-r case than for the stratified case. This is because of the fact that the flames are burning toward the fresh reactant mixture coming from slot 2, and case G-r has a higher mixture fraction (equivalence ratio $\phi = 0.9$) in slot 2 compared to the stratified case ($\phi = 0.6$ in slot 2) which means higher burning rates, as shown in Figure 5.27. The effect of the mixture fraction

Z is present into the laminar flame speed parameter, which is a function of the mixture properties. Z values closer to stoichimetric ones in case G-r (slot 2) mean higher laminar flame speeds that is directly linked to the higher burning rates which make flame G-r spreads in a wider angle in downstream locations (y > 70 mm) compared to case A-r where burning toward the leaner mixture coming from slot 2 results in a reduced spreading angle.

Further downstream, the thinner flame brush in case A-r compared to G-r indicates a less fluctuation of the flame front, as captured also in Figure 2.3.

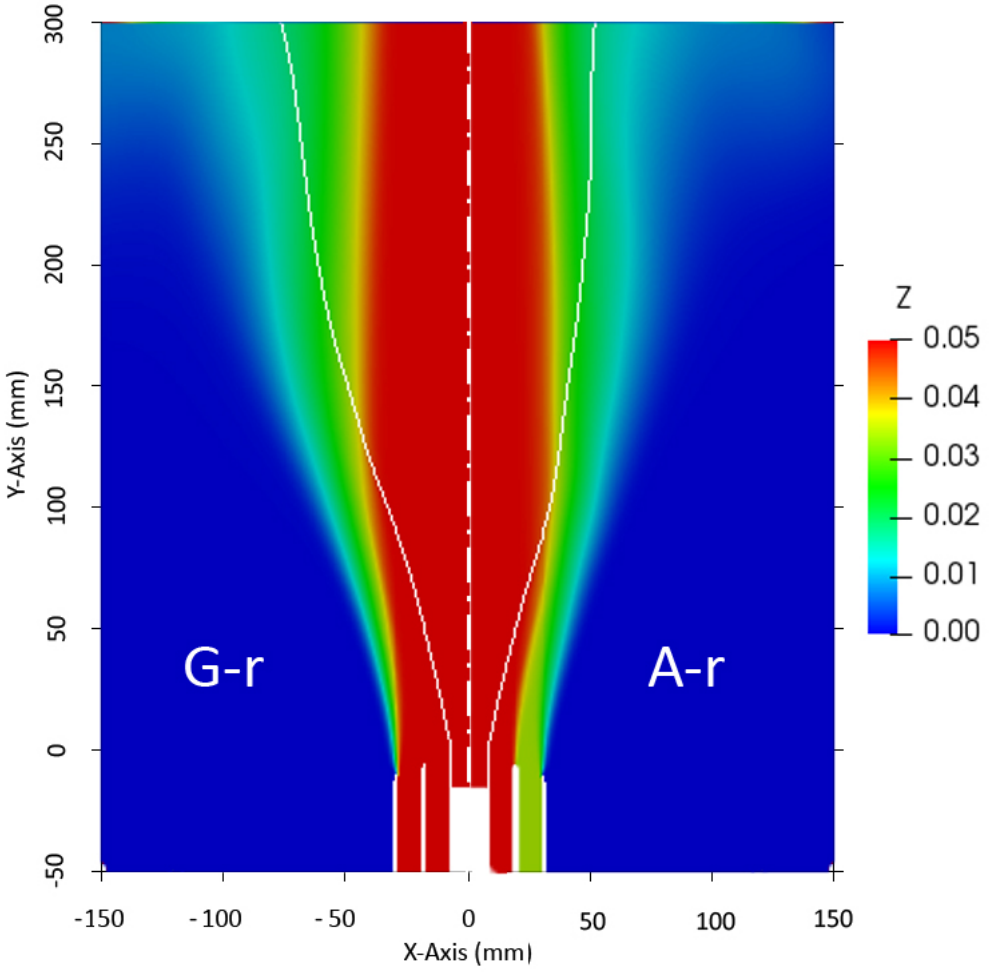

Figure 5.27: Mixture fraction field $Z(-)$ with iso-line of a regress variable b = 0.5 (white). Left: case G-r, right: case A-r.

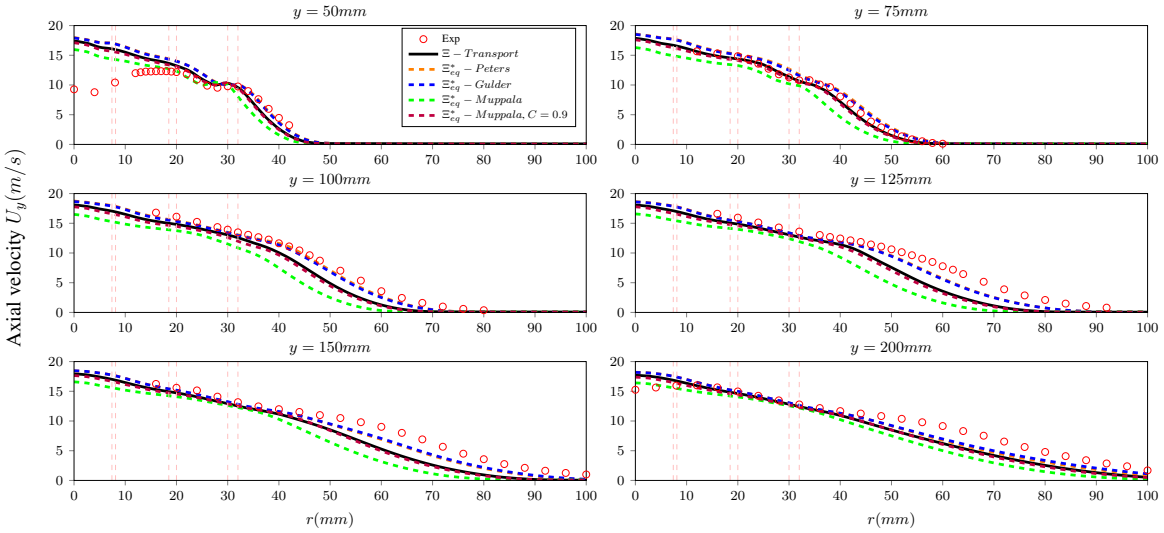

Figure 5.28: Mean axial velocity U_y for simulations with different flame wrinkling models at various axial locations y for the case G-r.

Figure 5.28 shows mean axial velocity profiles for the case G-r. A good agreement with experimental results is evident using Gulder and Peters correlations. The two-equations model ($\Xi - Transport$) also shows good results, however, it underpredicts the experimental results with the increase of radial direction for y >75 mm. Muppala-C=0.9 shows a very similar behavior of the two-equations model. However, Muppala-C=0.46 deviates significantly with the increase of radial velocity indicating that this model is not able to predict wide-spreading jet flows.

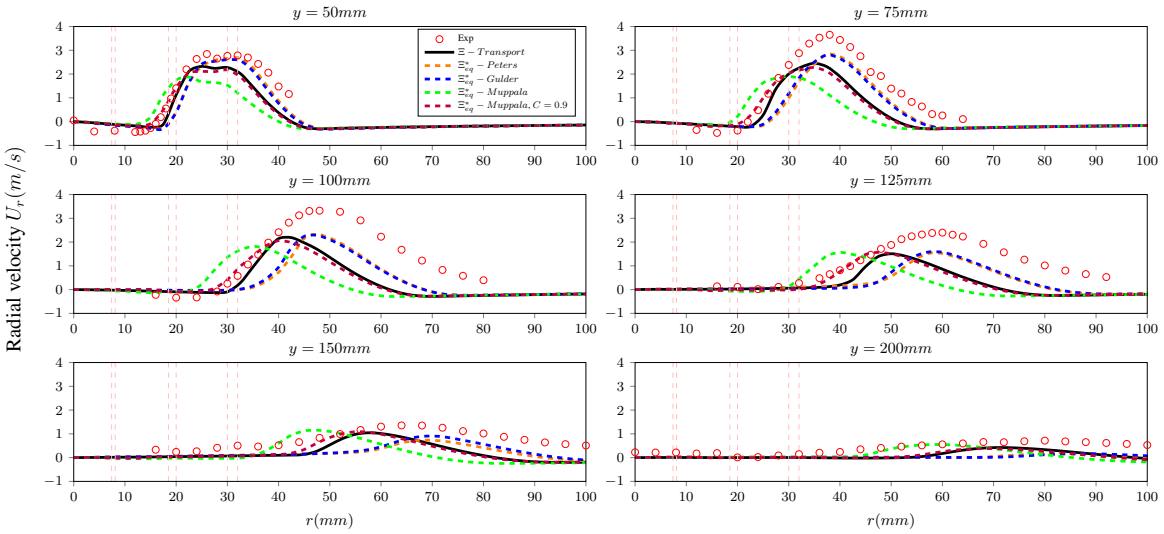

Figure 5.29: Mean radial velocity U_r for simulations with different flame wrinkling models at various axial locations y for the case G-r.

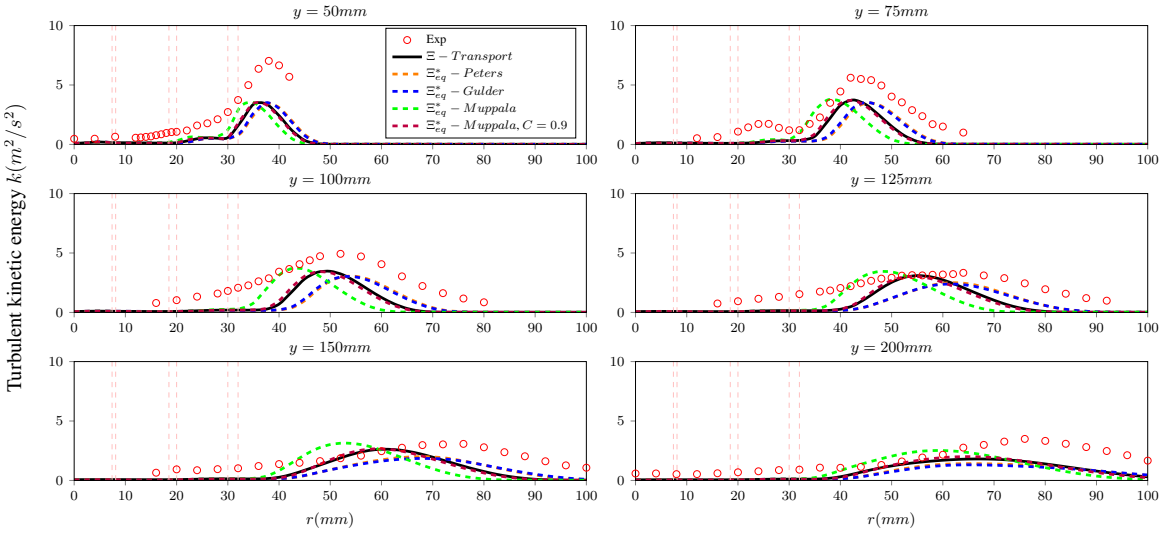

Figure 5.30: Turbulent kinetic energy k for simulations with different flame wrinkling models at various axial locations y for the case G-r.

For the radial velocity and the turbulent kinetic energy, shown in Figures 5.29 and 5.30 respectively, it has been demonstrated that Gulder and Peters correlations have similar behavior in premixed turbulent flames and they have a rather good prediction of all the peak locations which gives an indication about a correct prediction of the flame front. Also, $\Xi - Transport$ and Muppala-C=0.9 provide good results with a slight shift towards the radial direction while Muppala-C=0.46 has a more pronounced shift toward the centerline missing most of the peaks.

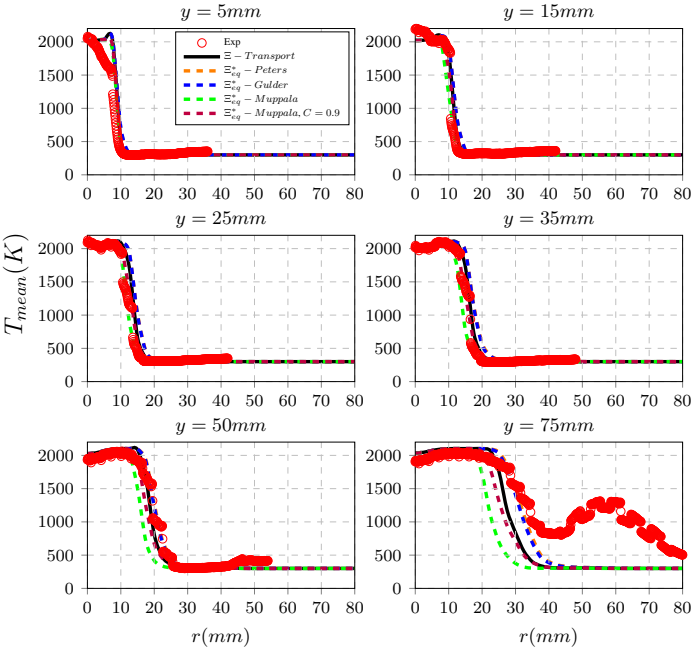

Figure 5.31: Mean temperature T for simulations with different flame wrinkling models at various axial locations y for the case G-r.

The mean temperature profiles are shown in Figure 5.31. The experimental results were measured only up to y = 75 mm. All models captured well the experimental measurements except at y = 75 mm. The sudden jump in the temperature profile at y = 75 mm and around y = 60 mm is not well understood. However, LES simulations show that the pockets of hot product gas are expelled from the flame core because of Kelvin-Helmholtz instability at the outer shear layer where a high-velocity shear is found and this might be responsible for the sudden jump in temperature measurement of flame G-r at y = 75 mm (see Figure 8 [54]). This behavior was not captured by RANS simulations using both the one-equation and the two-equations Weller model and can be a topic for further research.

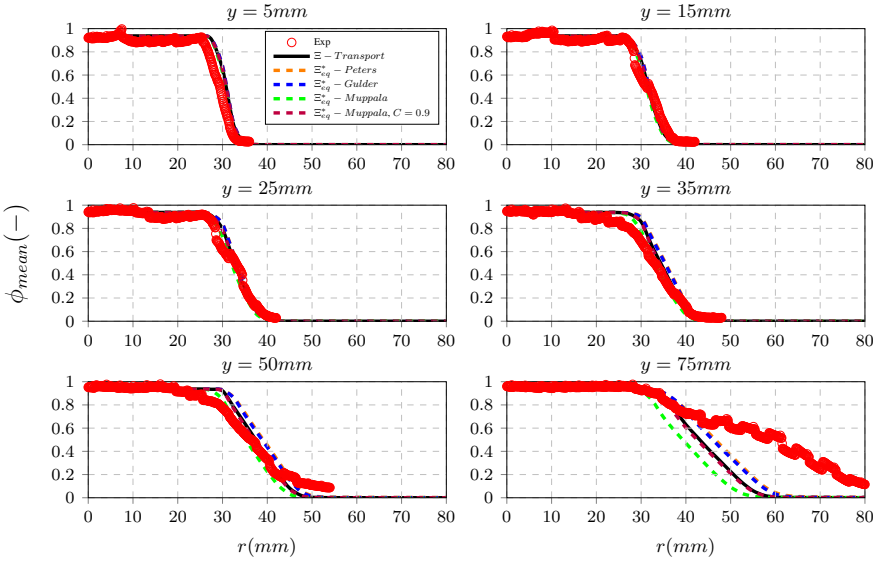

Figure 5.32: Mixture fraction Z for simulations with different flame wrinkling models at various axial locations y for the case G-r.

Figure 5.32 depicts the distribution of equivalence ratio for flame G-r. All models have a good prediction of the main trend. At y = 35 mm and y = 50 mm, the trend of the transition from the region of $\phi = 0.9$ of slot 2 into the co-flow region in the experimental measurements is more diffusive. However, all models show an abrupt transition. This might be related to the unity Lewis number assumption and the fact that differential diffusion effects are not considered in this study.

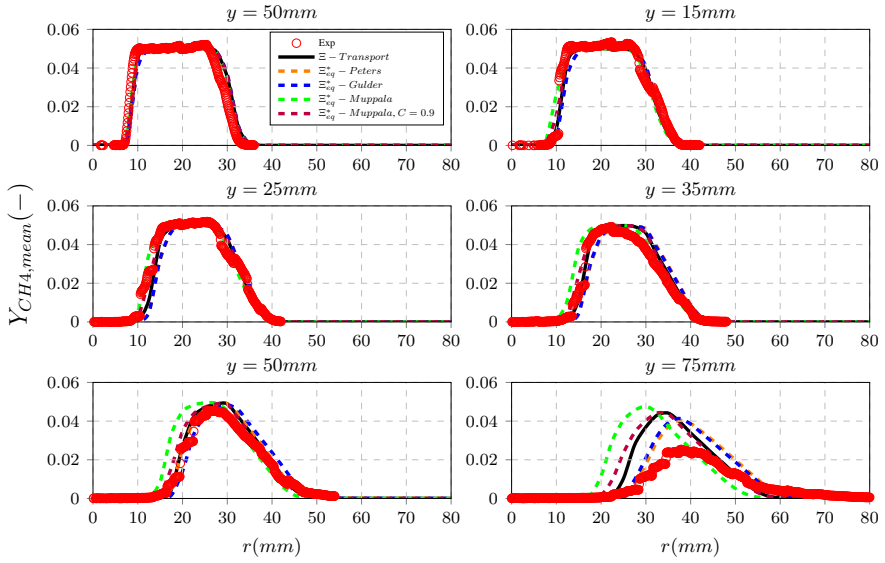

Figure 5.33: Mean mass fraction of CH_4 for simulations with different flame wrinkling models at various axial locations y for the case G-r.

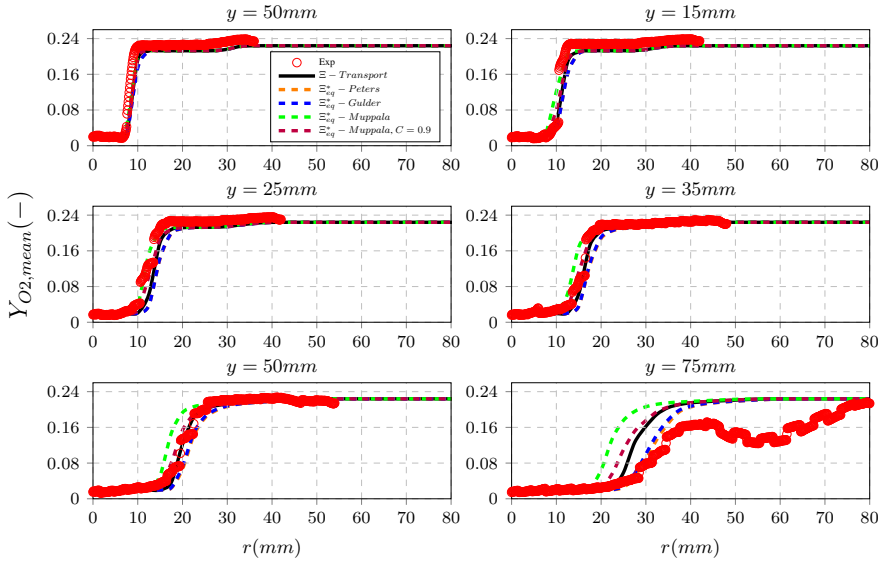

Figure 5.34: Mean mass fraction of O_2 for simulations with different flame wrinkling models at various axial locations y for the case G-r.

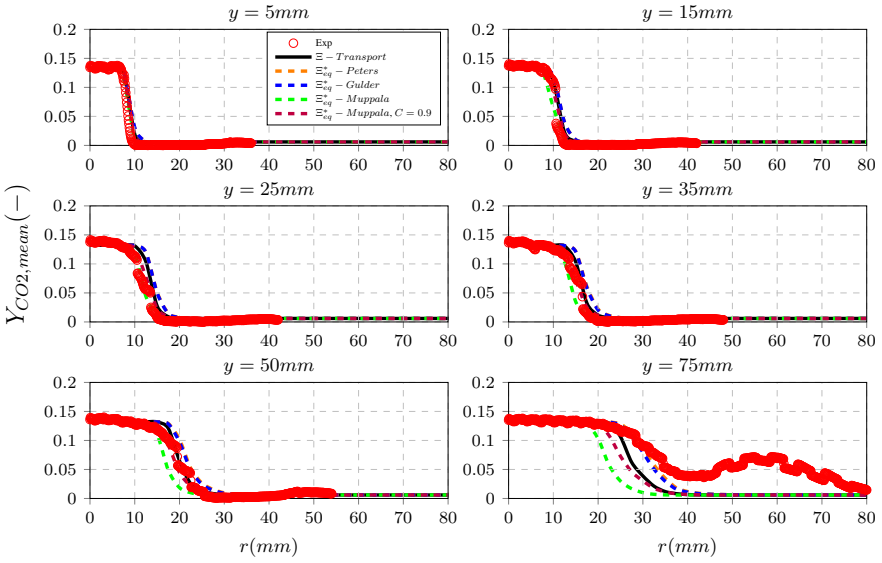

Figure 5.35: Mean mass fraction of CO_2 for simulations with different flame wrinkling models at various axial locations y for the case G-r.

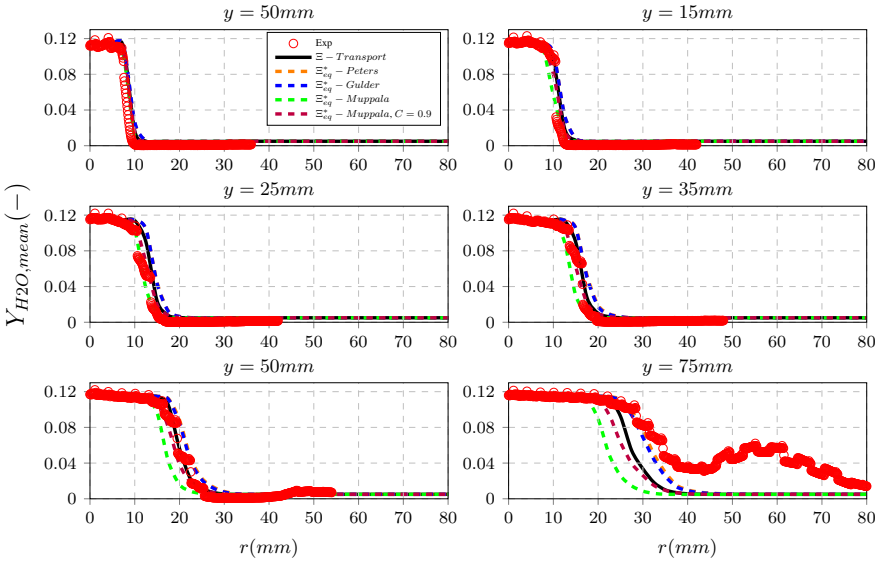

Figure 5.36: Mean mass fraction of H_2O for simulations with different flame wrinkling models at various axial locations y for the case G-r.

Figures 5.33, 5.34 ,5.35, and 5.36 show the mass fraction distribution of the main species. All models indicate good matching with experimental results except Muppala-C=0.46 where it shows only a partial agreement from the centerline up to y = 30 mm. Gulder and Peters correlations are found to be the most accurate to predict the trend at y = 75 mm up to a radial location of around r = 30 mm, followed by $\Xi - Transport$ and Muppala-C=0.9 which also gives good predictions at y = 75 mm but up to a radial location of around r = 25 mm only.

To some extent, a similar conclusion to the case A-r is drawn for the case G-r. Overall, the Weller model is able to predict the premixed flame G-r successfully using the one-equation and the two-equations versions of the model. All models show a satisfactory level of agreement with experiment except Muppala where it shows rather good agreement only in narrow regions from centerline up to r = 30 mm above the burner at various axial locations. Further in the radial direction, Muppala lack accuracy to predict the flow field correctly and the coefficient C is calibrated to 0.9 which shows significant improvements in the results. Similar behavior is observed between Gulder and Peters correlations which are found to be the most accurate among all the other models in predicting the flow field. $\Xi - Transport$ and Muppala-C=0.9 also show similar trends. Both provided consistent results but seem to underpredict the mean axial velocity faraway from the burner exit with the increase of radial direction. The general trend indicates that the one-equation model using Gulder and Peters show a more robust behavior than the two-equations model and Muppala-C=0.9 and can also provide sometimes better results especially in the faraway region with the increase of radial direction.

5.4 Flames regimes

Regime diagrams for premixed combustion in terms of velocity and length scale ratios have been proposed, for instance, by Borghi [14] and Peters [13] in order to distinguish between different regimes of turbulence-flame interactions. For scaling purposes, it is useful to assume equal diffusivities for all reactive scalars. Therefore, in this study, a Schmidt number ($Sc = \nu/D$) of unity is assumed and the flame thickness is defined as:

$$l_F = \frac{D}{S_u} \tag{5.2}$$

Where D is the mass diffusivity which is equal to the momentum diffusivity in this case based on the assumption of a Schmidt number of unity. S_u is the unstrained laminar flame speed.

The length ratio l/l_f is the ratio between the turbulent length scale to the flame thickness, while the velocity ratio is defined as the ratio between the turbulence intensity to the unstrained laminar flame speed u'/S_u. For more details of the theoretical background of the flame regime diagram proposed by Peters, which is used in this section, the reader is referred to [13].

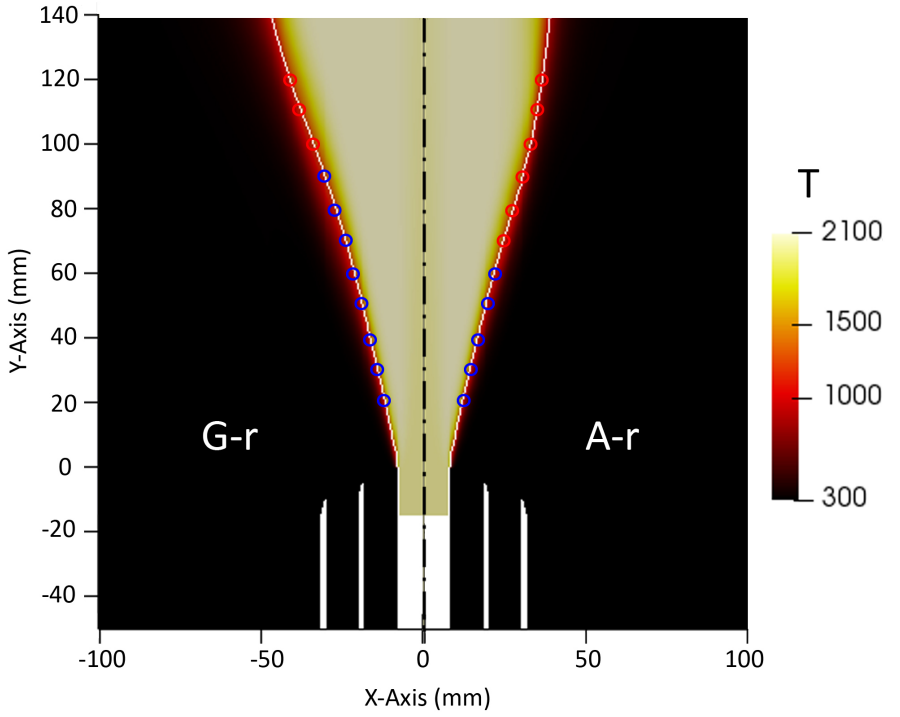

Figure 5.37: Flame temperature field $T(K)$ with iso-line of b = 0.5 (white) of the reactive cases G-r and A-r. The circles correspond to the locations where l/l_f and u'/S_u were evaluated. Blue circles correspond to the flamelets regime while red ones means that the flame is thickened-wrinkled.

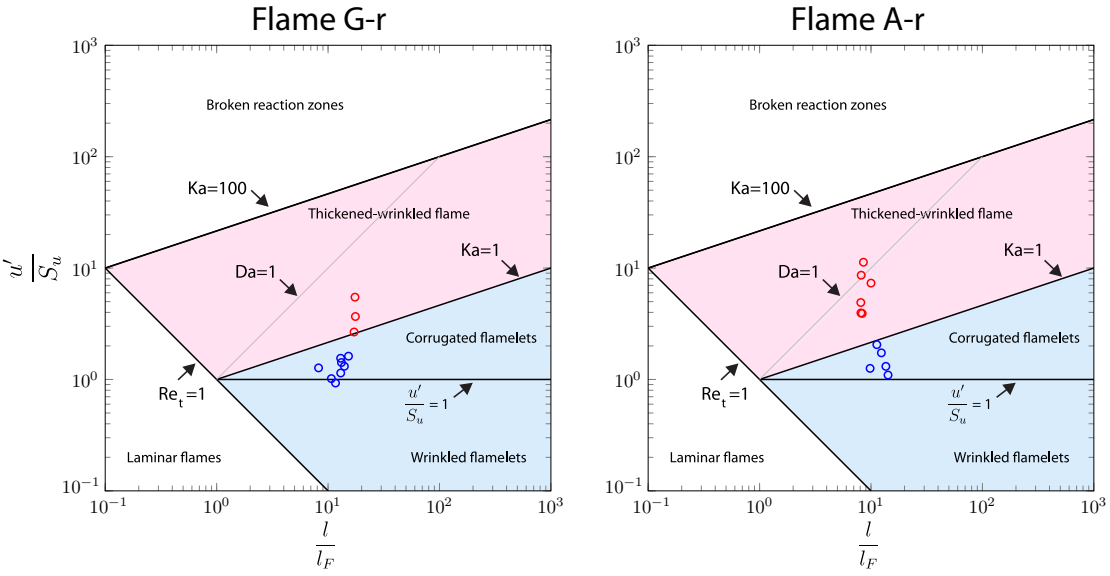

Figure 5.38: Regime diagram with the classification based on CFD calculations (circles) for the reactive cases G-r (left) and A-r (right). Light-blue shaded area is the flamelets regime while the pink shaded area corresponds to the thickened-wrinkled flame regime.

Eleven points were evaluated for the regime classification in each reactive flame case G-r and A-r, as shown in Figure 5.37. It shows also the axial locations

along the iso-line of a regress variable b = 0.5 where these CFD calculations of the ratios l/l_f and u'/S_u were evaluated from 20 mm < y < 120 mm. Blue circles correspond to the flamelets regime whereas the red ones correspond to the thickened-wrinkled flame regime. Figure 5.38 shows the Borghi-Peters regime diagram with the classifications based on the results of the numerical simulations (circles) for both flame G-r and A-r. The numerical results of case A-r is qualitatively similar to the one from the experimental data shown in Figure 2.5. However, different approaches for the estimations of the flame thickness led to the shift in the l/l_f ratio between numerical and experimental results.

For $u'/S_u < 1$, the flame front is solely wrinkled by turbulence (wrinkled flamelets). For $u'/S_u > 1$, the flame front is more strongly affected by turbulence and can exhibit folders entrapping burned or unburned gases (corrugated flamelets). Outside the flamelet regime, the thickened-wrinkled flame regime is characterized by Re > 1, 1 < Ka < 100, the last inequality indicating that the smallest eddies of size η can penetrate into the reactive-diffusive flame structure and increase the heat and mass transfer since $\eta < l_F$. However, the smallest eddies are still larger than the inner layer thickness ($l_\delta \sim l_F/10$) and thus cannot enter into that layer. The importance of unsteady effects was demonstrated by Poinsot et al. [55], who demonstrated that the smallest eddies cannot disturb the inner structure of a premixed flame, even though the flame thickness is of similar size, since the lifetime of the eddies is too short. Thus, for the existence of the flamelets, the condition of Ka < 1 of the Borghi diagram was found to be too restrictive and underestimates the flamelets regime by more than an order of magnitude of Ka values [55]. Lipatnikov et al. [56] also argued that increasing turbulence level favors the formation of even thinner highly strained reaction layers, so that the flamelets may extinguish before they broaden, and thickening by the penetration of small eddies is more likely to occur in the preheat zone, but not in the reaction layer.

The results presented in Figure 5.38 show that flame A-r is thickened-wrinkled at y = 70 mm compared to flame G-r which thickening of the flame starts from y = 100 mm. This is due to the fact that the unstrained laminar flame speed S_u is higher in slot 2 for flame G-r (higher equivalence ratio in slot 2) compared to flame A-r, as shown in Figure 5.39. Based on the arguments presented in this section from Poinsot DNS studies and Lipatnikov investigations, the flamelet assumption for both cases G-r and A-r is valid.

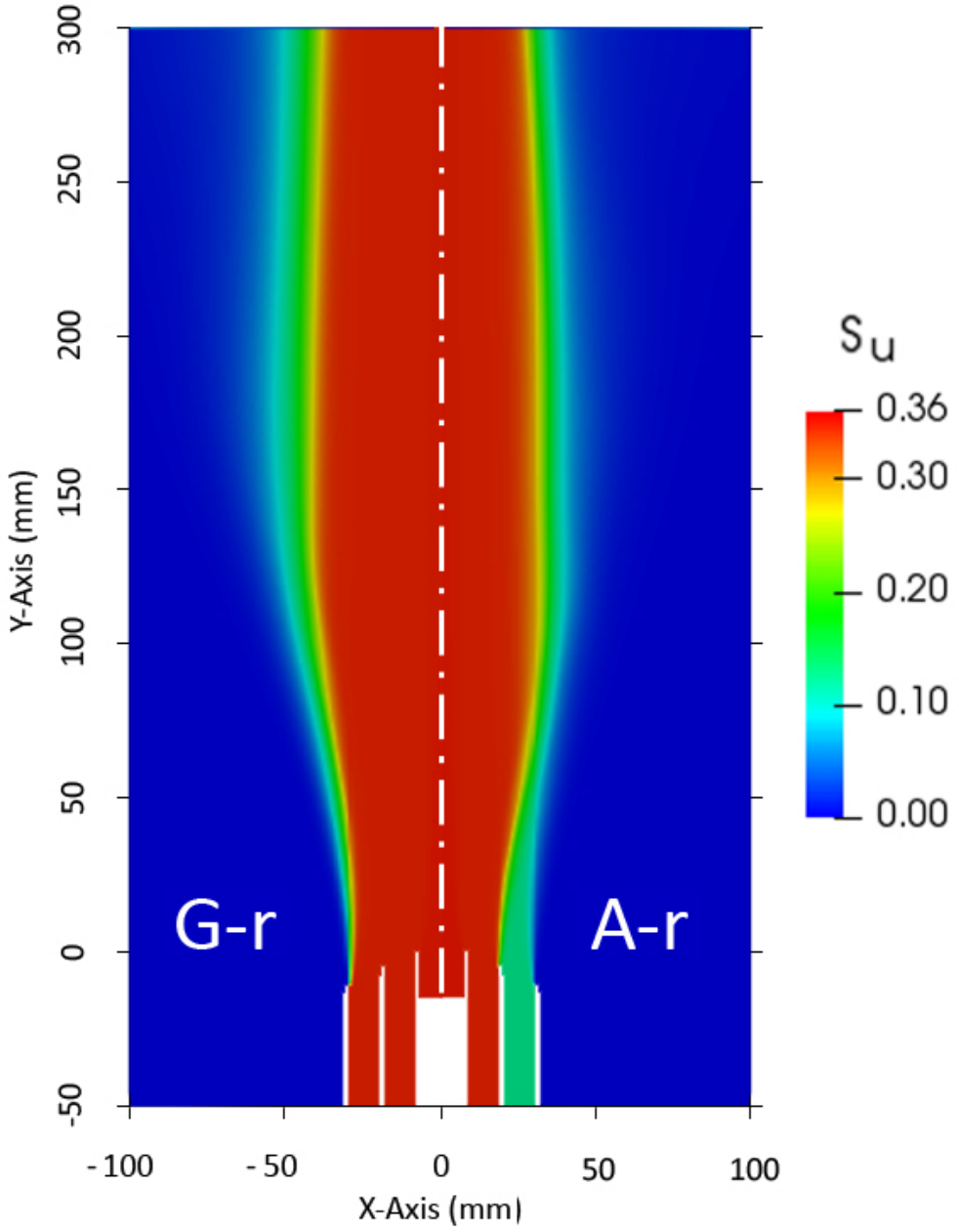

Figure 5.39: The unstrained laminar flame speed S_u (m/s) field in the reactive cases G-r (left) and A-r (right).

5.5 NO_x modelling

5.5.1 Kinetics of NO formation

The control of nitrogen oxides (NO_x) has been a major issue in designing modern combustion systems, since NO_x is identified as the dominant contributor to the formation of photochemical smog and acid rain, and also plays a key role in the ozone depletion. Thus, NO_x is a pollutant that arises the need to develop low emission combustion devices. The characteristics of NO_x emission can be quintessential information for the development of a clean combustor having suitable reduction approaches. The two essential sources of NO_x in the combustion of conventional fuels are oxidation of the molecular nitrogen (N_2) carried with the air and oxidation of nitrogen-containing compounds in the fuel (fuel-N). In most combustion devices NO_x emission consists of mostly nitric oxide (NO) that is formed from the oxidation of the molecular nitrogen. However, in combustion devices using coal or crude oil, which often contain significant amounts of organic nitrogen compounds, fuel-N can be an important source of NO. Suitable submodels to estimate NO_x emissions formed during the combustion process were incorporated in the LibLICE [47]. In this study, NO is chosen to represent NO_x and the Extended Zeldovich mechanism is used to model the formation of thermal NO [57], as follows:

$$\mathrm{O} + \mathrm{N_2} \longleftrightarrow \mathrm{NO} + \mathrm{N} \tag{5.3}$$

$$\mathrm{N} + \mathrm{O_2} \longleftrightarrow \mathrm{NO} + \mathrm{O} \tag{5.4}$$

$$\mathrm{N} + \mathrm{OH} \longleftrightarrow \mathrm{NO} + \mathrm{H} \tag{5.5}$$

In this study, the quasi steady state for N atoms is assumed which valid for most combustion cases, except in extremely fuel-rich combustion conditions. Reaction rate constants are taken from [57] after verifying that suggested values from recent works produce very consistent results that are validated against experimental measurements. A transport equation for NO mass fraction (Y_{NO}) is solved in the CFD domain with a source term computed in any cell accounting for the average temperature and species concentrations except NO for which the local concentration taken from Y_{NO} is used.

5.5.2 NO prediction in flame A-r and G-r

One of the main advantages of stratification in combustion systems is the reduction of NO_x emissions compared to the fully premixed combustion. Therefore, comparing profiles of NO pollutant at the exit of the burner for different stratified/fully-premixed cases is of great interest. Unfortunately, the TU Darmstadt experimentalist did not measure NO_x emissions. Hence, there is no experimental data of NO_x profiles for comparison. Furthermore, to the author's knowledge, there are no available numerical investigations of NO_x emissions for the TSF Darmstadt burner. This investigation is the first to be introduced into the literature for the TSF burner, and it is set to provide a qualitative and quantitative data for NO_x prediction so that it can be used for numerical and experimental comparisons purposes in the future.

In the studied burner, NO_x are expected to be essentially formed in high-temperature zones near pilot flame region, where Zeldovich mechanism prevails. The production rate of NO is highly sensitive to the predicted temperature. It has been shown by Kadar that the thermal NO production rate roughly doubles for every 100K temperature increase when the flame temperature is about 2000K [58]. Therefore, it is very important to state that the mass fraction of NO shown in Figures 5.40 and 5.41 is under the adiabatic assumption. Thus, it is expected that the numerical quantitative values overpredict the values from the experiment.

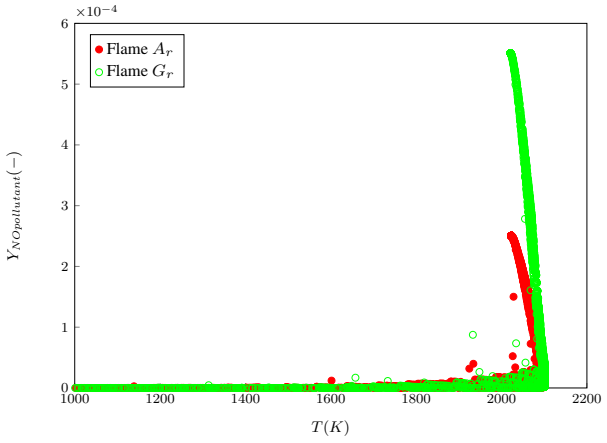

Figure 5.40: Scatter plot of mass fraction of NO vs temperature for the adiabatic simulations of flame A-r and G-r.

Figure 5.40 shows the mass fraction of NO plotted as a function of the temperature of the stratified case A-r and the fully premixed case G-r under the adiabatic assumption. Thus, the real NO formation from the experiment is expected to be lower because of the heat loss in the pilot tube. As stated by Kadar

[58], the production rate of NO is highly sensitive to the predicted temperature. These results serve as a first attempt to simulate NO in the TSF burner and can be used for comparison purposes in the future. As expected, NO mass fraction appears to be lower in the stratified case A-r compared to the case G-r. It is well known that the NO formation rate varies strongly with equivalence ratio. The NO formation decreases with the decrease of equivalence ratio which is the case in flame A-r. Other factors that affects NO formation are the concentration of global species O_2 and N_2 and the concentration of O atoms and OH radicals.

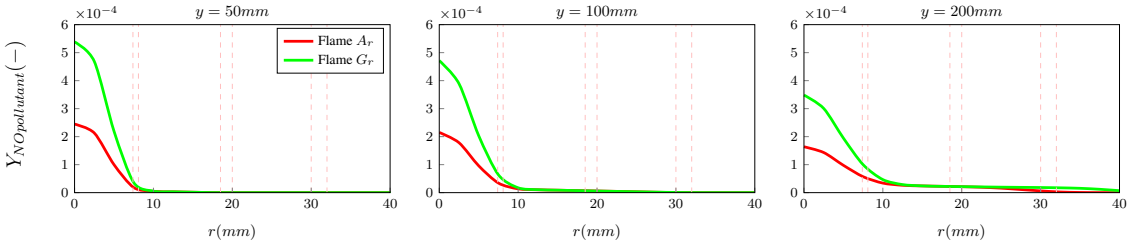

Figure 5.41: Mass fraction of NO at various axial locations y for in the adiabatic simulations of flame A-r and G-r.

Finally, the NO mass fraction profiles in the adiabatic simulations of flame A-r and G-r at various axial locations y are shown in Figure 5.40. The highest values for both cases are attained near the centerline above the pilot region which is expected since the temperature profile shows very high values in that region as depicted in Figure 5.19 for case A-r and Figure 5.31 for case G-r. Lower values are predicted for the stratified flame case A-r because of the effect of the lower equivalence ratio that plays a key factor in reducing the rate of formation of NO; Also, global species O_2 and N_2 distribution and the concentration of O atoms and OH radicals affect the rate of formation of NO.

5.6 Preliminary assessment of the CFM model

The Coherent Flamelet Model (CFM) is based on the flame surface density (FSD) concept. This model was first introduced by Marble and Broadwell (1977) and it was applied for diffusion flames [59]. More rigorous derivation was presented later by Candel et al. (1990) [60]. Then several improvements have been achieved through the years to make it suitable for premixed combustion too. It is also based on the flamelet assumption. In this study, an investigation of the proposed model by Choi-Huh of the CFM [29] is carried out for turbulent jet flames. The aim is to examine the ability of this model to simulate turbulent jet flames correctly including stratified flames. It is worth mentioning that this model has already been validated for engine simulations and gives rather good results. The solver `flameletCFMEngineDyMFoam` was modified during the course of this thesis to be suited for fixed volume combustion simulations. The new solver `flameletCFMFoam` is introduced which is based on the flamelet concept. A comprehensive description of the Choi-Huh version of the CFM model is presented in section 3.4.2.

The start of assessing this combustion model for turbulent stratified flames is through the cold flow simulations. The same initial fields shown in Figure 5.3 were used as the initial time step for the reactive case A-r in the folder `0` with the same boundary conditions shown in Table 5.2 and 5.3. The ignition characteristics and chemistry modelling are exactly the same to the one applied for the Weller model. The standard $k-\epsilon$ model was used for modeling turbulence. In the fist simulation, blowout occurred to the pilot flame. Thus the ignition characteristics were modified to sustain the propagation of the flame after several trials to the following:

```
ignitionSites
(
{
location (4e-4 -38e-3 0.0) ;
diameter 4e-3;
start 0.0;
duration 100e-3;
strength 4;
electricDelay 0;
}
);
```

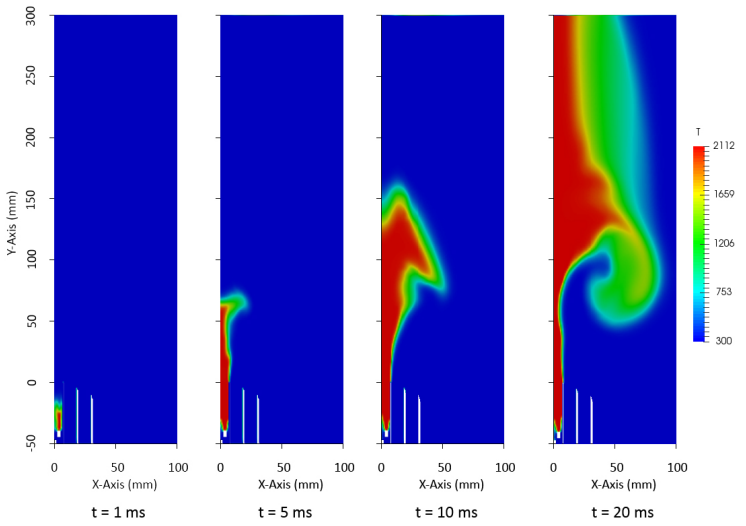

Figure 5.42: Snapshots of the evolution of the temperature field $T(K)$ of flame A-r at various time steps using the CFM model with Choi-Huh source terms.

Figure 5.42 shows the evolution of the temperature field using the Choi-Huh version of the CFM model. It is clear that the model is not able to predict the main temperature profile and significant instabilities of the flame surface density field Σ was observed. This led to complete misprediction of the flow filed suggesting that this model with the current implementation might not be suitable for jet flows simulation. The main issue might be related to the source terms of the Σ equation. The turbulent production source term for Σ is given by $S_{turb} = u'/l_{tc}$, where l_{tc} is a length scale introduced for dimensional reasons according to Choi-Huh [29]. That means the source term has a strong dependence on the turbulence intensity field and does not take into account other important parameters related to the flow field. The temperature evolution in Figure 5.42 is strongly related to the initial turbulent kinetic field k shown in Figure 5.3 (b). The flame has higher spreading rate depending on the high local turbulence intensity. This approach shows lack of describing the real complex phenomena that might involve other parameters as well. Due to limitations in the time frame of this thesis, a conclusion is made only on the performance of the Choi-Huh version of the CFM model for the stratified flame A-r and the premixed flame G-r simulations after several trials and a thorough parametric analysis that is not presented here for the sake of simplicity.

In conclusion, the use of the Choi-Huh version of the CFM model with the current implementation was not able to correctly simulate the Darmstadt TSF burner. The problem might be attributed to the source terms of the Σ equation, and particularly the production term of the flame surface density $S_{turb} = u'/l_{tc}$,

which depends mostly on the turbulence intensity u'. Although such a simplified description has been validated for engine applications, it was not able to capture the flow fields in this study and more understanding of this model version is needed in the future. Thus, there is a need for thoroughly validating such a model against a wide set of experimental data obtained from various well-defined simple flames under substantially different conditions.

Chapter 6

Conclusions

This thesis aimed to assess the Flame Area model proposed by Weller in the RANS context and to compare the performance of the one-equation version of this model, in which the wrinkling factor Ξ is modelled using an algebraic closure correlation, with the two-equations model version where a transport equation is instead solved for Ξ. A preliminary investigation of the Choi-Huh version of the Coherent Flamelet Model (CFM) was also considered. The Darmstadt TSF burner was selected with flame A-r (premixed stratified) and flame G-r (premixed homogeneous) as chosen cases for these assessments. The objective of this fundamental analysis is to identify the differences between these modelling strategies to support turbulent engine combustion simulations which involve more complex analysis.

The heat loss effect was not included in the chemistry table which will add a further dimension of the tabulation if included, thus it was omitted for simplicity at this stage since the main aim is to assess the general performance of the proposed combustion models. Also, differential diffusion effects were not considered.

To begin with, the one-equation and the two-equations Weller model versions were used to simulate the reactive stratified flame A-r and the fully premixed flame G-r. Three different correlations were considered for the algebraic closure of the flame wrinkling factor in the one-equation model version which are Peters, Gulder, and Muppala ones. These model versions were assessed based on the experimental data for the mean velocity statistics, temperature, mixture fraction, and species.

The following results are deduced from the Weller model simulations:

- A satisfactory agreement is found between the achieved numerical simulations results with both Weller model versions and the TSF burner experimental measurements; However, only a partial agreement is achieved when using Muppala correlation.

- Muppala correlation with the main calibration coefficient C=0.46 (proposed by Muppala) shows rather good agreement only in narrow regions from centerline to r = 30 mm at various axial locations. However, further in the radial direction, it seems to lack accuracy in predicting the flow field correctly implying that this correlation might not be highly accurate for wide-spreading jet flows. The reason might also be related to the unity Lewis number (Le) assumption because Muppala correlation is a function of this parameter.

- A parametric variation study on the main calibration coefficients of the different algebraic correlations in the one-equation combustion model indicates that the fine-tuning of these coefficients results in promising improvements, especially in the case of Muppala correlation where calibrating the main coefficient from C=0.46 to the new suggested value in this study, C=0.9, shows a significant improvement for both cases A-r and G-r.

- Although, the two-equation Weller model solves a transport equation for the flame wrinkling factor which might give a more detailed description of local parameters of the flow field, the one-equation model version (using Gulder and Peters correlations) shows a better agreement with the experimental measurements for flame G-r indicating the robustness of this model.

- Results also indicate that all considered models were sensitive to the turbulence intensity u' at the inlet boundary condition. Therefore, correct predictions of this quantity are important for obtaining accurate simulations.

- Finally, the first attempt to model NO_x of the TSF burner was performed in order to provide a qualitative and quantitative numerical data for NO_x prediction so that it can be used for numerical and experimental comparisons purposes in the future. The highest NO_x mass fractions for both cases A-r and G-r are attained near the centerline above the pilot region which is expected since the temperature profiles show very high values in this region. It was also evident that stratification could reduce NO_x pollutants. It is worth mentioning that these simulations were carried out under the adiabatic assumption. Since NO_x is highly sensitive to the temperature rise

when the flame temperature is about 2000K, the adiabatic NO_x simulations are expected to predict higher values compared to the experimental measurements because of the higher predicted temperature fields under the adiabatic assumption.

Regarding the CFM model, it was found that the Choi-Huh version of the CFM model was not able to capture the flow fields correctly in both cases A-r and G-r. The problem might be attributed to the source terms of the Σ equation, and particularly $S_{turb} = u'/l_{tc}$, which depends mostly on the turbulence intensity u' where l_{tc} is a length scale introduced for dimensional reasons. This might be due to the simplified description of the production source term of the flame surface density which does not take into account other flow field variables in case of turbulent jet flows. Nevertheless, more understanding of this model version is needed in the future.

Future works

The CFM model is widely used in applied CFD research to simulate turbulent premixed combustion in SI engines. However, to improve the prediction of novel combustion strategies, such as highly turbulent and stratified flames, there is a need for a further assessment of such model on controlled flame conditions. Moreover, little information is found in the literature on applying the CFM model for turbulent jet flows. This suggests that the application of this combustion model for combustors and burners is an area of future research.

Regarding the Weller model, it will be interesting to include the effects of heat losses and differential diffusion for a better prediction of the flow fields, especially for the NO_x profiles. Another area of interest to further assess the capabilities of this flame area model could be its application on more challenging cases, such as swirling flames. An example of this flame configuration type can be found in the Cambridge stratified swirl burner.

Bibliography

[1] International Energy Agency. "International Outlook for energy 2018: a view to 2040". pages 1–16, 2018. ISSN 03787788. doi: 10.1080/01998595.2012.10491656.

[2] P.A Pilavachi. Power generation with gas turbine systems and combined heat and power. *Applied Thermal Engineering*, 20(15):1421 – 1429, 2000. ISSN 1359-4311. doi: https://doi.org/10.1016/S1359-4311(00)00016-8. URL http://www.sciencedirect.com/science/article/pii/S1359431100000168.

[3] Elias Tsoutsanis, Nader Meskin, Mohieddine Benammar, and Khashayar Khorasani. A dynamic prognosis scheme for flexible operation of gas turbines. *Applied Energy*, 164:686 – 701, 2016. ISSN 0306-2619. doi: https://doi.org/10.1016/j.apenergy.2015.11.104. URL http://www.sciencedirect.com/science/article/pii/S0306261915015792.

[4] Mohammadreza Tahan, Elias Tsoutsanis, Masdi Muhammad, and Z.A. Abdul Karim. Performance-based health monitoring, diagnostics and prognostics for condition-based maintenance of gas turbines: A review. *Applied Energy*, 198:122 – 144, 2017. ISSN 0306-2619. doi: https://doi.org/10.1016/j.apenergy.2017.04.048. URL http://www.sciencedirect.com/science/article/pii/S0306261917304415.

[5] Saad Akhtar, Stefano Piffaretti, and Tariq Shamim. Numerical investigation of flame structure and blowout limit for lean premixed turbulent methane-air flames under high pressure conditions. *Applied Energy*, 228:21 – 32, 2018. ISSN 0306-2619. doi: https://doi.org/10.1016/j.apenergy.2018.06.055. URL http://www.sciencedirect.com/science/article/pii/S0306261918309267.

[6] M. Stöhr, I. Boxx, C. Carter, and W. Meier. Dynamics of lean blowout of a swirl-stabilized flame in a gas turbine model combustor. *Proceedings of the*

Combustion Institute, 33(2):2953 – 2960, 2011. ISSN 1540-7489. doi: https://doi.org/10.1016/j.proci.2010.06.103. URL http://www.sciencedirect.com/science/article/pii/S1540748910001781.

[7] Yannick Sommerer, David Galley, Thierry Poinsot, Sébastien Ducruix, François Lacas, and Denis Veynante. Large Eddy Simulation and Experimental Study of Flashback and Blow-Off in a Lean Partially Premixed Swirled Burner. *Journal of Turbulence*, 5:1–21, October 2004. doi: 10.1088/1468-5248/5/1/037. URL https://hal.archives-ouvertes.fr/hal-00183387.

[8] Erdzan Hodzic, Mehdi Jangi, Robert-Zoltan Szasz, and Xue-Song Bai. Large eddy simulation of bluff body flames close to blow-off using an eulerian stochastic field method. *Combustion and Flame*, 181:1 – 15, 2017. ISSN 0010-2180. doi: https://doi.org/10.1016/j.combustflame.2017.03.010. URL http://www.sciencedirect.com/science/article/pii/S0010218017301025.

[9] Davide E. Cavaliere, James Kariuki, and Epaminondas Mastorakos. A comparison of the blow-off behaviour of swirl-stabilized premixed, non-premixed and spray flames. *Flow, Turbulence and Combustion*, 91(2): 347–372, Sep 2013. ISSN 1573-1987. doi: 10.1007/s10494-013-9470-z. URL https://doi.org/10.1007/s10494-013-9470-z.

[10] Swetaprovo Chaudhuri and Baki M. Cetegen. Blowoff characteristics of bluff-body stabilized conical premixed flames with upstream spatial mixture gradients and velocity oscillations. *Combustion and Flame*, 153(4):616 – 633, 2008. ISSN 0010-2180. doi: https://doi.org/10.1016/j.combustflame.2007.12.008. URL http://www.sciencedirect.com/science/article/pii/S0010218008000254.

[11] Swetaprovo Chaudhuri, Stanislav Kostka, Michael W. Renfro, and Baki M. Cetegen. Blowoff dynamics of bluff body stabilized turbulent premixed flames. *Combustion and Flame*, 157(4):790 – 802, 2010. ISSN 0010-2180. doi: https://doi.org/10.1016/j.combustflame.2009.10.020. URL http://www.sciencedirect.com/science/article/pii/S0010218009003125.

[12] Suliman Abdelwahid, Medhat Nemitallah, Binash Imteyaz, Ahmed Abdelhafez, and Mohamed Habib. Effects of h2 enrichment and inlet velocity on stability limits and shape of ch4/h2–o2/co2 flames in a premixed swirl combustor. *Energy & Fuels*, 32(9):9916–9925, 2018. doi:

10.1021/acs.energyfuels.8b01958. URL https://doi.org/10.1021/acs.energyfuels.8b01958.

[13] Norbert Peters. *Turbulent Combustion*. Cambridge Monographs on Mechanics. Cambridge University Press, 2000. doi: 10.1017/CBO9780511612701.

[14] R. Borghi. *On the Structure and Morphology of Turbulent Premixed Flames*, pages 117–138. Springer US, Boston, MA, 1985. ISBN 978-1-4684-4298-4. doi: 10.1007/978-1-4684-4298-4_7. URL https://doi.org/10.1007/978-1-4684-4298-4_7.

[15] Giancarlo Ferrari. *Internal combustion engines*. 2014. ISBN 9788874888054.

[16] A.R. Masri. Partial premixing and stratification in turbulent flames. *Proceedings of the Combustion Institute*, 35(2):1115 – 1136, 2015. ISSN 1540-7489. doi: https://doi.org/10.1016/j.proci.2014.08.032. URL http://www.sciencedirect.com/science/article/pii/S1540748914004167.

[17] P.G. Aleiferis, Y. Hardalupas, A.M.K.P. Taylor, K. Ishii, and Y. Urata. Flame chemiluminescence studies of cyclic combustion variations and air-to-fuel ratio of the reacting mixture in a lean-burn stratified-charge spark-ignition engine. *Combustion and Flame*, 136(1):72 – 90, 2004. ISSN 0010-2180. doi: https://doi.org/10.1016/j.combustflame.2003.09.004. URL http://www.sciencedirect.com/science/article/pii/S0010218003002256.

[18] M.C. Drake and D.C. Haworth. Advanced gasoline engine development using optical diagnostics and numerical modeling. *Proceedings of the Combustion Institute*, 31(1):99 – 124, 2007. ISSN 1540-7489. doi: https://doi.org/10.1016/j.proci.2006.08.120. URL http://www.sciencedirect.com/science/article/pii/S154074890600383X.

[19] Yasuo Takagi. A new era in spark-ignition engines featuring high-pressure direct injection. *Symposium (International) on Combustion*, 27(2):2055 – 2068, 1998. ISSN 0082-0784. doi: https://doi.org/10.1016/S0082-0784(98)80052-0. URL http://www.sciencedirect.com/science/article/pii/S0082078498800520.

[20] Mingfa Yao, Zhaolei Zheng, and Haifeng Liu. Progress and recent trends in homogeneous charge compression ignition (hcci) engines. *Progress in Energy and Combustion Science*, 35(5):398 – 437, 2009. ISSN 0360-1285. doi:

https://doi.org/10.1016/j.pecs.2009.05.001. URL http://www.sciencedirect.com/science/article/pii/S0360128509000197.

[21] F Zhao, M.-C Lai, and D.L Harrington. Automotive spark-ignited direct-injection gasoline engines. *Progress in Energy and Combustion Science*, 25(5):437 – 562, 1999. ISSN 0360-1285. doi: https://doi.org/10.1016/S0360-1285(99)00004-0. URL http://www.sciencedirect.com/science/article/pii/S0360128599000040.

[22] Ehsan Fooladgar and C.K. Chan. Effects of stratification on flame structure and pollutants of a swirl stabilized premixed combustor. *Applied Thermal Engineering*, 124:45 – 61, 2017. ISSN 1359-4311. doi: https://doi.org/10.1016/j.applthermaleng.2017.05.197. URL http://www.sciencedirect.com/science/article/pii/S1359431116343022.

[23] K.T. Kim and S. Hochgreb. The nonlinear heat release response of stratified lean-premixed flames to acoustic velocity oscillations. *Combustion and Flame*, 158(12):2482 – 2499, 2011. ISSN 0010-2180. doi: https://doi.org/10.1016/j.combustflame.2011.05.016. URL http://www.sciencedirect.com/science/article/pii/S0010218011001623.

[24] K. T. Kim and S. Hochgreb. Effects of nonuniform reactant stoichiometry on thermoacoustic instability in a lean-premixed gas turbine combustor. *Combustion Science and Technology*, 184(5):608–628, 2012. doi: 10.1080/00102202.2011.652788. URL https://doi.org/10.1080/00102202.2011.652788.

[25] Taekyu Kang and Dimitrios C. Kyritsis. Methane flame propagation in compositionally stratified gases. *Combustion Science and Technology*, 177 (11):2191–2210, 2005. doi: 10.1080/00102200500240836. URL https://doi.org/10.1080/00102200500240836.

[26] Guido Kuenne, Florian Seffrin, Frederik Fuest, Thabo Stahler, Anja Ketelheun, Drik Geyer, Johannes Janicka, and Andreas Dreizler. Experimental and numerical analysis of a lean premixed stratified burner using 1d raman/rayleigh scattering and large eddy simulation. *Combustion and Flame*, 159(8):2669 – 2689, 2012. ISSN 0010-2180. doi: https://doi.org/10.1016/j.combustflame.2012.02.010. URL http://www.sciencedirect.com/science/article/pii/S0010218012000594. Special Issue on Turbulent Combustion.

[27] Mark S. Sweeney, Simone Hochgreb, Matthew J. Dunn, and Robert S. Barlow. The structure of turbulent stratified and premixed methane/air flames ii: Swirling flows. *Combustion and Flame*, 159(9):2912 – 2929, 2012. ISSN 0010-2180. doi: https://doi.org/10.1016/j.combustflame.2012.05.014. URL http://www.sciencedirect.com/science/article/pii/S0010218012001794.

[28] Weller Thermo-Fluids Section and H. G. Weller. The development of a new flame area combustion model using conditional averaging, 1993.

[29] Chang R. Choi and Kang Y. Huh. Development of a coherent flamelet model for a spark-ignited turbulent premixed flame in a closed vessel. *Combustion and Flame*, 114(3):336 – 348, 1998. ISSN 0010-2180. doi: https://doi.org/10.1016/S0010-2180(97)00194-6. URL http://www.sciencedirect.com/science/article/pii/S0010218097001946.

[30] Lorenzo Sforza, Tommaso Lucchini, Giovanni Gianetti, and Gianluca D'Errico. Development and validation of si combustion models for natural-gas heavy-duty engines. In *14th International Conference on Engines Vehicles*. SAE International, sep 2019. doi: https://doi.org/10.4271/2019-24-0096. URL https://doi.org/10.4271/2019-24-0096.

[31] F. Seffrin, F. Fuest, D. Geyer, and A. Dreizler. Flow field studies of a new series of turbulent premixed stratified flames. *Combustion and Flame*, 157 (2):384 – 396, 2010. ISSN 0010-2180. doi: https://doi.org/10.1016/j.combustflame.2009.09.001. URL http://www.sciencedirect.com/science/article/pii/S0010218009002491.

[32] T. Poinsot, D. Veynante, and S. Candel. Quenching processes and premixed turbulent combustion diagrams. *Journal of Fluid Mechanics Digital Archive*, 228:561, July 1991. doi: 10.1017/s0022112091002823. URL https://doi.org/10.1017/s0022112091002823.

[33] Molecular theory of gases and liquids. j. o. hirschfelder, c. f. curtiss, and r. b. bird. wiley, new york, 1954. xxvi + 1219 pp., $20.00. *Journal of Polymer Science*, 17(83):116–116, 1955. doi: 10.1002/pol.1955.120178311. URL https://onlinelibrary.wiley.com/doi/abs/10.1002/pol.1955.120178311.

[34] B.E. Launder and D.B. Spalding. The numerical computation of turbulent flows. *Computer Methods in Applied Mechanics and Engineering*, 3(2):269 –

289, 1974. ISSN 0045-7825. doi: https://doi.org/10.1016/0045-7825(74)90029-2. URL http://www.sciencedirect.com/science/article/pii/0045782574900292.

[35] F. R. Menter. Two-equation eddy-viscosity turbulence models for engineering applications. *AIAA Journal*, 32(8):1598–1605, 1994. doi: 10.2514/3.12149. URL https://doi.org/10.2514/3.12149.

[36] DAVID C. WILCOX. Reassessment of the scale-determining equation for advanced turbulence models. *AIAA Journal*, 26(11):1299–1310, 1988. doi: 10.2514/3.10041. URL https://doi.org/10.2514/3.10041.

[37] Henk Kaarle Versteeg and Weeratunge Malalasekera. *An introduction to computational fluid dynamics - the finite volume method.* Addison-Wesley-Longman, 1995. ISBN 978-0-582-21884-0.

[38] Brennen. *Internet book on fluid dynamics*. URL: http://brennen.caltech.edu/fluidbook/basicfluiddynamics/turbulence/ lawofthewall.pdf, 2016.

[39] J. Guerrero. *A crash introduction to turbulence modelling in openfoam*. URL: http://www.arek.pajak.info.pl/wp-content/uploads/2015/03/15turbulenceOF.pdf, lecture notes, university of genoa. edition, 2014.

[40] T. Poinsot and D. Veynante. *Theoretical and Numerical Combustion*. Edwards, 2001. ISBN 9781930217058. URL https://books.google.it/books?id=HMvCQgAACAAJ.

[41] Xiaofeng Yang, Arun Solomon, and Tang-Wei Kuo. Ignition and combustion simulations of spray-guided sidi engine using arrhenius combustion with spark-energy deposition model. In *SAE 2012 World Congress Exhibition*. SAE International, apr 2012. doi: https://doi.org/10.4271/2012-01-0147. URL https://doi.org/10.4271/2012-01-0147.

[42] R. Herweg and R. R. Maly. A fundamental model for flame kernel formation in s. i. engines. In *International Fuels Lubricants Meeting Exposition*. SAE International, oct 1992. doi: https://doi.org/10.4271/922243. URL https://doi.org/10.4271/922243.

[43] Changyou Chen and Ali Veshagh. A refinement of flame propagation combustion model for spark-ignition engines. In *International Congress*

Exposition. SAE International, feb 1992. doi: https://doi.org/10.4271/920679. URL https://doi.org/10.4271/920679.

[44] *A Comparison of Turbulent Flame Speed Correlations for Hydrocarbon Fuels at Elevated Pressures*, volume Volume 4B: Combustion, Fuels and Emissions of *Turbo Expo: Power for Land, Sea, and Air*, 06 2016. doi: 10.1115/GT2016-57804. URL https://doi.org/10.1115/GT2016-57804. V04BT04A043.

[45] Ömer L. Gülder. Turbulent premixed flame propagation models for different combustion regimes. *Symposium (International) on Combustion*, 23(1):743 – 750, 1991. ISSN 0082-0784. doi: https://doi.org/10.1016/S0082-0784(06)80325-5. URL http://www.sciencedirect.com/science/article/pii/S0082078406803255. Twenty-Third Symposium (International) on Combustion.

[46] Ömer L. Gülder. Correlations of laminar combustion data for alternative s.i. engine fuels. In *West Coast International Meeting and Exposition*. SAE International, aug 1984. doi: https://doi.org/10.4271/841000. URL https://doi.org/10.4271/841000.

[47] Tommaso Lucchini, Gianluca D'Errico, Angelo Onorati, Alessio Frassoldati, Alessandro Stagni, and Gilles Hardy. Modeling non-premixed combustion using tabulated kinetics and different fame structure assumptions, mar 2017. ISSN 1946-3936. URL https://doi.org/10.4271/2017-01-0556.

[48] F. Cavallo Marincola, T. Ma, and A.M. Kempf. Large eddy simulations of the darmstadt turbulent stratified flame series. *Proceedings of the Combustion Institute*, 34(1):1307 – 1315, 2013. ISSN 1540-7489. doi: https://doi.org/10.1016/j.proci.2012.08.001. URL http://www.sciencedirect.com/science/article/pii/S1540748912003720.

[49] Muppala, Siva and Madhav Rao, Vendra C. Numerical implementation and validation of turbulent premixed combustion model for lean mixtures. *MATEC Web Conf.*, 209:00004, 2018. doi: 10.1051/matecconf/201820900004. URL https://doi.org/10.1051/matecconf/201820900004.

[50] Renaud Mercier. Turbulent combustion modeling for large eddy simulation of non-adiabatic stratified flames. 2015.

[51] A numerical study of the laminar flame speed of stratified methane/air flames. *Proceedings of the Combustion Institute*, 28(2):1925 – 1932, 2000. ISSN 1540-7489. doi: https://doi.org/10.1016/S0082-0784(00)80597-4. URL http://www.sciencedirect.com/science/article/pii/S0082078400805974.

[52] Dynamic response of strained premixed flames to equivalence ratio gradients. *Proceedings of the Combustion Institute*, 28(2):1859 – 1866, 2000. ISSN 1540-7489. doi: https://doi.org/10.1016/S0082-0784(00)80589-5. URL http://www.sciencedirect.com/science/article/pii/S0082078400805895.

[53] Lorenzo Sforza. *Development of a comprehensive CFD model for spark-ignition engine combustion*. PhD thesis, Politecnico di Milano, 2018. URL https://www.politesi.polimi.it/handle/10589/143396.

[54] By A. Roux and Heinz Pitsch. Large-eddy simulation of stratified combustion. 2011.

[55] Thierry Poinsot, Sébastien Candel, and Arnaud Trouvé. Applications of direct numerical simulation to premixed turbulent combustion. *Progress in Energy and Combustion Science*, 21(6):531 – 576, 1995. ISSN 0360-1285. doi: https://doi.org/10.1016/0360-1285(95)00011-9. URL http://www.sciencedirect.com/science/article/pii/0360128595000119.

[56] A.N. Lipatnikov and J. Chomiak. Turbulent flame speed and thickness: phenomenology, evaluation, and application in multi-dimensional simulations. *Progress in Energy and Combustion Science*, 28(1):1 – 74, 2002. ISSN 0360-1285. doi: https://doi.org/10.1016/S0360-1285(01)00007-7. URL http://www.sciencedirect.com/science/article/pii/S0360128501000077.

[57] Craig T. Bowman. Kinetics of pollutant formation and destruction in combustion. *Progress in Energy and Combustion Science*, 1(1):33 – 45, 1975. ISSN 0360-1285. doi: https://doi.org/10.1016/0360-1285(75)90005-2. URL http://www.sciencedirect.com/science/article/pii/0360128575900052.

[58] A.H. Kadar. Modelling turbulent non-premixed combustion in industrial furnaces. *repository.tudelft.nl*, 2015.

[59] Frank E. Marble and James E. Broadwell. The coherent flame model for turbulent chemical reactions. 1977.

[60] SEBASTIEN M. CANDEL and THIERRY J. POINSOT. Flame stretch and the balance equation for the flame area. *Combustion Science and Technology*, 70(1-3):1–15, 1990. doi: 10.1080/00102209008951608. URL https://doi.org/10.1080/00102209008951608.